MATERIALS FOR ENERGY STORAGE IN LITHIUM-ION BATTERIES

by

Jiajia Tan

A dissertation submitted to the faculty of
The University of Utah
in partial fulfillment of the requirements for the degree of

Doctor of Philosophy

Department of Materials Science and Engineering

The University of Utah

December 2012

The University of Utah Graduate School

STATEMENT OF DISSERTATION APPROVAL

The dissertation of **Jiajia Tan**

has been approved by the following supervisory committee members:

Ashutosh Tiwari	, Chair	**7/16/2012** Date Approved
Ling Zang	, Member	**6/26/2012** Date Approved
Agnes Ostafin	, Member	**6/26/2012** Date Approved
Reaz Chaudhuri	, Member	**7/10/2012** Date Approved
Michael Free	, Member	Date Approved

and by **Dinesh Shetty** , Chair of

the Department of **Materials Science and Engineering**

and by Charles A. Wight, Dean of The Graduate School.

ABSTRACT

Electric vehicles using on-board electricity as a power source have been commercialized for application in a small part of the automobiles market. For wide substitution of the current gasoline-powered vehicles, a lot of effort should be placed on improving the performance of lithium-ion batteries (LIBs), which are the dominant power sources of recent groups of electric vehicles. In this work, we studied several promising cathode and solid-state electrolyte materials for realization of high-capacity, high-safety LIBs.

Poly-anionic $LiFePO_4$ and $Li_2FeP_2O_7$ have been considered very promising cathode materials for LIBs. They have large specific capacities, high thermal and chemical stability, and low cost. However, both of them have the same problem of low ionic and electronic conductivities. In order to speed up the kinetics in the LIBs, these poly-anionic materials were synthesized by developing a simple and high-throughput solution-based technique. The sort of chelating agent and the amount of carbon atoms in the starting solution were varied and the optimal parameters were found for $LiFePO_4$ and $Li_2FeP_2O_7$, respectively.

The safety issue is another important factor for electric vehicles; it is not ensured by current LIBs using organic liquid electrolytes, which are flammable and volatile, prone to leak and decompose at high temperatures. Therefore, recent research has been focused on developing solid-state electrolytes. In this work, high-quality garnet-type

$Li_7La_3Zr_2O_{12}$ (LLZO) electrolytes were synthesized using a solution-based technique. The ionic conductivity of cubic LLZO was revealed to be 1.67×10^{-4} S/cm. A proto-type cell comprised of LLZO electrolyte, $LiCoO_2$ cathode and lithium metal anode was assembled. The cell possessed a gravimetric discharge capacity of 3.4 mAh/g. This value is quite low compared to conventional cells, mainly due to its large interfacial resistance.

For improving the interfacial contact, LLZO was fabricated into thin films by pulsed laser deposition technique. The films deposited at room temperature had amorphous structure, and exhibited a lithium-ion conductivity of 3.35×10^{-7} S/cm. The effects of annealing on the properties of the films were investigated. Films annealed properly were found to have an enhanced lithium-ion conductivity value of 7.36×10^{-7} S/cm. Moreover, the as-deposited thin films were found to be electrochemically stable against lithium metal.

To my husband Haixiao

TABLE OF CONTENTS

LIST OF FIGURES

LIST OF TABLES

LIST OF ABBREVIATIONS

DC	Direct current
EDS	Energy dispersive x-ray spectroscopy
FTIR	Fourier transform infrared spectroscopy
LIBs	Lithium-ion batteries
LLZO	$Li_7La_3Zr_2O_{12}$
PLD	Pulsed laser deposition
PVD	Physical vapor deposition
SEM	Scanning electron microscope
UV	Ultraviolet
XRD	X-ray diffraction

ACKNOWLEDGEMENTS

I would like to thank my advisor, Professor Ashutosh Tiwari, for guidance, support and the special opportunity to work with him in the Nanostructured Materials Research Laboratory. I would also like to thank my committee for their input and assistance.

I would like to especially thank my husband for supporting my study and life during the time of degree pursuing.

CHAPTER 1

INTRODUCTION

Lithium-ion batteries have changed our lifestyles tremendously. In the 1980s LIBs began finding applications as power sources in watches, calculators and implantable medical devices. In today's age of information and speed, LIBs have become integral components in portable computing, entertainment, telecommunication equipment, and even automobiles. Since conventional automobiles are one of the major contributors of greenhouse gases, there is significant effort to reduce or replace fossil fuel demand by developing hybrid and electric vehicles. LIBs will provide a breakthrough in electric vehicle acceptance and widespread use. In this section, we will give a brief introduction of the basic parts and working principles of LIBs, and their advantages and challenges.

A primary battery is an energy transformation device that converts the chemical energy stored in its active materials into electric energy through electron and lithium ion transfer caused by an oxidation-reduction reaction. For Li-ion battery systems, the reaction is reversible when supplied with external electric power source. Normally, a battery is composed of one or more cells (basic electrochemical unit) that are electrically

---

Reprinted with kind permission of Springer Science and Business Media. Reprint with changes by adding other materials and cutting off some original content.
Tan, J.; Tiwari, A. Lithium-based batteries for efficient energy storage: Nanotechnology and its implications. In Energy Efficiency and Renewable Energy Through Nanotechnology; Zang, L. Ed. 2011; pages: 719-724, 730-731, 748-754; Figures: 1, 2, 10, 11, 20.

connected in series or parallel to provide the required operating voltage and capacity. In our discussion, we generally refer to lithium ion battery as a single cell.

Each cell consists of positive and negative electrodes, an electrolyte and a separator. The positive electrode has a higher chemical potential than the negative electrode. The operating process is demonstrated in Figure 1.1. The positive electrode provides lithium ions and becomes oxidized as an anode when charged. When discharging, lithium ions are inserted back into the positive electrode, which is reduced as a cathode. In contrast, the negative electrode is the opposite electrode during cycling. Since the lithium ions can be inserted and removed from the electrodes, they are also called insertion electrode materials. In general, the positive electrode is referred to as the cathode and the negative electrode as the anode, which is correct only when the cell is discharged. The ionic conducting electrolyte provides the medium for transfer of ions between the anode and cathode. The electrolyte is typically a liquid composed of solvents, aqueous or nonaqueous and dissolved lithium salts, acids, or alkali to enable ionic conductivity. Some batteries use solid electrolytes, which require high operating temperatures (> 80 ^{o}C) in order to realize acceptable ionic conductivity of electrolyte. The anode and cathode electrodes should be electronically separated to prevent internal short-circuiting. Thus the electrolyte should not be electronically conductive, and a mesoporous polymer separator is designed to isolate electrodes while allowing ions to move through it.

The main parameters that determine the electrochemical performances of a LIB are cell potential (V), specific energy capacity, rate capability and cycling ability. Energy capacity describes the ability of hosting lithium ions, with units of Wh/kg or Wh/L,

representing the energy stored per mass or volume. High energy capacity is critical for the application of light small power sources in portable electronic devices and hybrid vehicles. The specific rate, with units of A/kg or A/L, is crucial when large current is required, as in hybrid vehicles and large power devices. The rate capability is mainly determined by the both the electric conductivity within the electrode and the ionic conductivity within the electrodes, electrolyte, and across the electrolyte-solid-interface (SEI). The operating current is often expressed as 1C, 2C or 0.1C, where C stands for the current (A/Kg) that will charge an electrode to its theoretical capacity in 1 hour. If an operating current is xC, then the theoretical specific capacity is obtained in 1/x hour. Rate capability is considered good only if the experimentally obtained capacity is close to theoretical capacity, no matter what operating current is applied. The cycling ability reflects the stability of the cell after several hundred times of charging/discharging and is determined by factors such as volume expansion/contraction, structure-maintaining ability and thermal stability.

Li-based batteries have outperformed other battery systems and account for much more than half of worldwide sales in portable batteries due to several advantageous properties against which no other battery system can compete. First, LIBs have high operating voltages and high energy densities. A single cell has an average operating potential of approximately 3.6-4 V, much higher than that of Ni-Cd, Ni-MH and Pb-acid batteries. Lithium is less dense and the most electropositive metal in the periodic table; hence, high energy density is predicted. The specific capacity is more than 1.5 times that of Ni-Cd batteries. Figure 1.2 shows the power density and energy density of various battery systems [1]. In this picture, 4G/5G refers to devices that provide users with IP

telephony, ultrabroadband Internet access, gaming services and streamed multimedia. EV and HEV are abbreviations for electric vehicles and hybrid electric vehicles. It can be seen that the Li-ion batteries have the highest power and energy densities, and come the closest to meeting projected requirements for further application, though there are still improvements to be made.

The second advantage of lithium-ion batteries is the impressively high charging and discharging rate. Up to 3C of the discharging rate and 1C of charging rate are attainable. The operating temperature range is large, from -20 to +60 ˚C. In addition to the advantages described above, LIBs have a superior cycle life, exceeding 1000 cycles; low self-discharge (8-12% per month), and long shelf lives. There is also no memory-effect and thus, they can be recharged at any time.

With these advantages in mind, there are still some problems that limit the usage of LIBs. Some problems proposed several decades ago still need solutions, such as safety issues and restricted assembly conditions. Moreover, energy capacity and cycling life requirements will continue to increase, as shown in Figure 1.2.

One problem associated with metallic Li is the formation of dendrites, leading to short-circuiting, then thermal runaway and possible explosion. Moreover, metallic lithium is highly reactive with oxygen, nitrogen and moisture; thus, glove boxes or dry-rooms become necessary for assembly. Battery assembly is much simpler if insertion electrodes composed of Li compounds are used as both anode and cathode, since they are stable in the ambient atmosphere. Therefore, several insertion anode materials have been explored, including graphite, titanium oxide, silicon, carbon nanofibers, etc. Research on anode materials is very popular today, since new anode materials have much higher

specific capacity than the commonly used graphite. Their developmental status and properties will be discussed in detail in the anode section.

Another big problem with lithium-ion batteries is that any Li that has participated in a secondary reaction cannot be reversibly removed; this property is described as small Coulombic efficiency and poor reversibility. The capacity will also fade due to processes such as electrolyte decomposition, phase changes in the insertion/desertion of lithium ions, and passive film formation on the electrodes. The passive films are called solid electrolyte interface (SEI), and are formed by decomposition of electrolyte and deposition of lithium salts. On one hand, the SEI helps protect against further corrosion of lithium. On the other, if the SEI becomes very thick due to unnecessary side reactions between electrolyte and electrodes, it can cause a significant loss in capacity and will become highly resistive to ionic conduction. This is also a critical factor when choosing suitable electrode materials and electrolyte for LIBs.

A lot of efforts have been made to improve the performance of the LIBs by developing novel cathode materials. For example, substitution of Mn in $LiMn_2O_4$ with Ni and Cr is known to increase the operating voltage (up to 5 V) and reduce capacity fading. The main problem with many cathode materials is low ionic conductivity, which significantly limits the rate capability and reversibility. Nanotechnologies can help mitigate this problem by reducing the particle size in a variety of ways. Nanosized or nanostructured materials exhibit faster rate and higher specific capacity since the Li^+ diffusion length is shortened, the reaction sites are modified and the electrolyte-electrode contact area is increased. However, too large a contact area between electrode and electrolyte is not preferable, since a significant amount of side reactions will take

place, resulting in low Coulombic efficiency. More advanced mesoporous materials with ordered or disordered micro pores can be developed, which have many advantages and disadvantages of their own. These will be discussed in the cathode section.

Electrolytes have also attracted attention because they will lower the risk of danger when using a low vapor pressure or even solid electrolyte. Novel electrolytes are essential when making thin-film batteries and lithium-oxygen batteries. These issues are covered in the last two sections of this chapter.

1.1 Previous Research on $LiFePO_4$ Polyanionic Cathode

1.1.1 Criteria for Good Cathodes

Li metal was first utilized in the 1970s to assemble primary Li cells. This kind of cell found applications in implantable medical devices, after hydrogen gas production was avoided in the cell [2]. Simultaneously, researchers revealed the intercalation ability of alkali metal ions into dichalcogenides. From then on, lithium-ion batteries have become one of the most highlighted research areas. Over last 40 years, various kinds of cathode materials have been investigated in order to achieve the synthesis of high capacity, high electrochemical potential, fast rate, low cycling fading, low cost and environment friendly material. An ideal cathode material should satisfy all these criteria:

1) The cathode should have a high redox potential;

2) The potential should not change much, normally within 0.4 V, for different degrees of lithium insertion/extraction;

3) The ability to host lithium ions should be high to give satisfactory gravimetric and volumetric capacity;

4) The ionic and electric conductivities should be high to guarantee small polarization during charge and large operation current;

5) The structure of cathode material should be thermally stable and with no disordered ions pinning in lithium sites;

6) The volume should not expand/contract too much with lithium insertion/deinsertion to ensure cycling stability.

1.1.2 Structural and Electrochemistry

It was recently found that olivine-structured oxyanion scaffolded materials provide interesting possibilities. Those materials consist of corner-sharing MO_6 (M = Fe, Ti, V or Nb) octahedra and XO_4 (X = S, P, As, Mo or W) tetrahedral anions [3]. The redox potentials of Fe^{3+}/Fe^{2+} and V^{4+}/V^{3+} couples lie at a higher level in the phosphate polyanions PO_4^{3-} than in their oxidized forms [4]. The creative work of Goodenough and coworkers motivated the use of $LiFePO_4$ as a positive cathode material for lithium-ion batteries [5]. Figure 1.3 demonstrates charge/discharge curves for secondary lithium batteries using $LiFePO_4$ cathode material [6]. It was found that a high theoretical capacity of 165 mAh/g and a flat discharge voltage at 3.4 V versus Li/Li^+ can be achieved from $LiFePO_4$–assembled batteries. This kind of battery also has high thermal and chemical stability, and possesses the advantages of low cost [7] and small environmental impact [8]. However, it has the drawback of less good rate capability due to its poor electrical conductivity and slow ionic diffusivity [9, 10]. To overcome these barriers, much effort has been made, such as size reduction, uniformity improvement, metal dispersion, carbon coating, etc.

1.1.3 Material Synthesis Methods

As is well-known, the electrochemical behavior of $LiFePO_4$ is strongly influenced by its preparation methods. $LiFePO_4$ has conventionally been synthesized by a solid-state reaction that involves successive steps of grinding and annealing at high temperatures for long periods of time. The main steps are as follows: stoichiometric starting materials are mixed by the ball milling method; then the mixture is heated to around 300–400 °C to decompose any organic compound involved; it is subsequently annealed at around 500–800 °C to form and fully crystallize the desired phase [11]. The solid-state method has several disadvantages, such as large particle size, broad particle size distribution, and the low conductivity of the as-synthesized products. Thus, carbon is added to increase the conductivity of the cathode. The post synthesis addition of carbon leads to its inhomogeneous distribution surrounding the $LiFePO_4$ particles.

Recently, researchers developed some excellent solution-based techniques for the synthesis of $LiFePO_4$/C composites with carbon homogeneously distributed around the $LiFePO_4$ particles [12, 13]. Typical solution-based techniques, such as hydrothermal processing, sol–gel processing, precipitation, emulsion-drying and spray pyrolysis, are effective methods for the synthesis of olivine-structured materials [14]. The sol-gel process is incredibly versatile, allowing for a wide selection of precursor materials and carbon sources. This technique also allows for the synthesis of particles with excellent morphology and uniform size distribution of small particles, while offering a high purity and homogeneity at low processing temperatures. Figure 1.4 shows the microstructures of $LiFePO_4$ synthesized by sol-gel technique. The carbon incorporation during the synthesis process helps reduce the particle size and increase the electric conductivity [15]. One

concern about the heat treatment procedure is the temperature range. According to Kepler‘s report, the preparation process should be below a temperature of around 600 °C, or errant Fe ions will exist on the Li sites and reduce the reactivity and diffusion of the lithium ions [16].

1.2 Previous Research on High-Capacity Polyanionic Cathodes

Lithium-ion batteries are widely used in portable computers, entertainment devices, telecommunications, and recent automobiles. Their usage in HEV (hybrid electrical vehicles) and EV (electrical vehicles) requires of them higher voltage and larger capacity, as well as suitability for large scale production. The specific capacity needs to be increased above 200 mAh/g. Currently available cathode materials cannot fulfill these requirements very well. For example, lithium transition metal oxides, such as $LiCoO_2$, etc., have shown voltage around 4 V and gravimetric capacity of 150 mAh/g [17]. Limited by the capacity and high price, they only found application in small-scale and expensive devices, such as cell phones and laptops. From 1996, research on polyanionic compounds resulted in another commercially successful cathode material – $LiFePO_4$. Though it is cheap, structurally stable and environmentally benign, it has a capacity of less than 170 mAh/g [18]. Therefore, we still have to develop cathode materials which have capacities over 200 mAh/g and are cheap enough for large scale usage.

1.2.1 High-Potential Strategy

Besides the specific capacity, the redox potential of the cathode materials should be properly increased. High potential cathode is especially preferred when coupled with high potential anode materials, such as lithium titanates to obtain a safe cell with

moderate voltage [19]. In addition, the developments on solid-state electrolytes stable up to 6 V are currently underway, making the high-potential cathode materials even more favorable [20].

For achieving high capacity, high potential cathode materials, researchers have focused on improving the capacity of polyanionic materials by altering the transition metal and/or the type of polyanions. Up to date, two types of polyanion structures have attracted a lot of attention. The first type is $LiMXO_4$ (M: transition metal; X = P, As, Si, Ge) of one lithium per formula [21-23]. Most of these materials are of olivine-type structure with octahedral MO_6. The specific capacities were found to be below 170 mAh/g and their voltages range from 3.1 V ($LiFeGeO_4$) to 4.8 V ($LiCoPO_4$) [24]. Dompablo et al. reported that the lithium insertion voltage displayed a positive linear dependence on Mulliken X electronegativity (see Figure 1.5). In other words, they illustrated that the deinsertion voltage increases with the energy penalty for taking an electron away from an M ion [24]. This discovered rule would direct the design of cathode materials of desired potential.

1.2.2 Multiple Lithium Strategy

The second type of polyanionic materials is the monoclinic $LixM'_2(YO_4)_3$ ($x > 1$, M': transition metal; Y: S, P, Mo), among which $Li_3V_2(PO_4)_3$ (LVP) has been extensively studied due to its high theoretical capacity of 198 mAh/g with all three lithium atoms removed [25, 26]. Also, LVP exhibits a higher chemical diffusion coefficient of lithium ions at a large temperature range and maintains much higher reversible capacity at low temperature (-20 °C), compared to olivine $LiFePO_4$ [27]. These advantages in kinetics, such as higher ion diffusion coefficient, smaller polarization and smaller charge transfer

resistance, result from the relatively high ionic conductivity of monoclinic LVP with connected lithium polyhedral [27]. However, the charge profile has four voltage plateaus making it incompatible with practical devices. Moreover, vanadium is not environmentally benign.

Very recently, a new polyanionic material – $Li_2FeP_2O_7$ (LFPO) has been considered as a candidate for lithium-ion batteries in HEV [28]. The crystal structure of the material is shown in Figure 1.7. It has a theoretical capacity of 220 mAh/g with both lithium atoms extracted. However, only one of the lithium ions has been successfully removed, resulting in 110 mAh/g. This is due to the high voltage needed for the second lithium removal at 5.2 V which exceeds the stable voltage window of liquid organic electrolytes [29]. However, this problem may be solved by the development of the solid-state electrolyte. Another problem for LFPO is the slow electronic and ionic conductivity which we believe can be improved by deducing the particle size and coating the particles with carbon as in the case of $LiFePO_4$ [30]. Therefore, research on modification of LFPO is desired.

1.3 Review of Various Electrolytes for LIBs

Along with the anode and cathode, the electrolyte as the ionic transport media between them, has been explored and analyzed extensively. So far, four main types of electrolytes have been under careful inspection: conventional liquid, ionic liquid, solid polymer and inorganic solid electrolytes. They each have preferences for coupling with different electrodes and operation conditions. A good combination of electrodes and electrolyte affords excellent electrochemical performance and guarantees safety. Accordingly, it is crucial to choose the most suitable electrolyte when designing a new

lithium-ion battery. The related considerations and handling precautions are discussed below.

1.3.1 Conventional Liquid Electrolyte

In earlier times (1970s), lithium perchlorate in propylene carbonate-dimethoxyethane mixtures was used as the electrolyte and coupled with lithium metal to assemble secondary lithium batteries [31]. It took almost 10 years for the emergence of the ethylene carbonate-added (EC) electrolyte. Soon it gained attention, owing to a sustainable improvement of charge-discharge performance [32]. As is well-known, EC works as an active material that decomposes on the anode surface to form a solid electrolyte interlayer (SEI) when charged to around 0.8 V versus Li^+/Li during the first half cycle. The SEI is composed of mainly two layers. The inner layer closer to the electrode is more densified and comprised of lithium salts like LiF, Li_2O, and lithium carbonate, while the outer layer is polymorphous and is comprised of lithium polymers, such as dilithium butylene dicarbonate $Li_2(OCO_2(CH_2)_2OCO_2)_2$ and Lithium ethylene dicarbonate $(CH_2OCO_2Li)_2$, etc. [33]. In most of today's liquid electrolyte lithium-ion batteries in ambient temperature, EC, whose melting point is 36.8 °C, is used in mixture with one or two low melting point carbonates (e.g., dimethyl carbonate, diethyl carbonate). These carbonates are aprotic, polar and of high dielectric constant; hence, they are able to solvate lithium salts to more than 1 M. The lithium salts widely used in current research and commercial LIBs are $LiPF_6$ and sometimes $LiClO_4$. However, realized in this century, novel lithium bis-oxalatoborate, LiBOB, shows better electrochemical performance than $LiPF_6$ dissolved electrolyte [34]. Anyway, the improvement is not large.

The liquid electrolytes of carbonates with dissolved lithium salts are electrochemically stable under 5.5 V and, thus, can satisfy most of the high potential electrodes [35]. Their high ionic conductivity of larger than 10^{-3} S/cm also improves their popularity. Even though they are used extensively for commercial and household applications, there are problems concerning safety and the environment. Since the solvents are flammable, the battery may catch fire or even explode if it shorts accidentally. The solvents are also toxic and should be dealt with cautiously. Additionally, the limited operating temperature range (–20 to 50 °C) and voltage range fall short in severe natural conditions.

1.3.2 Ionic Liquid Electrolyte

Starting in the 1980s, interest in room temperature ionic liquid electrolyte persists. Room temperature ionic liquid (RTIL) is also called room temperature molten salt, with melting points below room temperature. Countless types of ionic liquids have been evaluated as liquid electrolytes, especially in the 10 ten years. To make it simple and clear, a molten salt is represented by $[A^+][X^-]$, the cation and anion. The most commonly used RTIL are quaternary ammonium salts, such as tetraalkylammonium $[R_4N^+]$. The counter anions can be organic or inorganic, such as $[BF_4^-]$, $[PF_6^-]$, $[AsF_6^-]$, triflate $[CF_3SO_3^-]$, imide $[N(CF_3SO_2)_2^-]$ and $[N(F_2SO_2)_2^-]$ [36]. When they are used as the electrolyte in the cell, lithium salt $[Li^+][X^-]$ is added, forming $[Li^+][A^+][X^-]$ ionic liquid. The lithium salt is often lithium bis(trifluoromethanesulfonyl)imide (LITFSI) instead of $LiPF_6$ in carbonate solvents. LiTFSI became popular recently, since it can greatly improve the ionic conductivity of solid polymer electrolytes (as discussed in the next section). Their features have been thoroughly studied and the relationships between those

characteristics and electrochemical behavior inside the lithium-ion batteries are addressed in this section.

One of the most promising RTILs is PP13–TFSI (N-Methyl-N-propylpiperidinium bis(trifluoromethanesulfonyl)imide), reported by Sakaebe and coworkers. They prepared a room temperature ionic liquid composed of quaternary ammonium cation and imide anion. This novel salt was tested in a $Li/LiCoO_2$ cell and showed very good performance of more than 97% Coulombic efficiency at the C/10 cycling rate and 85% of the capacity at C/2 [37]. This high Coulombic efficiency was attained, indicating less decomposition of electrolytes and a thinner SEI. The formation of SEI is the basic and most important factor determining the quality of the electrolyte. Generally speaking, however, the cycling ability of $Li/RTIL/LiCoO_2$ is not as good as that of $Li/LiPF_6$ in $EC:DMC/LiCoO_2$. The addition of molecular additives to ionic liquid has been proved to be the most effective method, since they form a protective coating on the surface of electrodes.

A controversial issue in room temperature ionic liquids is the viscosity. The ionic liquid has much higher viscosity than that of water, normally in the range of 30–50 cP. This is the result of strong Coulombic interaction between ions. Accordingly, the vapor pressure is always low for ionic liquids, which is very good because low vapor pressures reduce flammability. But the highly viscous liquid makes it difficult to fill the gaps between electrode particles. Thus, special treatment is required to improve the contact between the electrolyte and electrodes, for instance, setting them together for a long time under low ambient pressure [38]. Though there are many problems yet to be solved, research interest in RTIL never drops due to the importance of safety issues.

1.3.3 Solid Polymer or Gel Electrolyte

Solid polymer electrolyte is most attractive when considering thin-film batteries. These thin-film cells can be packed together, forming a high voltage or high rate battery while being flexible. Besides, the cost and reliability of solid polymer electrolytes are appealing. In contrast to various liquid electrolytes, the high-molecular weight polymers for solid electrolytes are limited to polyethylene oxide (PEO). Because of the low ionic conductivity and solid state, they are suitable for application in thin-film batteries where the limited thickness increases their conductance.

A high temperature (60–80 °C) is needed to keep the PEO from crystallizing; thus, the ionic conductivity of amorphous PEO can reach a useful value of about 10^{-4} S/cm. Hence, effort has been placed on improving the ionic conductivity of the polymer electrolyte at room temperature. One of the most effective methods is to add liquid plasticizers, but this promotes problems such as deterioration of the mechanical strength and risk of reaction with the lithium metal anode. Croce et al. reported in 1998 that nanosized ceramic powders of TiO_2 and Al_2O_3 can be added in as solid plasticizers to lower the operation temperature of PEO [39]. They achieved ionic conductivity of 10^{-5} at 30 °C, which is more than 3 orders of magnitude higher than plasticizer-free PEO. They opened a new area in raising the ionic conductivity of the solid electrolyte; however, no other techniques for new and better plasticizers were reported to improve the performance. Therefore, solid-electrolyte-lithium-ion batteries are only favorable when the operation temperature is above 60 °C. Other approaches about polymer development have been investigated as well. Hammond and Delongchamp designed a polymer comprised of PEO/PAA (poly(acrylic acid)) in a layer-by-layer configuration [40]. The

molecular weight of the integrated film can be very high due to the low PEO/PAA cross-link density. Even though they attained an ionic conductivity of 10^{-4} S/cm, the requirement of pre-exposure to humidity (for achieving better conductivity) does not seem suitable in humidity-sensitive lithium ion battery applications.

Although large amounts of effort have been focused on enhancing the ionic conductivity of polymer electrolytes, the progress has not been sufficient to allow practical operation at room temperature. Despite this, polymer electrolytes continue to stimulate researchers' thoughts regarding polymer design and additive materials. The reason is that in terms of their cost and safety, they outperform all liquid electrolytes.

1.3.4 Inorganic Solid Electrolyte

Inorganic solid electrolytes are pointing to fast ion conducting lithium glasses and ceramics, where lithium ions move within a naturally static framework. The fast ionic conduction mechanism describes the lithium ion movement by rotational disorder and vacancies existing in the crystal structures of the electrolyte. As the same in polymer solid electrolytes, inorganic solid electrolytes are supposed to be safe (no leakage or pollution), economical and suitable for thin-film batteries. The problem associated with this type of electrolyte is low ionic conductivity at room temperature, which greatly limits their practical application. There are various kinds of fast ionic conductors for not only lithium, but also monovalent protons, sodium, silver, potassium, copper, and fluoride ions [41]. But herein, we only discuss the lithium ionic conductors and their applications.

The lithium ionic conductors here can be divided into three groups. The first is perovskite-type—$RE_{2/3-x}Li_{3x}TiO_3$ (RE: rare earth ion). Much work has been done on lithium lanthanum titanates since 1993 when Inaguma et al. [42] reported a very high

lithium conductivity of 10^{-3} S/cm for bulk $La_{0.5}Li_{0.34}TiO_{2.94}$ at room temperature. This is a very impressive ionic conducting electrolyte; however, its performance is reduced when used in batteries since grain boundaries exist for polycrystalline electrolytes. The main factor limiting its usage is the large amount of lithium intercalation that occurs when the operation potential is around 1.2 V. This will also cause the coexistence of Ti^{4+} and Ti^{3+}, leading to increased electronic conductivity [43]. The second kind of lithium ionic conducting solid electrolyte is of a three-dimensional structure (LISICON) similar to the well known Na super-ionic conductor (NASICON). The composition is set to be $Li_{1+x}M_{2-x}M'_xP_3O_{12}$, where M = Ti, Ge or Hf and M′ = Al or In. They have shown a good ionic conductivity of $2–8\times10^{-4}$ S/cm at around 25 °C [44]. But in practice, the grain boundaries increase the difficulty of ion transport by promoting scattering sites, inducing a drop in conductivity to 10^{-5} S/cm. The third kind of lithium ionic conductor electrolyte is garnet-structured glasses. Garnet-type lithium ion conductors have attracted lots of attention as potential solid-state electrolytes for lithium-ion batteries, due to their structural stability and the possibility of achieving higher and higher ionic conductivity. The typical structure of garnets is $A_3B_2C_3O_{12}$, which is constructed of CO_4 tetrahedra and BO_6 octahedra that are connected by shared corners, forming triangular dodecahedral AO_8 that share edges both with tetrahedral and among themselves. The cations in the octahedral and dodecahedron cages can be replaced by different elements without much change of the crystal framework, therefore, the structure and stoichiometry of garnets can vary a lot. For example, in $Li_3Ln_3B_2O_{12}$ garnets, the B atom in the octahedral site can be Te or W, and *L*n can be La, Pr, Nb, Ga, etc. However, they have almost immeasurable ionic conductivity at room temperature. A step-further, research about increasing the

number of lithium per formula unit above 3 resulted in a 3 orders of magnitude increase of ionic conductivity in $Li_5Ln_3B'_2O_{12}$ (B'=Bi, Sb, Na, Ta), where *Ln* can be substituted by group II elements to further increase the lithium content per formula unit. $Li_6BaLa_2Ta_2O_{12}$ is the most attractive, due to its high bulk ion conductivity of $4x10^{-5}$ S/cm and high electrochemical stability of 6 V versus Li^+/Li at room temperature [45]. Recently, $Li_7Ln_3B''_2O_{12}$ (B''=Zr, Hf, Sn) have attracted a lot of attention since the ionic conductivity was increased about 1 order of magnitude higher than the Li_5 garnets. In this group, $Li_7La_3Zr_2O_{12}$ (LLZO) has attracted the most attention due to its high ionic conductivity approaching 10^{-3} S/cm at room temperature, as well as good compatibility with lithium metal and stability in air. $Li_7La_3Zr_2O_{12}$ is also one of our focuses in this dissertation.

The crystal structure of LLZO in the cubic Ia-3d phase is shown in Figure 1.8. The high ionic conductivity of LLZO is mostly due to three reasons: (i) isotropic three-dimensional lithium diffusion path, (ii) short Li-Li distance, and (iii) low rates of occupancy at the Li sites (enhanced by Al^{3+} substitution of $3Li^+$) [46]. Originally, LLZO possess a tetragonal phase of $I4_1/acd$ space group at room temperature, and the three lithium sites are fully occupied due to cation ordering; and the lithium conductivity is 1 order of magnitude lower than that of Li_5 garnets. However, it was newly found that Al doping can obstacle the cation ordering and stabilize the cubic Ia-3d phase at room temperatures [47], and the ionic conductivity of the stabilized cubic phase is 2 orders of magnitude higher than that of the tetragonal LLZO. The full understanding of the mechanism behind for Al doping is still underway.

Finally, we draw a conclusion on these different kinds of liquid and solid electrolytes. For conventional coin cells or prismatic cells, liquid electrolyte of $LiPF_6$ in EC-DMC takes more than 90% weight. And the lithium salt of LiTFSI was recently shown to exhibit stability toward electrodes. Thus, attempts have been made to add it both in carbonate solvents and ionic liquids to form a novel liquid electrolyte. As for the progress of solid polymer and inorganic electrolytes, their use in thin-film batteries becomes more and more widespread. However, more types of polymers should be included and an understanding of the additives should also be improved. As well, fast ion conductors are developing very fast right now, e.g.,, the newly developed $Li_7La_3Zr_2O_{12}$ garnet is the most attractive.

1.4 Brief Review of Thin-Film Batteries

Thin-film batteries are classified by small thickness, ranging from several microns to several millimeters. Their areas can be minimized to 100×100 μm^2 or enlarged to around 20 cm^2. The concept of designing thin-film batteries is the deposition of thin films of anode, electrolyte and cathode, sequentially on a substrate. The typical features of this kind of battery are very unique, compared to conventional coin, cylindrical and prismatic cells. Additionally, they are reported to have higher volumetric and gravimetric energy densities, power capabilities and superior design flexibility. We will discuss the similarities and differences of thin film and conventional secondary lithium batteries.

1.4.1 Materials and Methods

Many types of cathodes, anodes and electrolytes have been investigated in thin-film batteries. Most of them use lithium metal as the anode, LiPON as the electrolyte and

lithium transition metal oxide as the cathode. For instance, Wang et al. [48] presented their work on the deposition of lithium metal by thermal vaporization and $LiCoO_2$, LIPON by radio-frequency sputtering. The obtained films have thicknesses of 0.05–0.5 μm, 3 μm and 1~2 μm for $LiCoO_2$, lithium and LIPON, respectively. They obtained very impressive results from the cell comprised of 0.05 μm thick $LiCoO_2$. Capacity fading of 0.0001% per cycle was achieved. And the 0.5 μm thick layer showed capacity fading of 0.002% per cycle for the same discharge depth. The better cyclability of thinner films results from released strain. With less strain, the structure can be maintained while cycling, thus the resistance caused by structure deformation can be suppressed. Therefore, thin-film batteries benefit from the small thickness of electrodes.

Similar to conventional lithium-ion cells, thin-film batteries suffer from problems such as volume expansion during charge/discharge cycles, side reactions between nanoscale electrodes and electrolytes, and low ionic conductivities of cathode and electrolyte. Differing from other lithium-ion cells, thin-film batteries have issues of high cost from thin film deposition techniques, but may provide solutions to many problems via modification of the nanostructured materials. Therefore, it is very useful to investigate thin film techniques and their impact on the structures and electrochemical performances of battery materials. Normally, the lithium metal is grown by vacuum thermal vapor deposition and the solid cathode and electrolyte are deposited by various techniques: radio frequency (RF) sputtering, RF magnetic sputtering, chemical vapor deposition (CVD), e-beam evaporation deposition, electrostatic spray deposition (ESD), pulsed laser deposition (PLD) or sol-gel coating, etc.

1.4.2 Applications

A very attractive area of thin-film batteries is the microscaling of battery arrays, which are called smart cards. They are widely used and demanded for fingerprint scanners, face recognition, hand geometry, eye scanners, signature verification and voice recognition [49]. West et al. [50] reported all-solid state microscale thin-film batteries in 2002. They prepared batteries as small as 50×50 μm^2 by photolithography. The batteries were arranged in parallel and serial to yield higher voltage or capacity. Figure 1.9 shows the series arrangement of the micro-batteries. The big squares are metal contacts and the small dark areas are active batteries. The obtained voltage for each cell is 3.9 V and the current is 10 $\mu A/cm^2$. However, they observed a short cycle life of tens of cycles due to contamination in the electrodes and electrolyte during etching. The electrolyte used in thin-film batteries can also be a liquid electrolyte. The transition from liquid to solid electrolyte solves the problem of leakage and ensures higher mechanical strength.

Briefly speaking, thin-film batteries take advantage of small thicknesses, which benefit the less ion conductive electrode and electrolyte materials. It also has problems similar to other lithium-ion batteries, including large volume change, cycling instability, etc. The developments of anode materials as carbon and lithium alternatives are popular focal points, since they possess much higher capacity than graphite and are safer than lithium. Since the weight and volume of thin-film batteries are small, the ratio of pre-packed material over a packed cell should be as large as possible. So, it requires a rational distribution of anode, cathode, electrolyte, collectors and outer shell. Besides, the mechanical strength is important, since it relates to the tolerance to be bent or pressed.

Further, the condensed serial package of thin films can give a high voltage, thus, the design of thin film cells is carefully considered.

1.5 Motivations and Objectives

Structure modification of current polyanionic cathode materials has been found to improve the overall performance of cathode. Detailed study on the effect of synthesis parameters is needed to obtain the maximum benefit on improving the specific capacity of cathode materials. Specific emphasis has been focused on the role of chelating agent type, chelating agent amount and sintering temperature.

Solid-state electrolyte of $Li_7La_3Zr_2O_{12}$ with a garnet-like structure was recently developed by solid-state method which is time and energy consuming. For achieving high-quality $Li_7La_3Zr_2O_{12}$ in a cost-effective way, a solution-based technique needs to be developed where most of the steps are carried out at low temperatures. Moreover, as a good solid-state electrolyte for lithium-ion batteries, the interfacial resistance between the electrolyte and electrode should be diminished. In this sense, an attempt has been made to deposit $Li_7La_3Zr_2O_{12}$ thin films which are supposed to have lower interfacial resistance when coupled with electrode films deposited by vapor-phase techniques.

The objectives of this work are described as follows:

(1) Investigate the effect of chelating agent on the structure and performance of the $LiFePO_4$ cathode composite.

(2) Synthesis and characterization of $Li_2FeP_2O_7$ cathode composite.

(3) Synthesis of $Li_7La_3Zr_2O_{12}$ garnet and study of its potential as solid-state electrolyte in prototype lithium-ion cells.

(4) Fabrication of $Li_7La_3Zr_2O_{12}$ thin films as potential electrolyte for lithium-based thin-film batteries.

1.6 References

1. Gao XP and Yang HX (2010) Multi-electron reaction materials for high energy density batteries. Energy Environ. Sci. 3: 174–189.

2. Greatbalch W, Lee JH, Schneider AA and et al. (1971) Solid-state lithium battery. A new improved chemical power source for implantable cardiac pacemakers. IEEE Transactions on Biomedical Engineering 18: 317–324.

3. Padhi AK, Nanjundaswamy KS, Masquelier C, Okada S and Goodenough JB (1997) Effect of structure on the Fe^{3+}/Fe^{2+} redox couple in iron phosphates. Journal of Electrochem. Soc. 144: 1609–1613.

4. Tarascon JM and Armand M (2001) Issues and challenges facing rechargeable lithium batteries. Nature 414: 359–367.

5. Padhi AK, Nanjundaswamy K. and Goodenough JB (1997) Phospho-olivines as positive-electrode materials for rechargeable lithium batteries. Journal of Electrochem. Soc. 144: 1188–1194.

6. Chung SY, Bloking JT and Chiang YM (2002) Electronically conductive phospho-olivines as lithium storage electrodes. Nature Materials 1: 123–128.

7. Ritchie A and Howard W (2006) Recent developments and likely advances in lithium-ion batteries. Journal of Power Sources 162 : 809–812.

8. Sauvage F, Baudrin E, Gengembre L and Tarascon JM (2005) Effect of texture on the electrochemical properties of $LiFePO_4$ thin films. Solid State Ionics 176: 1869–1876.

9. Kim JK, Choi JW, Chauhan GS, Ahn JH, Hwang GC, Choi JB and Ahn HJ (2008) Enhancement of electrochemical performance of lithium iron phosphate by controlled sol–gel synthesis. Electrochimica Acta 53: 8258–8264.

10. Hsu KF, Tsay SY and Hwang BJ (2005) Physical and electrochemical properties of LiFePO4/carbon composite synthesized at various pyrolysis period. Journal of Power Sources 146: 529–533.

11. Koltypin M, Aurbach D, Nazar L and Ellis B (2007) More on the performance of $LiFePO_4$ electrodes—The effect of synthesis route, solution composition, aging, and temperature. Journal of Power Sources 174: 1241–1250.

12. Choi D and Kumta PN (2007) Surfactant based sol–gel approach to nanostructured $LiFePO_4$ for high rate Li-ion batteries. Journal of Power Sources 163: 1064–1069.

13. Lin Y, Pan H, Gao M and Liu Y (2007) Effects of reductive conditions on the microstructure and electrochemical properties of sol-gel derived LiFePO4/C. Journal of the Electrochemical Society 154: A1124–A1128.

14. Jugović D and Uskoković D (2009) A review of recent developments in the synthesis procedures of lithium iron phosphate powders. Journal of Power Sources 190: 538–544.

15. Huang H, Yin SC and Nazar LF (2001) Approaching theoretical capacity of $LiFePO_4$ at room temperature at high rates. Electrochem. Solid-State Lett. 4: A170–A172.

16. Kepler KD, Vaughey JT and Thackeray MM (1999) $LixCu_6Sn_5$ ($0<x<13$): an intermetallic insertion electrode for rechargeable lithium batteries. Electrochem. Solid State Lett. 2, 307–358.

17. Cao Q, Zhang HP, Wang GJ, Xiao Q, Wu YP and Wu HQ (2007) A novel carbon-coated $LiCoO_2$ as cathode material for lithium ion battery. Electrochemistry Communications 9: 1228-1232.

18. Wang Y, Wang YG, Hosono E, Wang K and Zhou H (2008) The design of a $LiFePO_4$/Carbon nanocomposite with a core–shell structure and its synthesis by an in situ polymerization restriction method. Angew. Chem. Int. Ed. 47: 7461–465.

19. Whittingham MS (2004) Lithium batteries and cathode materials. Chem. Rev. 104: 427–4301.

20. Murugan R, Thangadurai V and Weppner W (2007) Fast Lithium Ion Conduction in Garnet-Type $Li_7La_3Zr_2O_{12}$. Angew. Chem. Int. Ed. 46: 7778–7781.

21. Amine K, Yasuda H and Yamachi M (2000) Olivine $LiCoPO_4$ as 4.8 V electrode material for lithium batteries. Electrochem. Solid-State Lett. 3: 178–179.

22. Guo H, Xiang K, Cao X, Li X, Wang Z and Li L (2009) Preparation and characteristics of Li_2FeSiO_4/C composite for cathode of lithium ion batteries. Transactions of Nonferrous Metals Society of China 19: 166–169.

23. Minakshi M, Singh P, Appadoo D and Martin D (2011) Synthesis and characterization of olivine $LiNiPO_4$ for aqueous rechargeable battery. Electrochimica Acta 56: 4356–4360.

24. Dompablo ME, Armand M, Tarascon JM and Amador U (2006) On-demand design of polyoxianionic cathode materials based on electronegativity correlations: An exploration of the Li_2MSiO_4 system (M = Fe, Mn, Co, Ni). Electrochemistry Communications 8: 1292–1298.

25. Ren MM, Zhou Z, Gao XP, Peng WX and Wei JP (2008) Core−shell $Li_3V_2(PO_4)_3$/C composites as cathode materials for lithium-ion batteries. J. Phys. Chem. C 112: 5689–5693.

26. Rui XH and Chen CH (2009) Synthesis and characterization of carbon-coated $Li_3V_2(PO_4)_3$ cathode materials with different carbon sources. Electrochimica Acta 54: 3374-3380.

27. Rui XH, Jin Y, Feng XY, Zhang LC and Chen CH (2011) A comparative study on the low-temperature performance of $LiFePO_4$/C and $Li_3V_2(PO_4)_3$/C cathodes for lithium-ion batteries. Journal of Power Sources 196: 2109-2114.

28. Nishimura S, Nakamura M, Natsui R and Yamada A (2012) New lithium iron pyrophosphate as 3.5 V class cathode material for lithium ion battery. J. Am. Chem. Soc. 132: 13596–13597.

29. Zhou H, Upreti S, Chernova NA, Hautier G, Ceder G and Whittingham MS (2011) Iron and manganese pyrophosphates as cathodes for lithium-ion batteries. Chem. Mater. 23: 293 – 300.

30. Gaberscek M, Dominko R and Jamnik J (2007) Is small particle size more important than carbon coating? An example study on $LiFePO_4$ cathodes. Electrochemistry Communications 9: 2778-2783.

31. Caïola A, Guy H and Sohm JCH (1970) Etude des systemes $Li/LiCH_3CO_2$, $Cu/Cu(CH_3CO_2)_2$ ET $Hg/Hg_2(CH_3CO_2)_2$ en milieu organique. Electrochim Acta 15:1733–1746.

32. Tobishima S and Yamaji A (1983) Electrolytic characteristics of mixed solvent electrolytes for lithium secondary batteries. Electrochimica Acta 28: 1067–1072.

33. Aurbach D (2000) Review of selected electrode–solution interactions which determine the performance of Li and Li ion batteries. Journal of Power Sources 89: 206–218.

34. Xu K, Zhang S, Jow TR, Xu W and Angell CA (2002) LiBOB as salt for lithium-ion batteries. A possible solution for high temperature operation. Electrochemical and Solid-State Letters 5: A26–A29.

35. Dominey LA (1994) Current state of the art on lithium battery electrolytes. Industrial Chemistry Library 5: 137–165.

36. Gali ski M, Lewandowski A and Stepniak I (2006) Ionic liquids as electrolytes. Electrochimica Acta 51: 5567–5580.

37. Sakaebe H and Matsumoto H (2003) N-Methyl-N-propylpiperidinium bis (trifluoromethanesulfonyl)imide (PP13–TFSI) – novel electrolyte base for Li battery. Electrochemistry Communications 5: 594–598.

38. Hayashi K, Nemoto Y, Akuto K and Sakurai Y (2005) Alkylated imidazolium salt electrolyte for lithium cells. Journal of Power Sources 146: 689–692.

39. Croce F, Appetecchi GB, Persi L and Scrosati B (1998) Nanocomposite polymer electrolytes for lithium batteries. Nature 394, pp. 456-458.

40. DeLongchamp DM and Hammond PT (2004) Highly ion conductive poly (ethylene oxide)-based solid polymer electrolytes from hydrogen bonding layer-by-layer assembly. Langmuir 20: 5403–5411.

41. Thangadurai V and Weppner W (2006) Recent progress in solid oxide and lithium ion conducting electrolytes research. Ionics 12: 81–92.

42. Inaguma Y, Liquan C, Itoh M, Nakamura T, Uchida T, Ikuto H and Wakihara M (1993) High ionic conductivity in lithium lanthanum titanate. Solid State Commun 86: 689–693.

43. Shan YJ, Chen L, Inaguma Y, Itoh M and Nakamura T (1995) Oxide cathode with perovskite structure for rechargeable lithium batteries. Journal of Power Sources 54: 397–402.

44. Xu X, Wen Z, Gu Z, Xu X and Lin Z (2004) Lithium ion conductive glass ceramics in the system $Li_{1.4}Al_{0.4}(Ge_{1-x}Ti_x)_{1.6}(PO_4)_3$ (x=0–1.0). Solid State Ionics 171: 207–213.

45. Thangadurai V and Weppner W (2005) Investigations on electrical conductivity and chemical compatibility between fast lithium ion conducting garnet-like $Li_6BaLa_2Ta_2O_{12}$ and lithium battery cathodes. Journal of Power Sources 142: 339–344.

46. Gerger CA, Alekseev E, Lazic B, Fisch M, Armbruster T, Langner R, Fechtelkord M, Kim N, Pettke T and Weppner W (2011) Crystal chemistry and staility of "$Li_7La_3Zr_2O_{12}$" garnet: A fast lithium-ion conductor. Inorganic Chemistry 50: 1089–1097.

47. Buschmann H, Dölle J, Berendts S, Kuhn A, Bottke P, Wilkening M, Heitjans P, Senyshyn A, Ehrenberg H, Lotnyk A, Duppel V, Kienle L and Janek J (2011) Structure and dynamics of the fast lithium ion conductor "$Li_7La_3Zr_2O_{12}$". Phys. Chem. Chem. Phys. 13: 19378–19392.

48. Wang B, Bates JB, Hart FX, Sales BC, Zuhr RA and Robertson JD (1996) Characterization of thin-film rechargeable lithium batteries with lithium cobalt oxide cathodes. Journal of Elect. Rochem. Soc. 143: 3203–3213.

49. Patil A, Patil V, Shin DW, Choi JW, Paik DS and Yoon SJ (2008) Issue and challenges facing rechargeable thin film lithium batteries. Materials Research Bulletin 43: 1913–1942.

50. West WC, Whitacre JF, White V and Ratnakumar BV (2002) Fabrication and testing of all solid-state microscale lithium batteries for microspacecraft applications. Journal of Micromechanics Microengineering 12: 58–62.

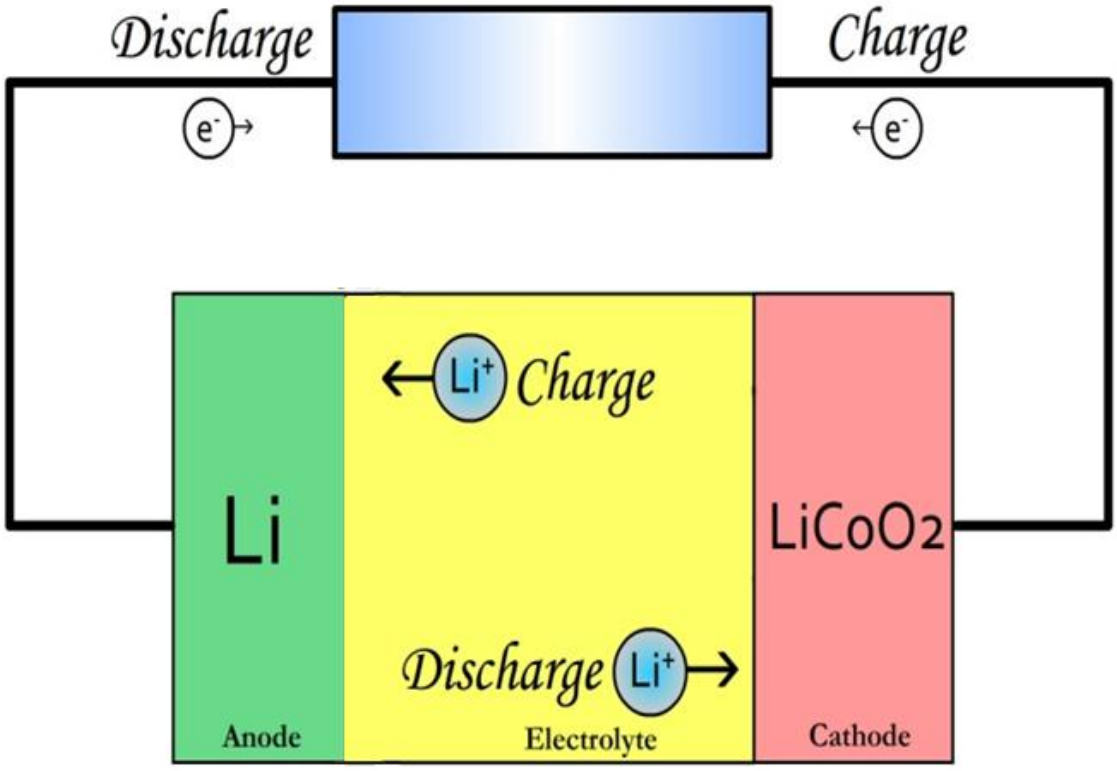

Figure 1.1. Operation of lithium-ion batteries.

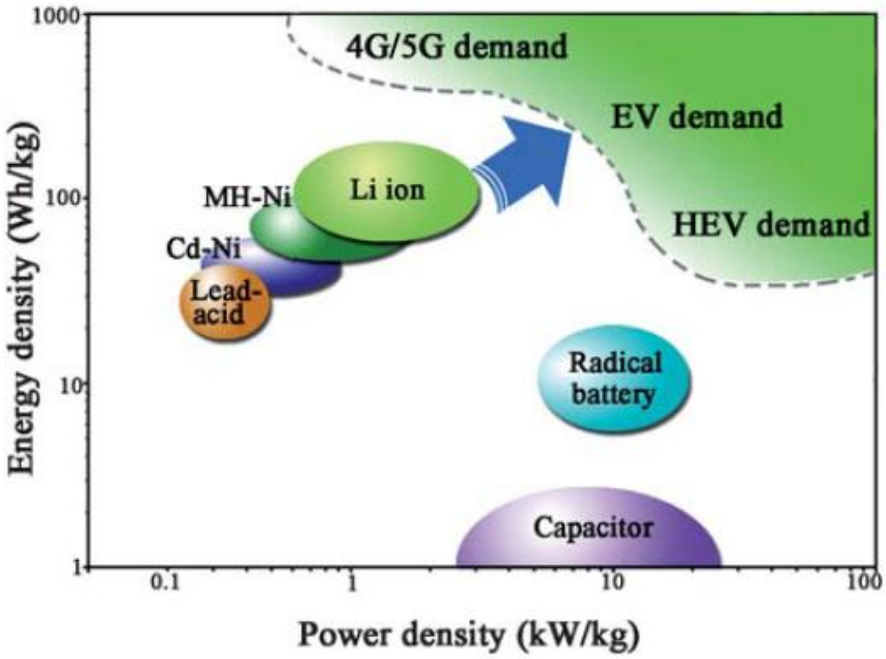

Figure 1.2. Schematic distribution of power density and energy density for different secondary batteries (from JM Tarascon (2001), with permission).

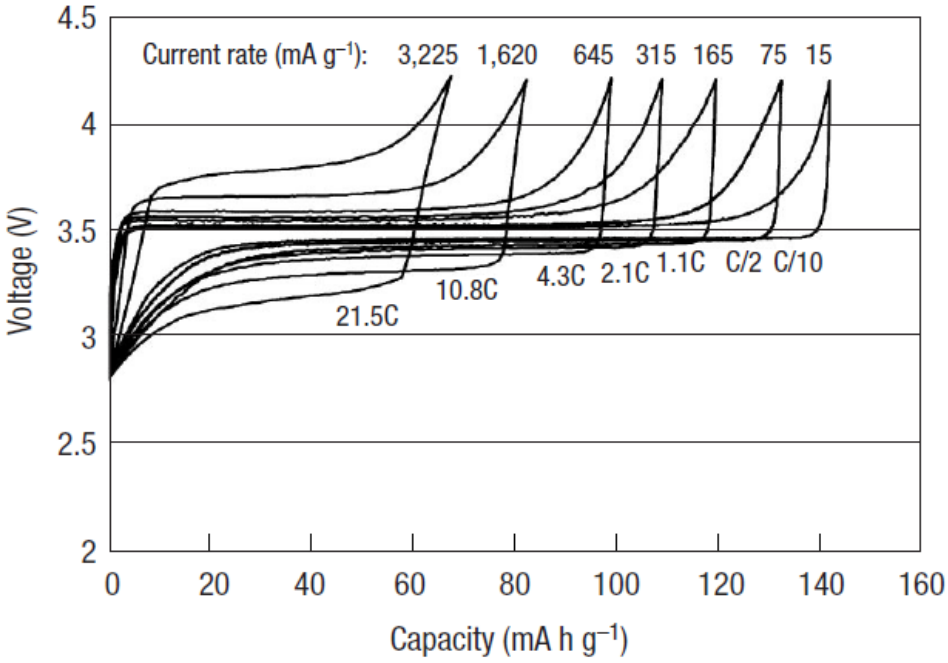

Figure 1.3. Charge-discharge curves for $LiFePO_4$ cathode materials at different rates (from SY Chung (2002), with permission).

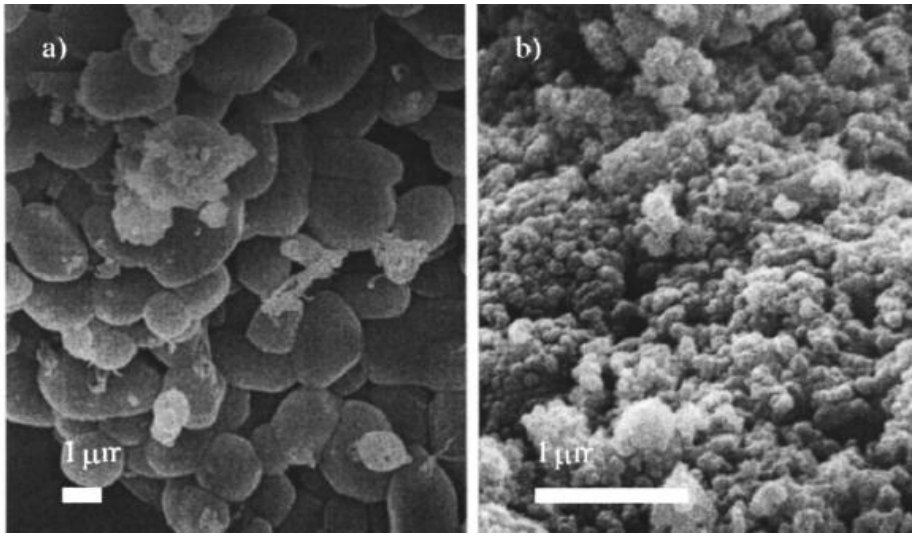

Figure 1.4. $LiFePO_4$ (a) without carbon, (b) with the oxidized carbon (from H Huang (2001), with permission).

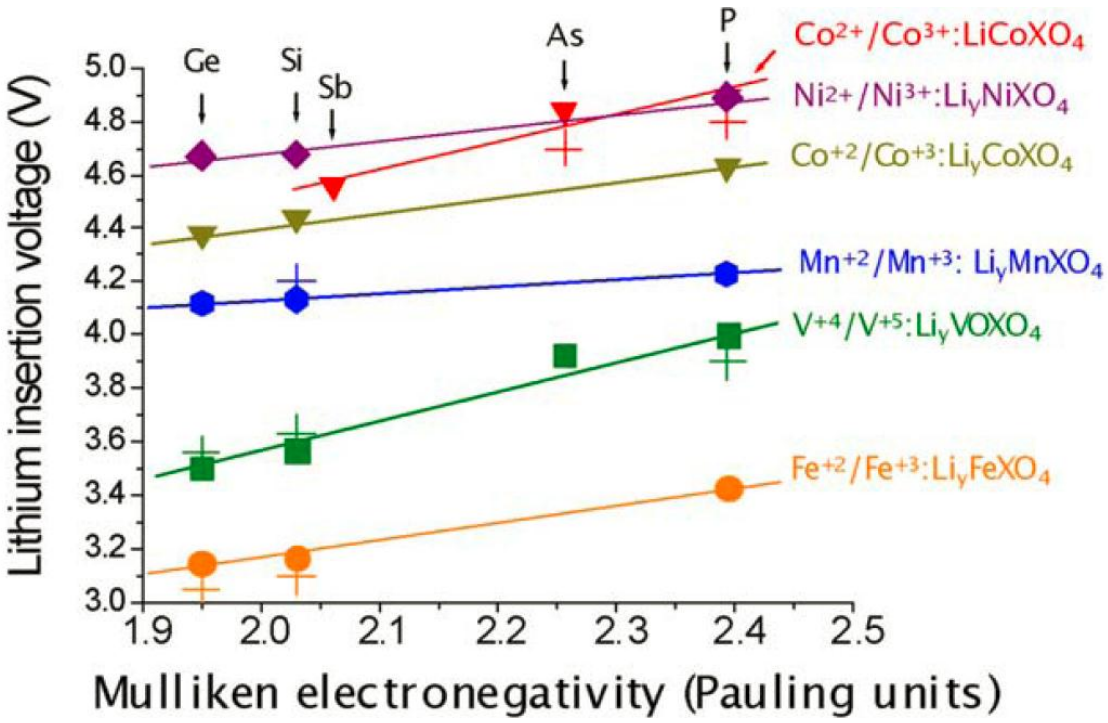

Figure 1.5. Calculated and experimental (crosses) lithium insertion voltage for polyoxianionic compounds vs. the X Mulliken electronegativity. The lines show the fit to respective linear functions (from ME Dompablo (2006), with permission).

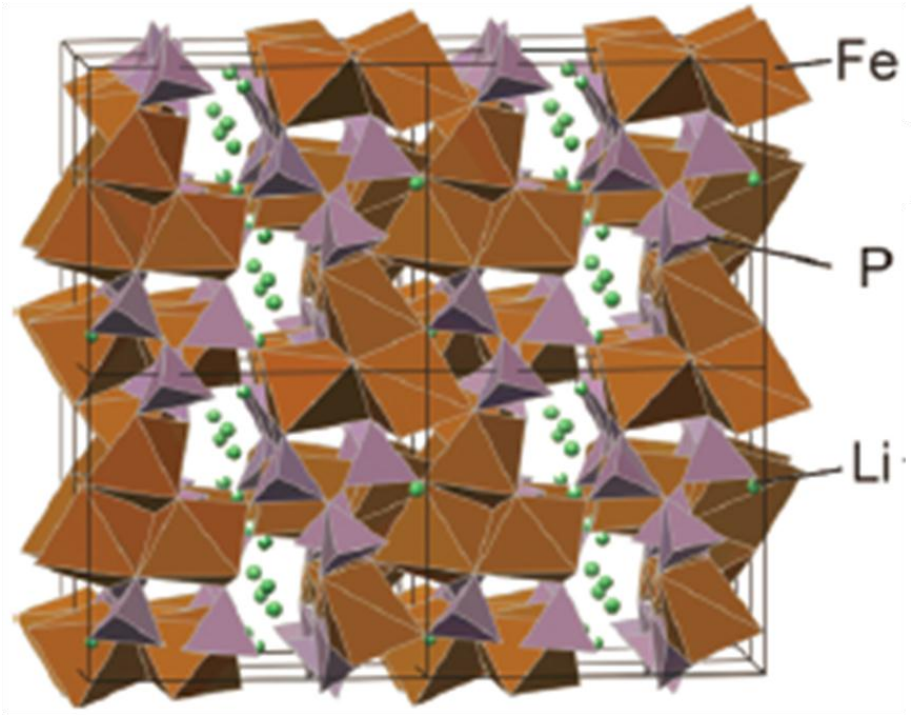

Figure 1.6. Crystal structure of $Li_2FeP_2O_7$. Reprint with permission from (Nishimura, S.; Nakamura, M.; Natsui, R.; Yamada, A. J. Am. Chem. Soc. 2010, **132**, 13596) Copyright (2010) American Chemical Society.

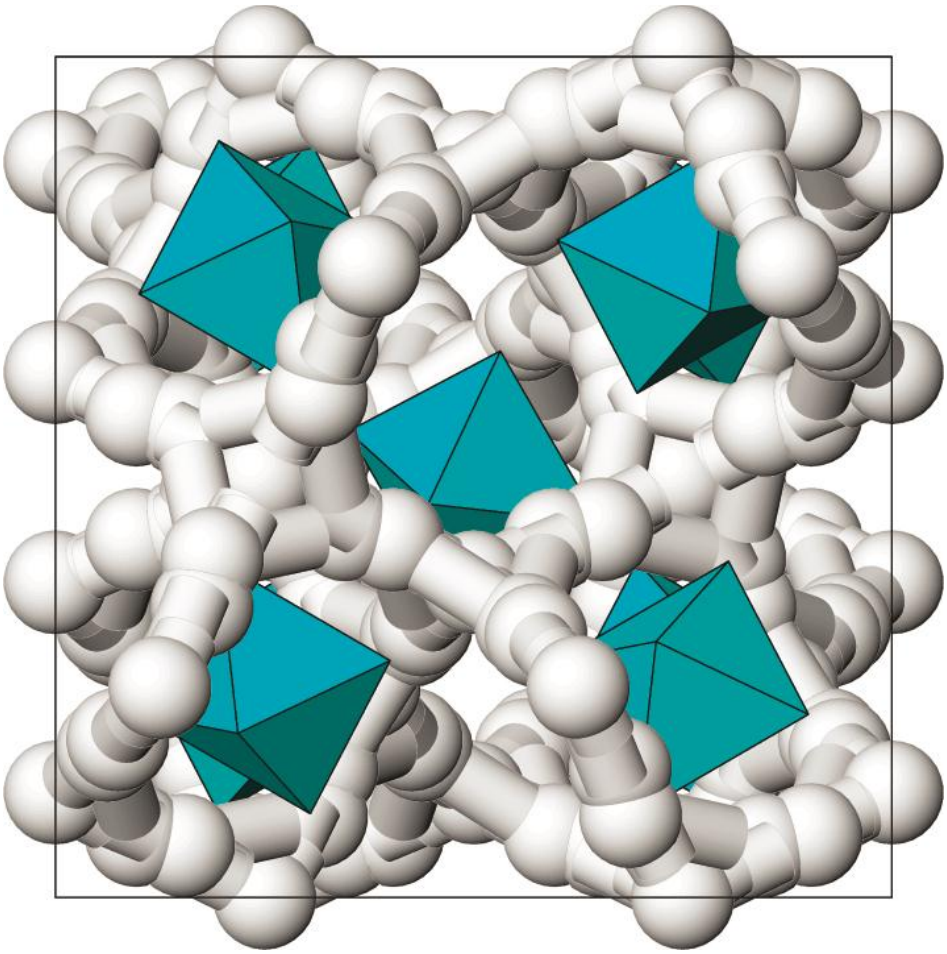

Figure 1.7. Crystal structure of Al-containing cubic phase $Li_7La_3Zr_2O_{12}$, projected on (100) plane. White spheres are Li sites, blue octahedral are ZrO_6, and La atoms have been omitted for clarity. Reprint with permission from (C.A. Gerger, E. Alekseev, B. Lazic, M. Fisch, T. Armbruster, R. Langner, M. Fechtelkord, N. Kim, T. Pettke, and W. Weppner, Inorganic Chemistry **50**, 1089) Copyright (2011) American Chemical Society.

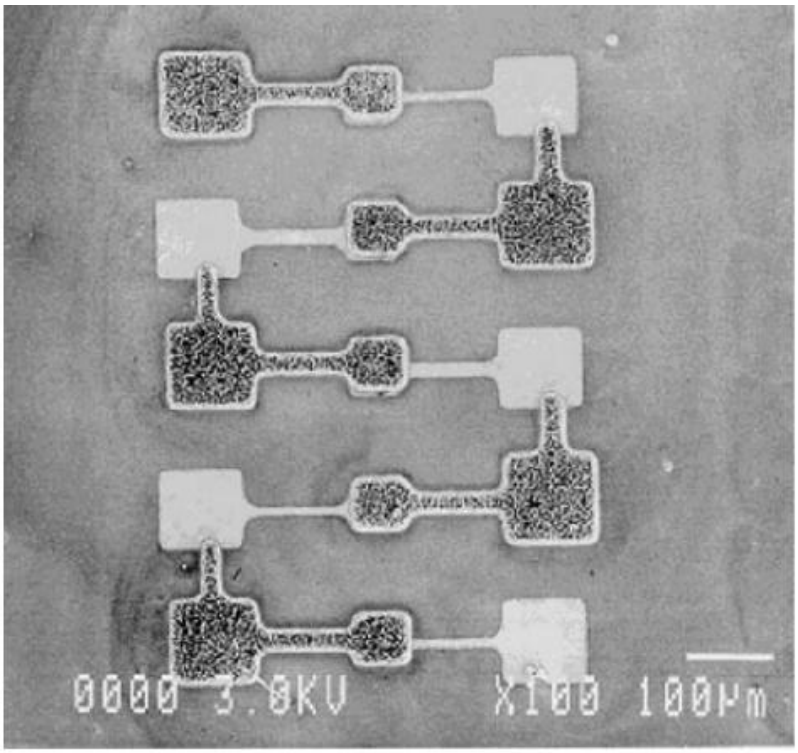

Figure 1.8. Micrograph of a five cell serial battery on a substrate. Reprint with permission from (West WC, Whitacre JF, White V and Ratnakumar BV, (2002) Fabrication and testing of all solid-state microscale lithium batteries for microspacecraft applications, J. Micromech. Microeng. 12: 58–62).

CHAPTER 2

EXPERIMENTAL TECHNIQUES

2.1 Processing

The cathode composite powders and the electrolyte ceramic pellet used in this dissertation were prepared by solution-based techniques. The 1 inch diameter target pellet used for thin film preparation by pulsed laser deposition (PLD) was also prepared by a solution-based technique.

2.1.1 Bulk Processing: Solution-Based Technique

Solution-based technique is a wet chemical processing technique that is commonly used to produce nanostructured or high surface area compounds. The solution-based process is a low temperature technique for fast production of homogenous single phase compounds like metal oxide, metal phosphate, etc. The chelating agent is a very crucial part for the successful synthesis of a pure phase, homogeneous product. Also, the amount of chelating agent plays an important role on the final morphology of the product. Chelating agent is often an organic compound with long carbon backbone, which helps the formation of a gel-like mixture when the solution is heavily concentrated. Without the chelating agent, the element in the solution cannot be homogeneously mixed at the atomic level, which would lead to impurities or even the wrong compound.

In a routine solution-based technique, the precursor materials are firstly dissolved in solvents (diwater, ethanol, etc.) with a stoichiometric molar ratio. Then, chelating agent (e.g., citric acid) is added, the amount of which is determined by the application of the compound. If the compound is used as the cathode, the molar ratio between carbon in citric acid and lithium ions in a lithium compound can be around 1. If the sample is used as the electrolyte, the ratio described above should be around, or less, than 0.1. Then, the pH value of the solution is adjusted by adding nitric acid or ammonium hydroxide to keep all of the ions in the solution during the following steps of refluxing and gelation. During refluxing at around 100 ^{o}C for a long time, the metal ions in the solution are supposed to bind to the carbon bone of the chelating agent by substituting a proton. After refluxing, the solution was concentrated resulting in a gel network. The atmosphere of this step is essential for keeping the valence state of the compound. Further heating of the gel to around 350 °C results in an exothermic reaction, converting the gel to powders and the residual organic compound is removed by heating at the same temperature. The resulting oxide or phosphate powders are homogenous and porous with very high surface to volume ratio. Further sintering of the powders is described in the next paragraph.

The powders obtained from the solution-based technique is then ground and pressed into pellet form and sintered in tube furnace at high temperatures. The atoms are able to diffuse faster at high temperatures; therefore, the amorphous powders are crystallized and the point contact between powders can change to grain boundaries. Meanwhile, the porosity of the powders is reduced. Therefore, this crystallization step is enough to obtain high quality, single crystal cathode composite, composed of cathode compounds and residual carbon. However, for $Li_7La_3Zr_2O_{12}$ electrolyte ceramics

prepared at temperatures higher than 1000 ^{o}C, the biggest challenge is to maintain the lithium stoichiometry in the material. As suggested by very broad XRD peaks, the as-prepared sol-gel powders (before sintering) were nano-sized, possessing very high surface to volume ratio. Direct heating of those powders to 1230 °C could have resulted in severe lithium evaporation. So to avoid the above problem, we performed sintering in two steps. In the first step, the sol-gel prepared powders were calcined at 800 ^{o}C for 10 hours. This resulted in grain-growth and hence a reduction in the over-all surface to volume ratio. In the second step compressed powders were calcined at 1230 ^{o}C for 8 h. Because of the reduced surface to volume ratio of the powders and the short calcination time, the problem of lithium evaporation was eliminated. The process is illustrated in Figure 2.1.

2.1.2 Pulsed Laser Deposition

In a pulsed laser deposition system, an excimer laser pulse of very high power is generated by discharging KrF gas discharge. The generated laser is then focused on the surface of a solid target and evaporates the material from the target. The energy density delivered by the laser can vary in the range of 1-5 J/cm^2, which is converted to around 1 GW/cm^2 power density during the time length (25 ns) of the laser pulse. This amount of power can increase the localized temperature as much as 25, 000 K [1]. Therefore, high temperature plasma (plum) is generated and expands in the PLD chamber in a forward direction. After that, the plasma condenses on a comparatively cool substrate kept 4.5 cm away from the target. A schematic diagram of a PLD system is shown in Figure 2.2. PLD technique has several advantages, one of which is the stoichiometric material transfer from the target to the substrate, due to the extremely high localized temperature,

which allows equal ablation rates for all elements in the target. The second advantage of the PLD system is the relatively lower substrate temperature required for epitaxial growth. Since the plasma plume is of very high temperature, the plume particulates condensed on the substrate surface possess high kinetic energy; the substrate energy required for epitaxial growth is lower than in other techniques. On the other hand, the high kinetic energy of the condensing plasma can remove some light element from the substrate easily. In our experiment, since lithium is very light and volatile, it might gain energy from the plasma and evaporate from the surface of the substrate, resulting in off-stoichiometric films. Therefore, a compensation target of Li_2O was prepared and used together with the $Li_7La_3Zr_2O_{12}$ target to ensure lithium stoichiometry.

2.2 Characterization

2.2.1 X-ray Diffraction

X-ray diffraction (XRD) was employed to find out the crystal phase, orientation and lattice parameters of the bulk powders, pellets and thin films. The θ-2θ XRD patterns were collected using a Philips XPERT diffractometer with Cu Kα source and Ni filter. According to Bragg's law ($n\lambda=2d\sin\theta$), the crystallographic details of the power and thin film samples can be revealed. The scans were taken in the 2θ range of 10^o to 90^o at room temperature.

2.2.2 Scanning Electron Microscopy and Energy and Dispersive X-ray Spectroscopy

Scanning electron microscopy (SEM) was employed to characterize the surface morphology of the produced sol-gel powders, sintered pellets and deposited thin films. A

Hitachi S3000-N SEM system in our experiment used a low-energy (<50 eV) secondary electron detector to form images. Secondary electrons are generated from out-shell of the specimen atoms by inelastic scattering, giving information about the surface morphology of the specimen. Energy dispersive x-ray spectroscopy (EDS) was used to analyze the elemental and compositional characteristics of thin-film and bulk samples. The Hitachi S3000-N is equipped with an EDX sapphire detector cooled by liquid nitrogen. EDS can detect the element of the specimen, relying on the principle that each element has a unique atomic structure and therefore, unique energy difference between different discrete electron states. When one electron in lower energy state is ejected to an excited state or out of the shell, there is a hole left which is then filled by an electron at higher energy state, during this process an x-ray is emitted and detected by corresponsive detector, forming a set of peaks characteristic of each element. However, EDS can't detect elements with an atomic number smaller than 5.

2.2.3 UV/Visible Transmission Spectroscopy

Optical transmission spectroscopy (OTS) was used to study the absorption intensity and optical band gap of the LLZO films. A UV/Visible spectrometer was used to collect the data in the transmittance mode. A piece of sapphire was used to collect the base-line before taking tests on the films grown on sapphire. The frequency range of the spectrometer is from 190 nm to 1100 nm. If the energy of the photon is larger than the value required to drive one electron from the valence band to the conduction band, it will be absorbed, otherwise it will transport through the thin films. The optical band gaps of the films were calculated first by changing the transmittance to absorption by this equation

$$I \propto e^{-\alpha x} \tag{2.1}$$

where, I is the transmittance, x is the thickness of the films, and α is the absorption coefficient.

2.2.4 Raman Spectroscopy

Raman spectroscopy is used to examine the local structure of a specimen, such as the rotational, vibrational, and other low-frequency modes. In a measurement, a monochromatic light (in the range from near ultraviolet to near infrared) is pointed on the sample. The incident photon interacts with all kinds of low-frequency modes, resulting in a shift of the scattered photon (inelastic scattering). The shift in energy can be up or down, depending on the specific modes in the system. If the energy of the emitted photon is lower than that of the incident light, it is called Stokes shift, where the excited molecule relaxes to a higher energy state than before. On the other hand, if the energy shift is upward, it is called Anti-Stokes shift, where the molecule coming back to a lower energy state than the pre-exited rotational or vibriational state. Notably, the energy of the laser beam should be in a proper range, or the sample would be changed due to absorption of too much thermal energy.

2.2.5 Fourier Transform Infrared Spectroscopy

Fourier transform infrared spectroscopy (FTIR) is often used to obtain an infrared spectrum of absorption, emission, photoconductivity or Raman scattering of the sintered solid (here, only absorption is addressed). Instead of using monochromatic laser, an FTIR spectrometer simultaneously collects spectral signal in a broadband spectral range. The name of Fourier transform infrared spectroscopy comes from the fact that the raw data

(time domain) will be converted into the actual spectrum (frequency domain) by a Fourier transform (a mathematical algorithm).

2.2.6 DC Polarization

DC polarization is used to find out the ratio between ionic and electronic conduction contribution in a mixed conductor. A mixed conductor should be sandwiched between two ionic-blocking electrodes and polarized by a DC voltage; then the current through the sample is recorded versus time until the value of the current stabilizes. At the very beginning, the current value should be high, since both ions and electrons are moving through the sample; while the current will drop very quickly and stabilizes at a lower value when all the ions are polarized to one side of the sample. The resistance difference between the two values is the conduction contribution from the ions. The stabilized resistance is the pure electronic conduction.

2.2.7 Electrochemical Impedance Spectroscopy

Electrochemical impedance spectroscopy (EIS) is a technique used to analyze the complex impedance of an electrochemical cell or other electrical device. At the desired DC voltage (V_{DC}), a small AC voltage changing in a sinusoidal wave-function is added to V_{DC}, forming in an output voltage, the corresponding impedance of the cell is implied by the recorded IV curve. The frequency of the AC signal is changed in a range; therefore, the specific impedance is calculated from each IV curve recorded at each frequency. The recorded data can be plotted in two ways: Bode or Nyquist. Bode curve uses frequency as the x axis, and total impedance is plotted as well as phase between imaginary and real resistance. Nyquist plot converts the total impedance and phase into real and imaginary

resistance and uses them as the x and y axis. The latter is more often seen in research articles, since its shape gives a clear idea about the equivalent circuit mode that might fit to the impedance of the sample.

Equivalent circuit method is used to analyze the inner electrical structure of tested devices. There are four electrical elements used to represent the equivalent circuit: (i) resistance R, which doesn't change with the frequency, the impedance Z = R; (ii) capacitance C, the admittance of which increases obviously with the frequency in certain range, the impedance $Z = -j/\omega C$ ($j=\sqrt{-1}$); (iii) inductance L, which mostly arrive from the connecting wires, $Z = j\omega L$; (iv) constant phase element (CPE) Q, which is a capacitive item, though not a pure capacitor due to surface absorption effect, the impedance of Q is

$$Z_Q = \frac{1}{Y_0} \times (j\omega)^{-n}, 0 < n < 1 \tag{2.2}$$

where Y_o is always a positive value with a dimension of $\Omega^{-1} \cdot cm^{-1} s^{-n}$. When n=0.5, the Q element becomes Warburg impedance [2]. Warburg impedance describes ion diffusion at low frequencies and is characterized as a straight line with a slope of 1 in the Nyquist plot.

The typical equivalent circuit of a lithium-ion battery is shown in Figure 2.3. The meaning of each subscript is explained in the caption. Here I would like to discuss three issues: first, the intercalation capacitance of the cell; second, the formation of solid-electrolyte layer; and third, the factors influencing the value of charge transfer resistance.

Firstly, the intercalation capacitance is built up by lithium accumulation on the surface of the cathode particle before insertion into the crystal structure and combination with an electron in the framework. The value of the intercalation capacity (C_{int}) is

proportional to I/v in cyclic voltammogram (CV). Also, the intercalation capacitance is conveniently represented in a dimensionless form:

$$C_{int} = [g + \frac{1}{x} + \frac{1}{1-x}]^{-1} \quad (2.3)$$

where, x is the intercalation level, and g reflects the interaction between the intercalation sites [3]. The equation shows that the capacitance should be very small for x approaching 0 or 1. At the beginning of charging process (x→1), the current is quite small in cyclic voltammogram; therefore, the value of I/v is small, which is consistent with the small value of C_{int}. Similarly, the CV current decreases at the end of the charging process, when x→0. Secondly, the solid-electrolyte interlayer (SEI) formed during cycling needs to be better revealed, since it affects the inner resistances of the batteries. A typical SEI layer is about 30-50 nm thick and it is constituted of two sub-layers: the inorganic layer adjacent to the cathode side and the organic layer close to the electrolyte [4]. The inorganic layer includes compounds of Li_2O, Li_2CO_3, and LiF, etc.; and the outer layer is mostly Li-R (R is poly-radical from the electrolyte solvent). They are formed due to the reaction between the cathode and electrolyte. The thickness of the layer is determined by several factors: the stability between the cathode and electrolyte, the surface area of the cathode powders, the state of lithium desertion, the cycling rates, etc. Thirdly, the charge transfer resistance is inversely proportional to the equilibrium exchange current density (I_0) [5]. I_0 interprets the rate constant of charge transfer at zero overpotential. Therefore, factors that reduce charge transfer resistance will increase the equilibrium exchange current, e.g., operating temperature, electron transfer between cathode crystal and carbon coating, electron conduction through carbon, ion conduction within the cathode particle, etc.

2.2.8 Cyclic Voltammetry

Cyclic voltammetry (CV) is a technique used to study the electrochemical properties of an analyte in an electrochemical cell. In a cyclic voltammetry test, the working electrode potential versus the reference electrode is ramped linearly versus time, which ends and is inverted when it reaches a set potential. The ramping rate has the dimension of V/s. The current flow into and out of the working electrode is plotted as the y-axis and the applied voltage in x-axis to give the cyclic voltammogram curve. Current flowing into the working electrode is positive, and vise versa. During the forward scan (V↑), a current peak is produced for any cathode that can be reduced as the voltage reaches the reduction potential; the peak then falls off as the concentration of lithium is depleted. During the backward scan, an anodic peak is produced when the cathode is reoxidized. The shape of this oxidation peak will usually be similar to that of the previous reduction peak. Moreover, the current peak will be proportional to the square root of the scan rate, if the reaction is limited by diffusion of lithium ions to the electrode surface. As a result, information is obtained about the redox potential and electrochemical reaction rates of the compounds within the diffusion layer.

2.3 References

1. Singh, R.; Narayan, *J. Phys. Rev. B* **1990**, 41, 8843.

2. Zhai, N. S.; Li, M. W.; Wang, W. L.; Zhang, D. L.; Xu, D. G. *J. Phys. Conf. Ser.* **2006**, 48, 1157.

3. Chidsey, C. E. D.; Murray, R. W. *J. Phys. Chem.* **1986**, 90, 1479.

4. Balbuena, P. B.; Wang, Y. Lithium-ion batteries: solid-electrolyte interphase; Imperial College Press: London, 2004.

5. Monk, P. Fundamentals of electroanalytical chemistry; John Wiley & Sons Ltd: West Sussex, 2001.

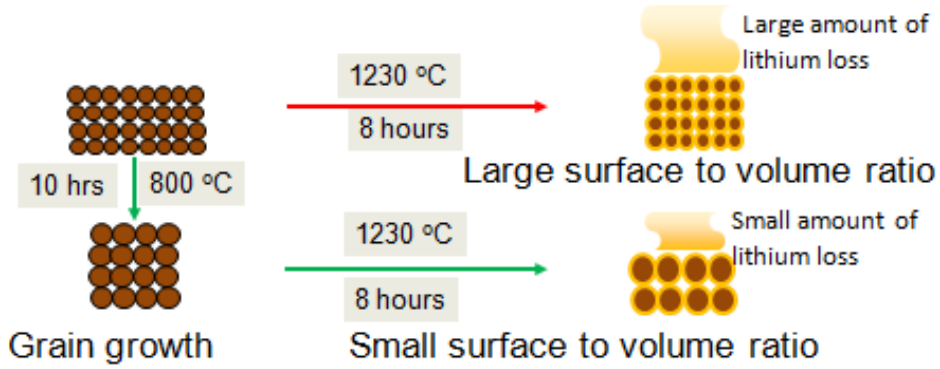

Figure 2.1. Illustration of two kinds of sintering process.

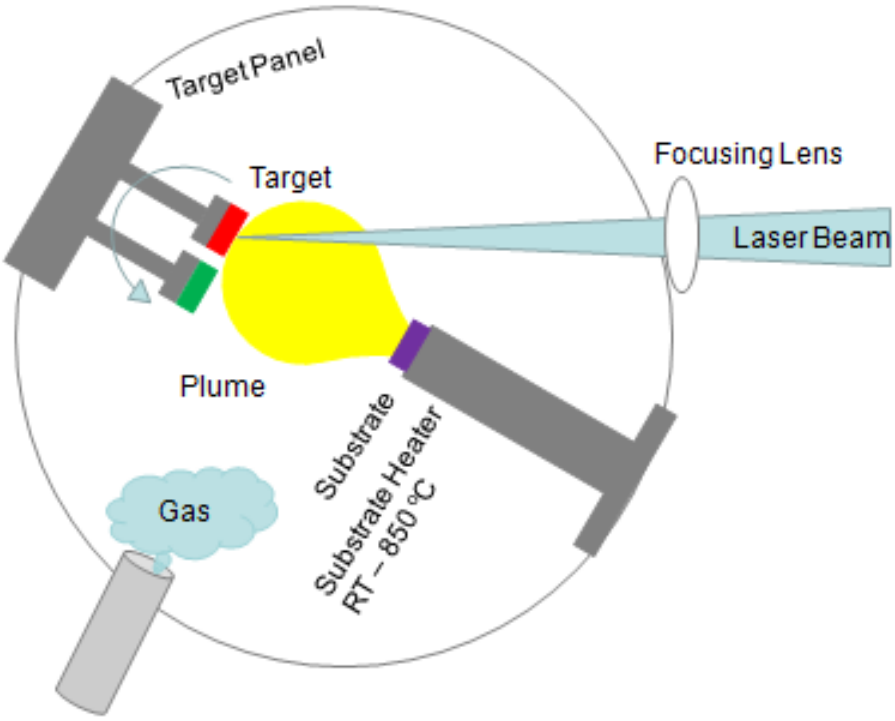

Figure 2.2. Schematic drawing of pulsed laser deposition system.

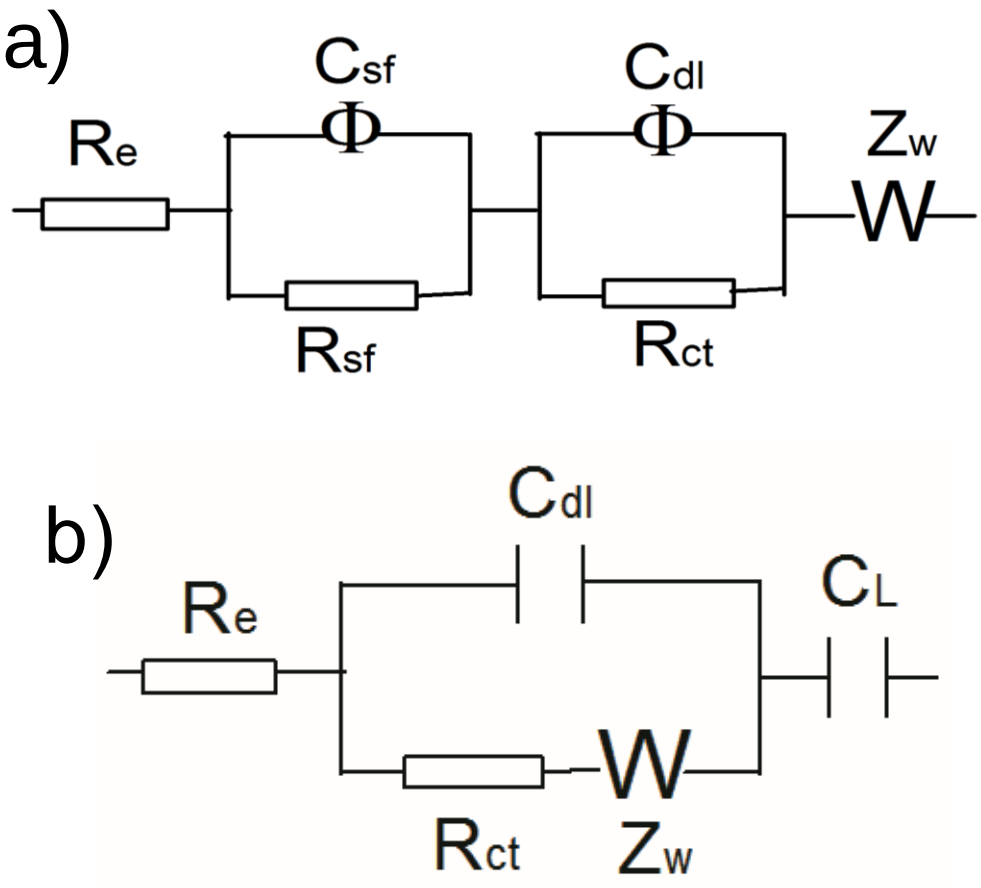

Figure 2.3. Equivalent circuits of the (a) activated LIB and (b) as-assembled LIB. R_e is the electrolyte resistance, dl is the double layer, ct is charge transfer, sf represents the interface between electrolyte and electrode, W is Warburg, and L is the intercalation.

CHAPTER 3

MODIFICATION OF $LiFePO_4$/C NANOCOMPOSITE CATHODE

3.1 Abstract

Here we report the synthesis of $LiFePO_4$/C nanocomposite cathode materials for lithium-ion batteries using a novel solution-based technique. Our technique is a modified version of traditional sol-gel technique and utilizes chelating agents which simultaneously create a coating of carbon on the $LiFePO_4$ nanoparticles. Two different chelating agents namely, poly vinyl alcohol (PVA) and citric acid were investigated. Different amounts of chelating agent were used in the starting solution to give different ratios of $LiFePO_4$ to carbon in the final product. Materials thus synthesized were thoroughly characterized using X-ray diffraction (XRD), scanning electron microscopy (SEM), energy dispersive X-ray spectroscopy (EDS), Fourier transform infrared spectrometer (FTIR), Raman spectroscopy, and electrochemical measurements. We find that chelating agents with short carbon chains (such as citric acid) perform better than agents with long carbon chains (such as PVA), and the carbon/lithium atomic ratios in the starting solution are optimized to be between 4:2 and 6:2.

Reprinted with permission of Effects of carbon precursors on $LiFePO_4$/C nanocomposites for lithium-ion batteries, Nanoscience and Nanotechnology Letters 3, 487-490, 2011.

3.2 Introduction

$LiFePO_4$ is one of the most widely used cathode materials for making lithium-ion batteries, due to its high theoretical capacity of ~170 mAh/g, a flat discharge voltage at 3.4 V [versus Li^+/Li], low cost and less impact on the environment [1-3]. However, $LiFePO_4$ has an intrinsic drawback of poor electrical conductivity due to tetrahedral PO_4 induced localization of d-electron band, which adversely affects its electrochemical performance [4-5]. To overcome this barrier, various approaches have been applied, such as compositing of $LiFePO_4$/C, addition of metal dispersion, doping with aliovalent cations, etc. [6-10] Among all the above approaches, making a composite of $LiFePO_4$ with carbon is the best, since the rate capability is significantly increased and the cost is lower than other means. [11]

There are two main routes to prepare $LiFePO_4$, solid state method and the solution based methods. Solid state method requires the mechanical milling of the ingredient materials for a long time followed by successive annealing at high temperatures. This is a time consuming process and usually results in larger particles and a higher level of impurities. Compared to this, sol-gel technique is a fast and economical method which enables the synthesis of particles with excellent morphology and uniform particle size, while offering a high phase purity and homogeneity [12-17]. Moreover, sol-gel technique is also a convenient method to do carbon coating on $LiFePO_4$ particles by in situ carbonization of organic precursors [18]. By greatly increasing the surface conductivity of $LiFePO_4$ particles, carbon coating serves as an important way to improve the rate performance, specific capacity and cyclability of $LiFePO_4$. Also, the residual carbon from the in situ carbonization of organic precursors can inhibit the growth of the particle size

during sintering while helping maintain reductive atmosphere [19].

The extent of the above benefits are dependent on many factors: the type and amount of organic precursors, the heat-treatment temperatures, etc. [11, 20] Various kinds of organic compounds have been used, functioning as both the reductive agent and carbon source at the same time, e.g., citric acid [20], polyvinyl alcohol (PVA) [21], lauric acid [22], ascorbic acid [23], sucrose [24], polyethylene glycol (PEG) [12], etc. These compounds can be broadly divided in two classes: long carbon chain compounds and short carbon chain compounds. The aim of this paper is to find which class of compounds produces better material. To achieve this goal we have chosen two representative materials, citric acid, a low carbon chain material and PVA, a long carbon chain material. We have also tried to find the optimum ratio of Li:C (in the starting solution) needed to achieve the highest possible capacity.

3.3 Experimental Procedure

$LiFePO_4$/C nanocomposites were synthesized by dissolving stoichiometric $LiOH \cdot H_2O$, $Fe(NO_3)_3 \cdot 9H_2O$ and P_2O_5 in distilled water and mixed with different amounts of citric acid according to different carbon/lithium ratios. The pH value of the resulting solution was adjusted to 7 by adding ammonium hydroxide. Then, the sol was refluxed for 12 hours and dried in air, creating a metal organic gel. Differential Scanning Calorimeter (DSC) measurements were performed on a cap of gel between 50 and 300 ^oC at a scanning rate of 10 ^oC/min. The DSC curve showed a strong peak at the temperature of 236.67 ^oC, where the pyrolysis of citric acid occurred. After that, the gel was heated to 300 °C in air resulting in $LiFePO_4$/C precursor powders which were pressed into a pellet and annealed under nitrogen atmosphere at 650 ^oC for 12 hours. The advantage of our

technique was the elimination of nitrogen atmosphere until the last crystallization step at 650 °C; this elimination reduces the use of nitrogen (costless) and simplified the experiment. In addition, the pyrolysis of organic compound in air was easier and less carbon resided in the solid by forming carbon dioxide, increasing the density of functional $LiFePO_4$ materials.

The crystal structure of the products was characterized by θ-2θ x-ray diffraction (XRD); the morphology and chemical composition was investigated by scanning electron microscopy (SEM) and attached energy dispersive x-ray spectroscopy (EDS). The local structure was examined by Fourier transform infrared spectroscopy (FTIR) and Raman spectroscopy; and the ionic and electric conductivities were tested by DC.

Electrochemical performance of the most promising samples was investigated by assembling lithium-ion cells using lithium as anode, Celgard 2400 as separator and 1 M/L $LiPF_6$/EC-DEC (1:1 vol %) as the electrolyte in reusable splitting cells. The cathode was fabricated by mixing $LiFePO_4$ composites with polyvinylidiene fluoride (PVDF) binder (Kynar®) and carbon black in a weight ratio of 85:5:10. The charge/discharge performance of the cells, all assembled in an argon-filled glove box, were evaluated at different temperatures.

3.4 Results and Discussion

Figure 3.1 shows the θ-2θ XRD patterns of the $LiFePO_4$ powders using different carbon sources and carbon/lithium ratios. The XRD patterns reflect the typical orthorhombic structure of $LiFePO_4$ olivine, indicating a highly pure phase. The lattice parameters for C4/2 were obtained to be a=6.010 Å, b=10.331 Å and c=4.698 Å by Rietveld refinement (JCPDS 40-1499, *Pnmb*(62), a = 6.019 Å, b = 10.347 Å,

c = 4.704 Å).

Figure 3.2 shows the grain size of each sample, calculated by Scherrer formula based on the full width at half maxima (FWHM) of their most intense peaks. The 4:2 and 6:2 carbon/lithium ratio using citric acid gave the smallest average grain size: both carbon lacking C3/2 and carbon rich C8/2 showed bigger sizes, which indicates that carbon will inhibit the grain growth by forming a thin layer covering $LiFePO_4$ grains, but too much carbon may form carbon agglomerates and no longer be uniformly distributed between grains. This figure also shows that the C4/2 has smaller grain size than P4/2, which may be caused by the long carbon chains of PVA leading to local carbon agglomerates. Therefore, we expected that C4/2 and C6/2 of the smallest average grain size would show the best electrochemical behavior due to shorter diffusion length and higher surface area.

The SEM micrographs of the C4/2 $LiFePO_4$/C powders before and after annealing are displayed in Figure 3.3. Before annealing, the $LiFePO_4$/C composites were a uniform porous gel due to violent exothermic reaction; after annealing, it crystallized into nanosized particles with an average size of about 30 nm, close to the crystallite size calculated from XRD peak broadening. The composition of this sample examined by EDS is shown in Figure 3.4; only the peaks corresponding to oxygen, phosphorous, iron and carbon are present in this spectrum, the composite was very pure compared to some results in the literature obtained by ball milling.

Figure 3.5 shows the FTIR spectra of C4/2 composites, which is consistent with previous reports of $LiFePO_4$ [25-26]. The absorption of FTIR spectra are ascribed to the intramolecular vibrations of $(PO4)^{3-}$—the P-O stretching modes belong to the 937-1138

cm^{-1} range; and O–P–O bending modes are in the range from 465 to 643 cm^{-1}. The gap between 700 and 900 cm^{-1} provides a proof for absence of impure phases like phosphate anions involving $(P_2O_7)^{4-}$, $(P_3O_7)^{5-}$, etc. The embedded figure is the Raman spectroscopy which shows peaks for $LiFePO_4$ at 995 and 1053 cm^{-1}. The deviation of 1053 cm^{-1} peak from the reported 1064 cm^{-1} could be attributed to the oxidation of iron (II) by the high power of the testing laser.

Figure 3.6 shows the direct current conductivity versus time for C3/2, C4/2 and C6/2. Both C3/2 and C4/2 curves had a typical mixed ionic and electronic conducting performance. The electronic and ionic conductivity for C3/2 was around 10^{-8} S/cm and 10^{-12} S/cm, while the conductivities for C4/2 increased to 10^{-5} S/cm and 10^{-6} S/cm, respectively. The DC profile for C6/2 showed pure electronic conductivity around 10^{-2} S/cm, ascribed to abundant carbon in the composites. The increase of the conductivity with time may be caused by the current output device. Although C6/2 may have better rate capability due to higher electric conductivity provided by rich carbon coverage, the specific capacity of C6/2, may be less than that of C4/2 because of its lower density of effective $LiFePO_4$ material. Hence, it is hard to tell whether C4/2 or C6/2 would exhibit better electrochemical performance.

In order to test the specific capacity of the two promising samples, the C4/2 and C6/2 $LiFePO_4$/C composites were made into cathode and cycled between 4.2 V and 2.5 V at 20 °C and 30 °C. Figure 3.7 shows that the specific capacity of C4/2 (136 mAh/g) was higher than that of C6/2 (130 mAh/g) at 0.1 C rate at 20 °C, while the voltage derivation from 3.4 V was slightly larger than that of C6/2 due to kinetic limit induced polarization. When going up to 30°C, the specific capacities of C4/2 and C6/2 were increased to 148

mAh/g and 140 mAh/g, respectively. This improvement of performance at higher temperature was mainly due to faster ionic diffusion within electrolyte and electrode materials. Therefore, at lower temperature, C6/2 sample is better due to faster kinetics, whereas, at slightly elevated temperature, C4/2 is better due to higher density of effective material.

3.5 Summary

A simple, novel and low-cost sol-gel technique has been successfully employed to synthesize high purity nannosized $LiFePO_4$/C composite. It was found that the citric acid performs better than PVA which we believe is due to its short carbon chains resulting in homogeneous carbon distribution. The grain size and the homogeneity of composites were also found to be influenced by the carbon/lithium ratio in the starting solution. By controlling the citric acid weight, we found the optimum ratio of the carbon/lithium in the initial solution lies between 4/2 and 6/2 which results in a thin layer of carbon uniformly covering the $LiFePO_4$ grains.

3.6 References

1. D. D. MacNeil, Z. Lu, Z. Chen and J. R. Dahn, *Journal of Power Sources* 108, 8 **(2002)**.

2. A. Ritchie and W. Howard, *Journal of Power Sources* 162, 809 **(2006)**.

3. F. Sauvage, E. Baudrin, L. Gengembre and J. M. Tarascon, *Solid State Ionics* 176, 1869 **(2005)**.

4. J.-K. Kim, J.-W. Choi, G. S. Chauhan, J.-H. Ahn, G.-C. Hwang, J.-B. Choi and H.-J. Ahn, *Electrochimica Acta* 53, 8258 **(2008)**.

5. K.-F. Hsu, S.-Y. Tsay and B.-J. Hwang, *Journal of Power Sources* 146, 529 **(2005)**.

6. S.-Y. Chung, J. T. Bloking and Y.-M. Chiang, *Nat Mater* 1, 123 **(2002)**.

7. S. Yang, P. Y. Zavalij and M. S. Whittingham, *Electrochemistry Communications* 3, 505 **(2001)**.

8. M. Takahashi, S. Tobishima, K. Takei and Y. Sakurai, *Journal of Power Sources* 97-98, 508 **(2001)**.

9. N. Ravet, Y. Chouinard, J. F. Magnan, S. Besner, M. Gauthier and M. Armand, *Journal of Power Sources* 97-98, 503 **(2001)**.

10. H. Huang, S. C. Yin and L. F. Nazar, *Electrochemical and Solid-State Letters* 4, A170 **(2001)**.

11. Z. Xu, L. Xu, Q. Lai and X. Ji, *Materials Research Bulletin* 42, 883 **(2007)**.

12. W-J Zhang, *Journal of Power Sources* 196, 2962 **(2010)**.

13. D. Choi and P. N. Kumta, *Journal of Power Sources* 163, 1064 **(2007)**.

14. D. Jugovic and D. Uskokovic, *Journal of Power Sources* 190, 538 **(2009)**.

15. Y. Lin, H. Pan, M. Gao and Y. Liu, *Journal of The Electrochemical Society* 154, A1124 **(2007)**.

16. K.-F. Hsu, S.-Y. Tsay and B.-J. Hwang, *Journal of Materials Chemistry* 14, 2690 **(2004)**.

17. M. Koltypin, D. Aurbach, L. Nazar and B. Ellis, *Journal of Power Sources* 174, 1241 **(2007)**.

18. M. Gaberscek, R. Dominko, M. Bele, M. Remskar, D. Hanzel and J. Jamnik, *Solid State Ionics* 177, 1801 **(2005)**.

19. Y. Lin, M.X. Gao, D. Zhu, Y.F. Liu and H.G. Pan, *Journal of Power Sources* 184, 444 **(2008)**.

20. S. Beninati, L. Damen and M. Mastragostino, *Journal of Power Sources* 194, 1094 **(2009)**.

21. A. Subramania, N. Angayarkanni and T. Vasudevan, *Materials Chemistry and Physics* 17, 19 **(2007)**.

22. D. Choi and P. N. Kumta, *Journal of Power Sources* 174, 1064 **(2007)**.

23. F. Croce, A.D. Epifanio, J. Hassoun, A. Deptula, T. Olczac and B. Scrosati, *Electrochemical and Solid-State Letters* 5, A47 **(2002)**.

24. J-K. Kim, J-W. Choi, G. S. Chauhan, J-H. Ahn, G-C. Hwang, J-B. Choi and H-J. Ahn, *Electrochimica Acta* 53, 8258 **(2008)**.

25. P.-X. Zhang, X.-Y. Li, Z.-K. Luo, X.-Q. Huang, J.-H. Liu, Q.-M. Xu, X.-Z. Ren and X. Liang, *Journal of Alloys and Compounds* 467, 390 **(2009)**.

26. K. Zaghib, A. Mauger, F. Gendron and C. M. Julien, *Chem. Mater.* 20, 462 **(2008)**.

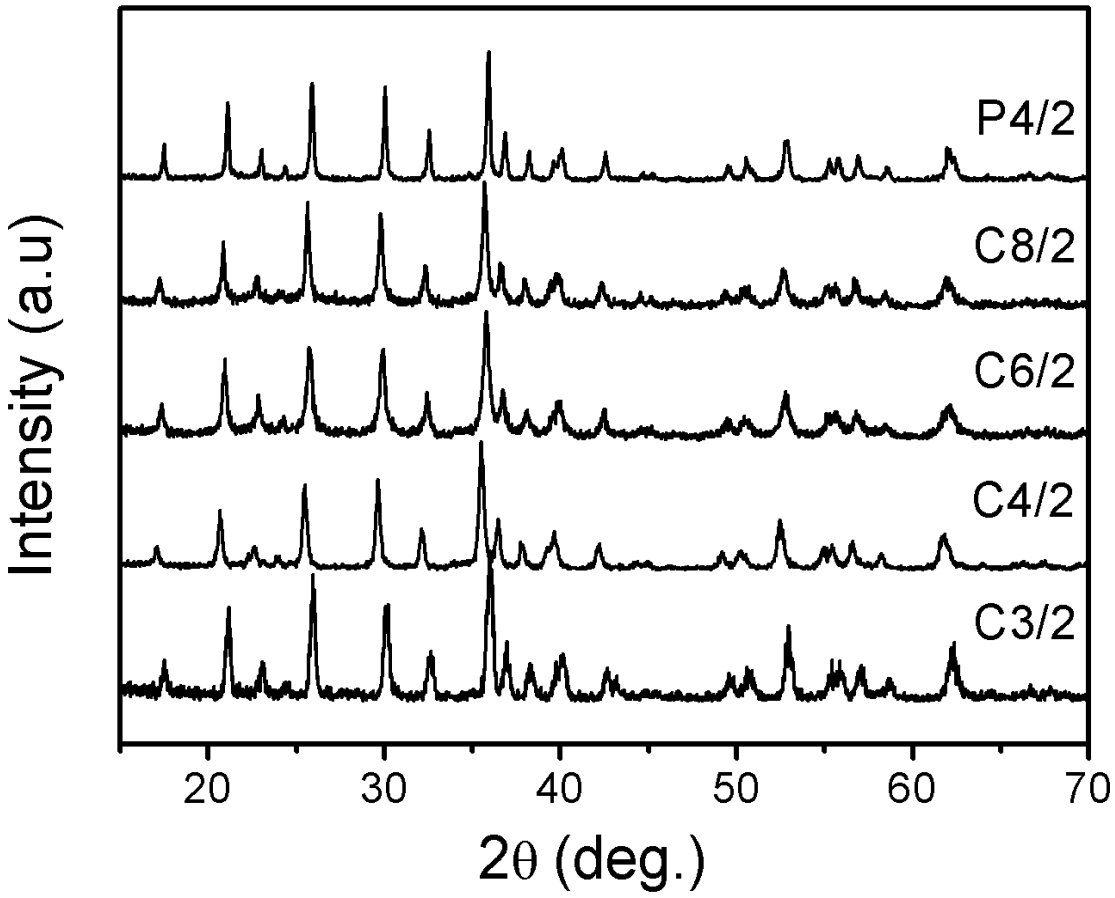

Figure 3.1. X-ray diffraction patterns of C3/2, C4/2, C6/2, C8/2 and P4/2 $LiFePO_4$/C composites (C3/2: the carbon source is citric acid and n_{Carbon}/n_{Li} = 3:2; P4/2: the carbon source is PVA and n_{Carbon}/n_{Li} =4:2).

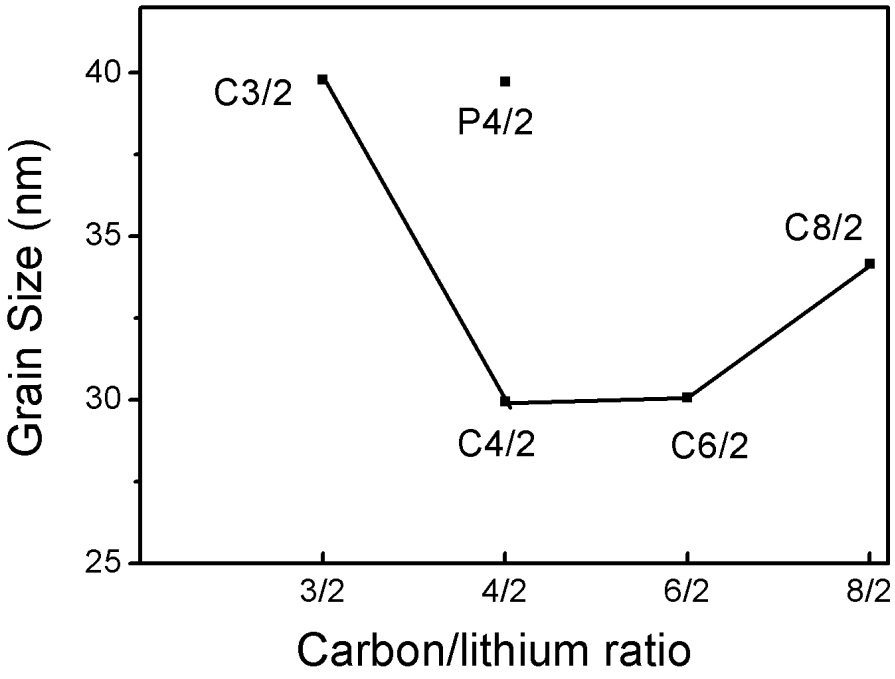

Figure 3.2. Average grain sizes for C1/2, C4/2, C6/2, C8/2 and P4/2 $LiFePO_4$.

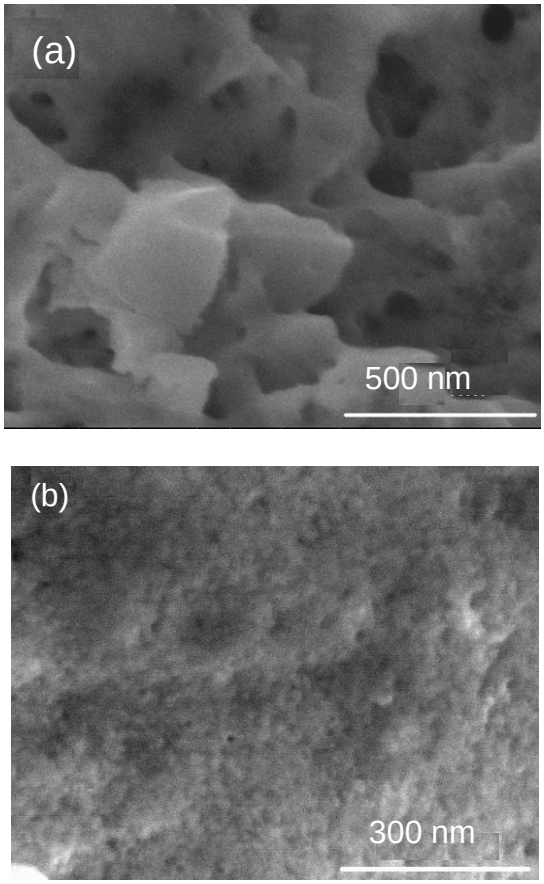

Figure 3.3. SEM micrographs of C4/2 powders (a) before and (b) after annealing.

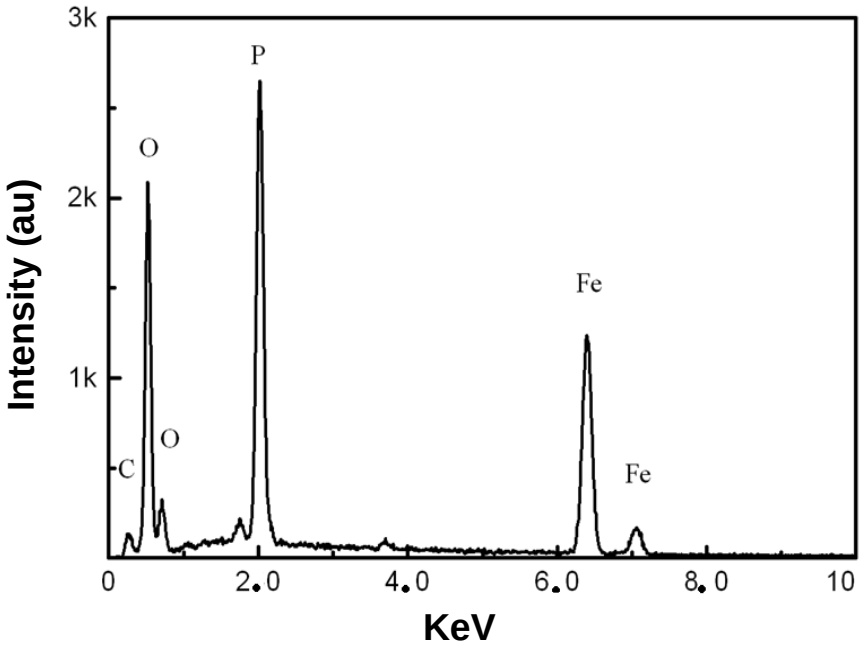

Figure 3.4. EDS spectrum of C4/2 pellet.

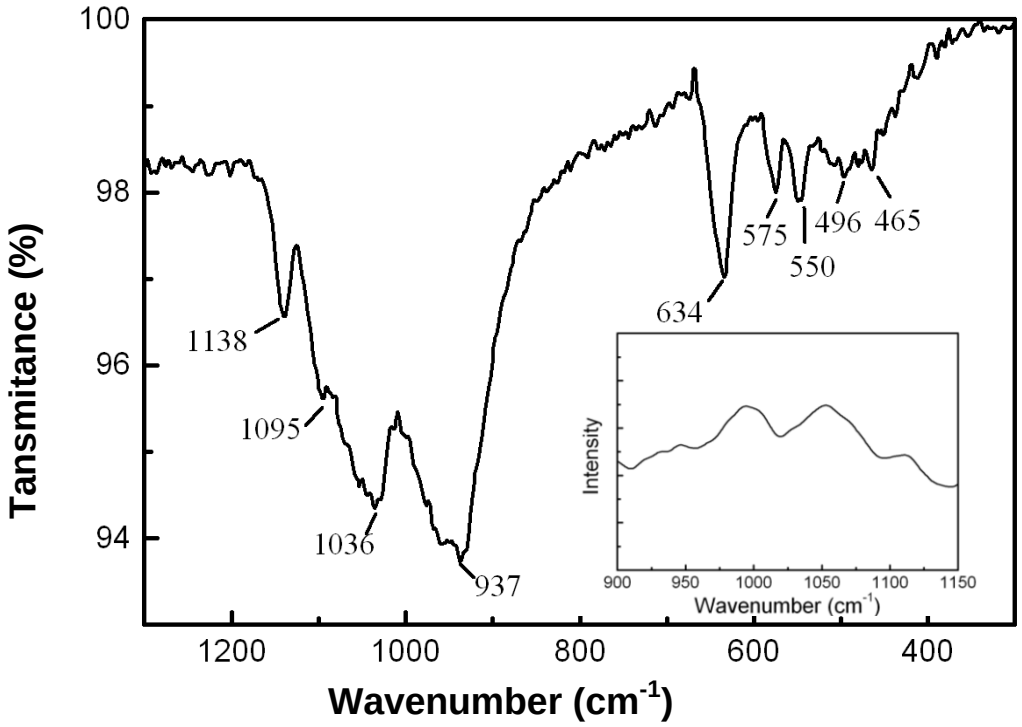

Figure 3.5. FTIR pattern and Raman spectra of $LiFePO_4$/C pellet.

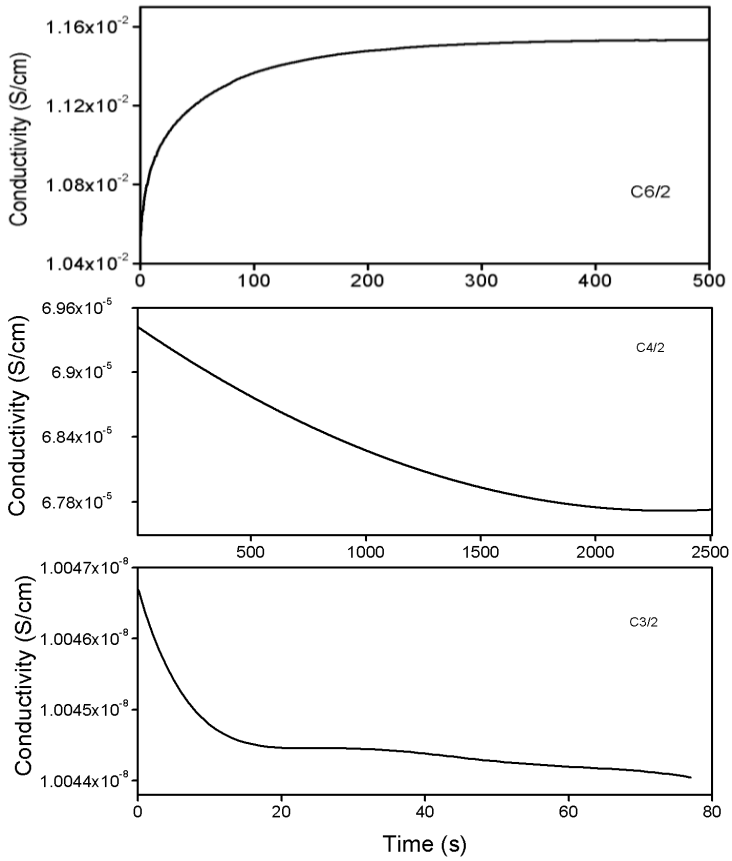

Figure 3.6. DC conductivity measurements for C3/2 (bottom), C4/2 (mid) and C6/2 (up).

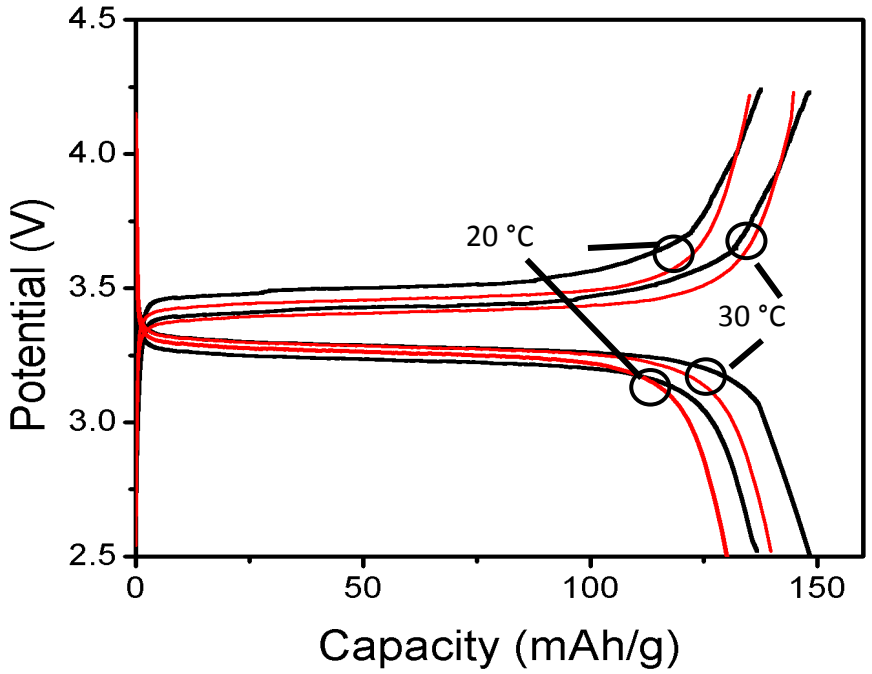

Figure 3.7. Charge/discharge performance of C4/2 (black) and C6/2 (red) $LiFePO_4$/Li cell at different temperatures.

CHAPTER 4

MODIFICATION of $Li_2FeP_2O_7$/C NANOCOMPOSITE CATHODE

4.1 Abstract

$Li_2FeP_2O_7$ is a newly developed polyanionic cathode material for high performance lithium-ion batteries. It is considered very attractive due to its large specific capacity, good thermal and chemical stability, and environmental benignity. However, the application of $Li_2FeP_2O_7$ is limited by its low ionic and electronic conductivities. To overcome the above problem, a solution-based technique was successfully developed to synthesize $Li_2FeP_2O_7$ powders with very fine and uniform particle size (< 1 μm), achieving much faster kinetics. The obtained $Li_2FeP_2O_7$ powders were tested in lithium-ion batteries by measurements of cyclic voltammetry, electrochemical impedance spectroscopy and galvanostatic charge/discharge cycling. We found that the modified $Li_2FeP_2O_7$ cathode could maintain a relatively high capacity even at fast discharge rates.

4.2 Introduction

Lithium-ion batteries (LIBs) are widely used as power sources in portable computers, entertainment devices, telecommunications, and recently in electrical

Jiajia Tan and Ashutosh Tiwari (2012). Modification of High Potential, High Capacity $Li_2FeP_2O_7$ Cathode Material for Lithium Ion Batteries. MRS Proceedings, 1440 , mrss12-1440-o09-133 doi:10.1557/opl.2012.1282 Reprint with permission.

automobiles. As required by EV (electrical vehicles) and HEV (hybrid electrical vehicles), LIBs should be able to store and release large amount of energy in a short time period, while being of light-weight. Therefore, large-scale production of novel cathode materials, with high voltage and large specific capacity, are urgently demanded. Currently available cathode materials such as $LiCoO_2$ [1] and $LiFePO_4$ [2] couldn't fulfill these requirements very well, mostly limited by high price and relatively low specific capacity.

A lot of research has been conducted on polyanionic cathode materials. One way of increasing specific capacity is to increase the redox potential of the polyanionic $LiMXO_4$ (M: transition metal; X = P, As, Si, Ge) [3-6]. Though there has been a large amount of work done on this topic, the overall performance of these materials is not significantly greater than that of more traditional cathode materials. Another way of achieving high specific capacity is to increase the number of removable lithium atoms in one formula. For this purpose, extensive studies have been focused on $Li_xM'_2(YO_4)_3$ ($x > 1$, M': transition metal; Y: S, P, Mo), leading to the development of $Li_2FeP_2O_7$ [7]. Although $Li_2FeP_2O_7$ (LFPO) has low electronic and ionic conductivity, it has a theoretical capacity of 220 mAh/g with both lithium atoms extracted, even higher than that of $Li_3V_2(PO_4)_3$ which can remove three lithium atoms [8-10]. Therefore, it is desirable to synthesize LFPO with improved kinetic properties.

In this paper, we are reporting the modification of LFPO synthesized through a solution-based technique. The effect of synthesis parameters on the crystal structure, morphology and electrochemical performance of the LFPO powders was thoroughly studied.

4.3 Experimental Procedure

Stoichiometric amount of precursor materials were first dissolved in deionized water and mixed together; then ammonium hydroxide was added in, and a transparent solution was achieved at the pH value of 4. The solution was then transferred into a flask and refluxed overnight. After that, the solution was evaporated on a hot-plate and concentrated into a gel, which was then dried at 90 °C in a vacuum. Following that, the sample was placed in a tube furnace and heated at 350 °C for 5 hours under a nitrogen atmosphere, resulting in powders that were then ground and pressed into pellets. At last, the pellets were annealed at different temperatures (500, 550 and 600 °C) for 24 hours in nitrogen. The precursor materials used in the experiment were $LiOH{\cdot}H_2O$, P_2O_5, $Fe(NO_3)_3{\cdot}9H_2O$ and $C_6H_8O_7$ (citric acid). The $LiOH{\cdot}H_2O$ to $C_6H_8O_7$ molar ratio was initially set to be 1: 1.

The obtained samples were characterized on a Philips PW 3040 X-ray diffractometer (Cu Kα radiation, $\lambda = 1.5406$ Å) at the 2θ range of 10° - 90° with a step size of 0.015° and a step time of 0.6 seconds. The scanning electron microscopy (SEM) images were taken at an operating voltage of 20 kV and a working distance of ~15 mm.

The LFPO samples were made into a cathode and tested in lithium-ion batteries. The cathode was fabricated firstly by forming a slurry, which was a mixture of LFPO with PVDF binder (polyvinylidiene fluoride) and carbon black at a weight ratio of 85: 5: 10 in an NMP solvent (N-methyl-2-pyrrolidone). The slurry was then tape-casted on an aluminum foil and baked overnight in a vacuum, with a mass loading of around 10 mg/cm^2. The batteries were assembled in an argon filled glove box, using lithium metal as the anode, Celgard 2400 as the separator, and 1 M $LiPF_6$/EC-DEC (1:1 vol %) as the

electrolyte. The charge/discharge cycling of the cells was tested between 2 V and 4.5 V at different rates from C/20 to 5C. The electrochemical impedance spectroscopy (EIS) was measured in a frequency range of 1 MHz to 0.4 Hz. The cyclic voltamegram (CV) of the cells was scanned from 2 V to 5 V at a rate of 0.05 mV/s.

4.4 Results and Discussion

Figure 4.1 shows the XRD patterns of the samples annealed at different temperatures (500 ℃ , 550 °C and 600 °C). At 500 °C, the sample is likely monoclinic with very broad peaks. When heated at 550 ^{o}C, the powders show a typical XRD pattern for monoclinic LFPO crystals, which belong to the $P2_1/C$ space group. Plus, the peaks are sharp, indicating good crystallinity. When annealed at 600 °C, several extra peaks were observed for impure phases which might be $LiFeP_2O_7$, etc. Based on these results, we can tell that the annealing temperature has a great effect on the crystalline structures of the samples, and the best value found in our experiment is 550 ^{o}C. The lattice constants of the monoclinic LFPO crystals were calculated to be a = 11.0196 Å, b = 9.7497Å, and c = 9.8058 Å, β = 101.5011 °, which were consistent with the literature [7].

The LFPO powders annealed at 550 ^{o}C had a large particle size of ~2 μm (sample 1), as shown in Figure 4.2a. Further reduction of the particle size is needed in order to enhance the kinetic properties of the LFPO powders. As we know, citric acid acts as the chelating agent in the sol-gel process and produces reductive atmosphere during gel-to-powder transformation. Moreover, the residual carbon can restrain grain growth and particle agglomeration during sintering by distributing uniformly between grains [11]. For this, the proper amount of citric acid was added to the starting solution, obtaining a $LiOH{\cdot}H_2O$ to $C_6H_8O_7$ Molar ratio of 1:1.5 (M_{Li}: M_{C6} = 1:1.5). The SEM image of the

newly obtained LFPO powders (sample 2) is shown in Figure 4.2b, where we can see the particle sizes become very uniform and most of them are smaller than 1 μm.

Figure 4.3a shows the electrochemical impedance spectroscopy (EIS) of the lithium-ion batteries as-assembled using sample 1 and sample 2 as the cathode, respectively. The curves can be fitted into the equivalent circuit drawn in the figure: R_e (C_{dL} // ($R_{ct}Z_w$)) C_L (e: electrolyte; ct: charge transfer; w: Warburg diffusion; dL: double layer; L: intercalation capacity) [12]. The charge transfer resistance was largely reduced for the smaller size LFPO particles, due to larger surface areas. Figure 4.3b shows the EIS results of the cells after the first charge process. The curves can be fitted by an equivalent circuit model (inserted diagram): Re (C_{sf}//R_{sf})(C_{dl}//R_{ct})Z_w (sf: surface layer). Still, the finer size LFPO cathode displayed smaller inner resistances in the charged cells. Batteries of small inner resistances are expected to exhibit higher capacity, faster charge/discharge rates, and smaller potential polarization.

The cyclic voltammetry of the cells was measured, and the results are shown in Figure 4.4. The cells exhibit a strong anodic peak around 3.5 V and a consequent cathodic peak at 3.2 V. The rising part around 5 V was assigned to the Fe^{3+}/Fe^{4+} oxidation at 5.2 V, as predicted by Whittingham's group [13]. A small anodic peak at 4.5 V was observed, which may be caused by the removal of lithium atoms from a type of location that requires more energy (higher voltage) for the ionization of one lithium atom. Further research on the structure of LFPO is needed to answer this question. Comparing the peak height of the two kinds of cells, the one with sample 2 as the cathode would display deeper reaction and higher capacity during charge/discharge process.

The charge/discharge behavior of these two kinds of cells is presented in Figure 4.5 (a) and (b), respectively. As expected, the cell with the modified cathode has a larger specific capacity of 106 mAh/g at the rate of 0.05 C, much higher than 82 mAh/g of the other cell. Moreover, the specific capacity of the modified LFPO cathode was larger for all rates in the range from 0.05 C up to 5 C, due to faster transport kinetics through the submicron LFPO powders.

4.5 Summary

We have successfully synthesized and modified the novel LFPO cathode material using a solution-based technique. LFPO powders annealed at 550 °C possessed a pure monoclinic phase. Two kinds of LFPO powders were synthesized with different particle sizes. The smaller particles resulted in reduced inner resistance and enhanced specific capacity of 106 mAh/g tested from lithium-ion cells. Moreover, the cyclic voltammetry test proved that the second lithium of LFPO was active and removable; therefore, higher capacity is attainable for LFPO when coupled with an electrolyte of the proper voltage window.

4.6 References

1. Q. Cao, H.P. Zhang, G.J. Wang, Q. Xiao, Y.P. Wu and H.Q. Wu, Electrochem. Commun. **9** (5), 1228 (2007).

2. Y. Wang, Y. G. Wang, E. Hosono, K. Wang and H. Zhou, Angew. Chem. Int. Ed. **47**, 7461 (2008).

3. K. Amine, H. Yasuda and M. Yamachi, Electrochem. Solid-State Lett. **3**, 178 (2000).

4. H. Guo, K. Xiang, X. Cao, X. Li, Z. Wang and L. Li, Trans. Nonferrous Met. Soc. China **19**, 166 (2009).

5. M. Minakshi, P. Singh, D. Appadoo and D. Martin, Electrochim. Acta **56**, 4356 (2011).

6. M.E. Dompablo, M. Armand, J.M. Tarascon and U. Amador, Electrochem. Commun. **8,** 1292 (2006).

7. S. Nishimura, M. Nakamura, R. Natsui and A. Yamada, J. Am. Chem. Soc. **132**, 13596 (2010).

8. M.M. Ren, Z. Zhou, X.P. Gao, W.X. Peng and J.P. Wei, J. Phys. Chem. C **112**, 5689 (2008).

9. X.H. Rui and C.H. Chen, Electrochimi. Acta, **54**, 3374 (2009).

10. X.H. Rui, Y. Jin, X.Y. Feng, L.C. Zhang and C.H. Chen, J. Power Sources **196**, 2109 (2011).

11. J. Tan and A. Tiwari, Nanosci. Nanotechnol. Lett. **3**, 487 (2011).

12. J. Zhao, L. Wang, X. He, C. Wan and C. Jiang, Int. J. Electrochem. Sci. **5**, 478 (2010).

13. H. Zhou, S. Upreti, N. A. Chernova, G. Hautier, G. Ceder and M. S. Whittingham, Chem. Mater. **23**, 293 (2011).

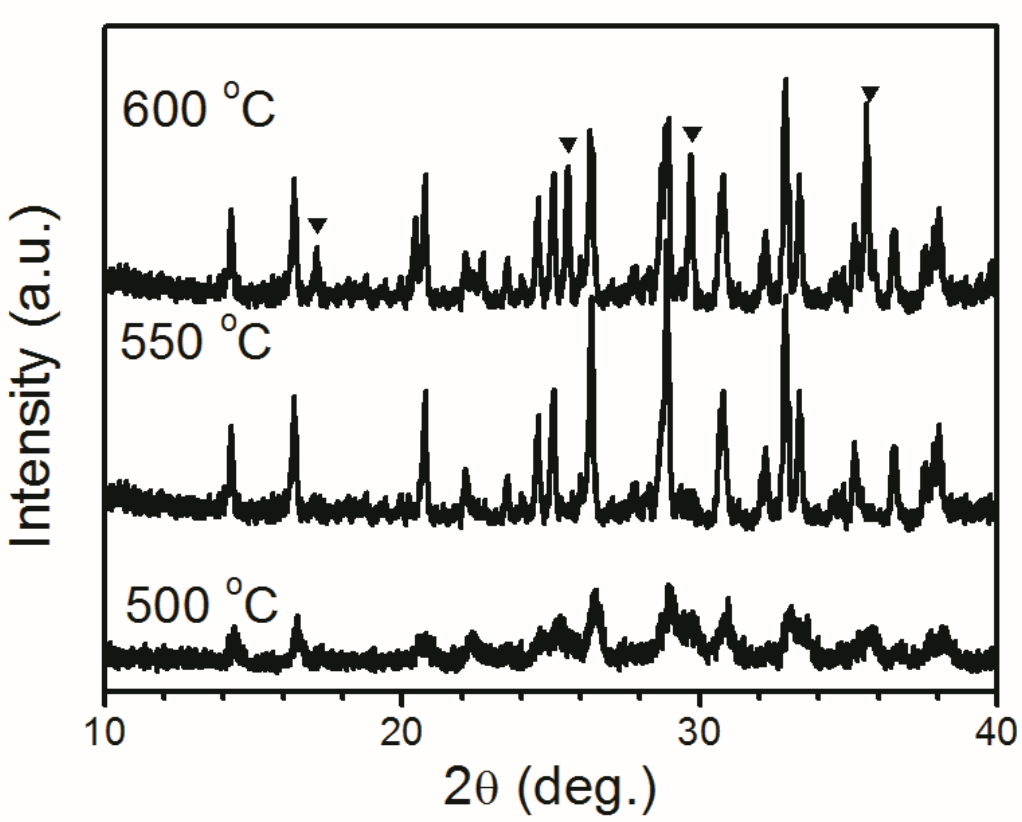

Figure 4.1. XRD patterns of LFPO powders annealed at 500 °C, 550 °C, and 600 °C.

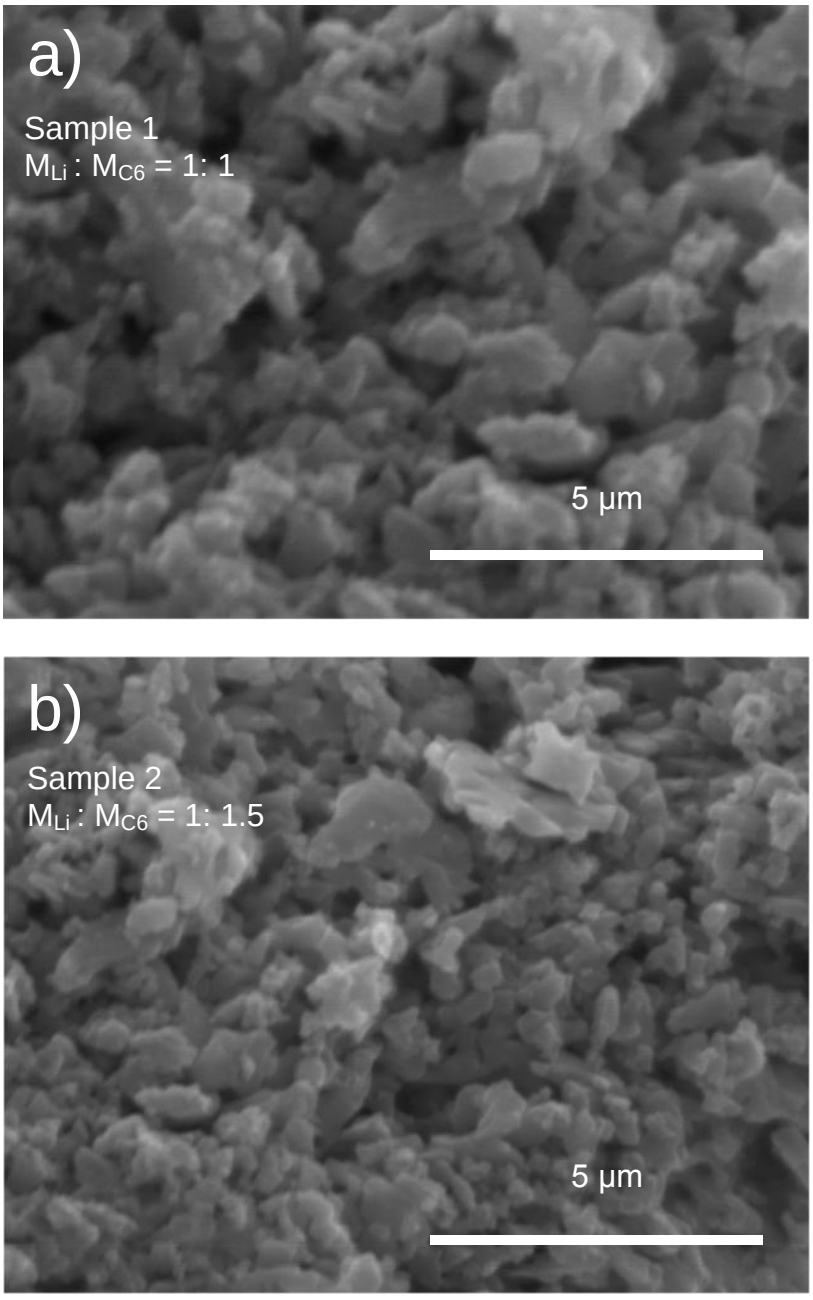

Figure 4.2. SEM images of the (a) premodified and (b) modified LFPO powders.

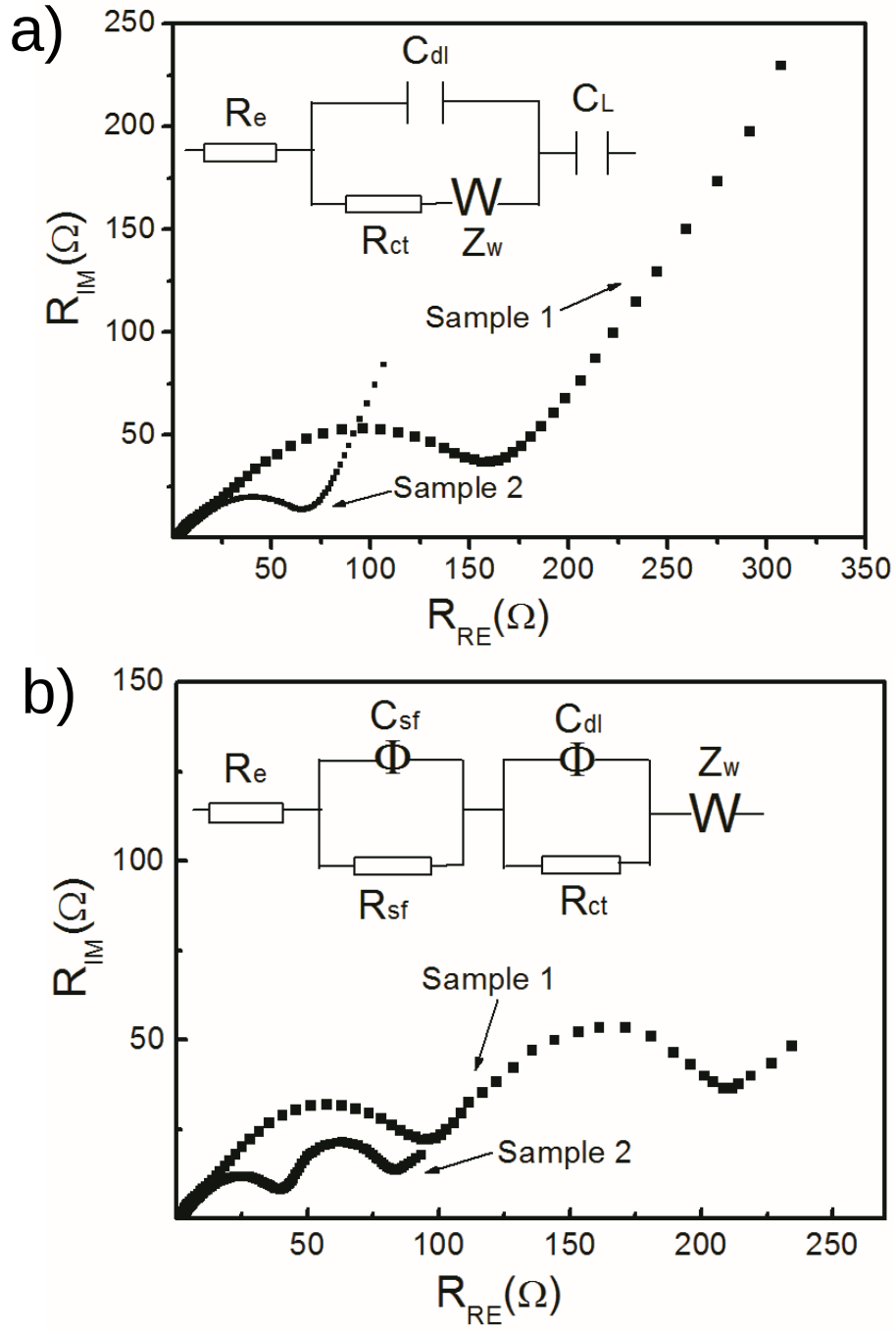

Figure 4.3. (a) EIS and equivalent circuit of the as-assembled lithium-ion cells; (b) EIS and equivalent circuit of the cells charged after the first time.

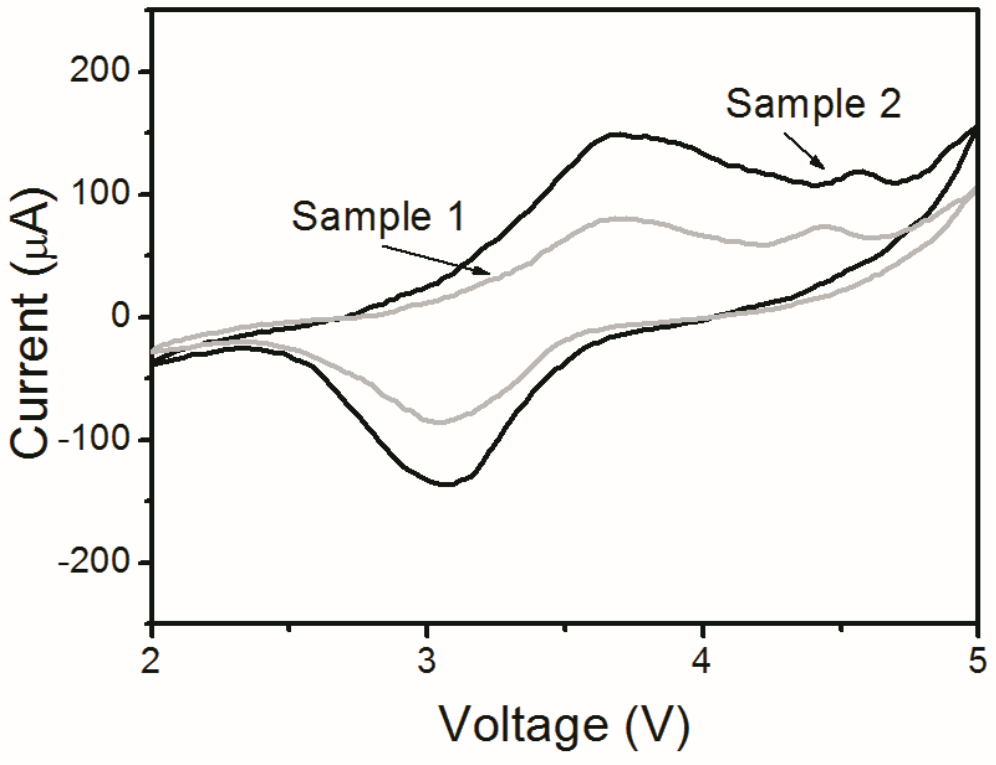

Figure 4.4. Cyclic voltammegrams of the cells scanned at a rate of 0.05 mV/S.

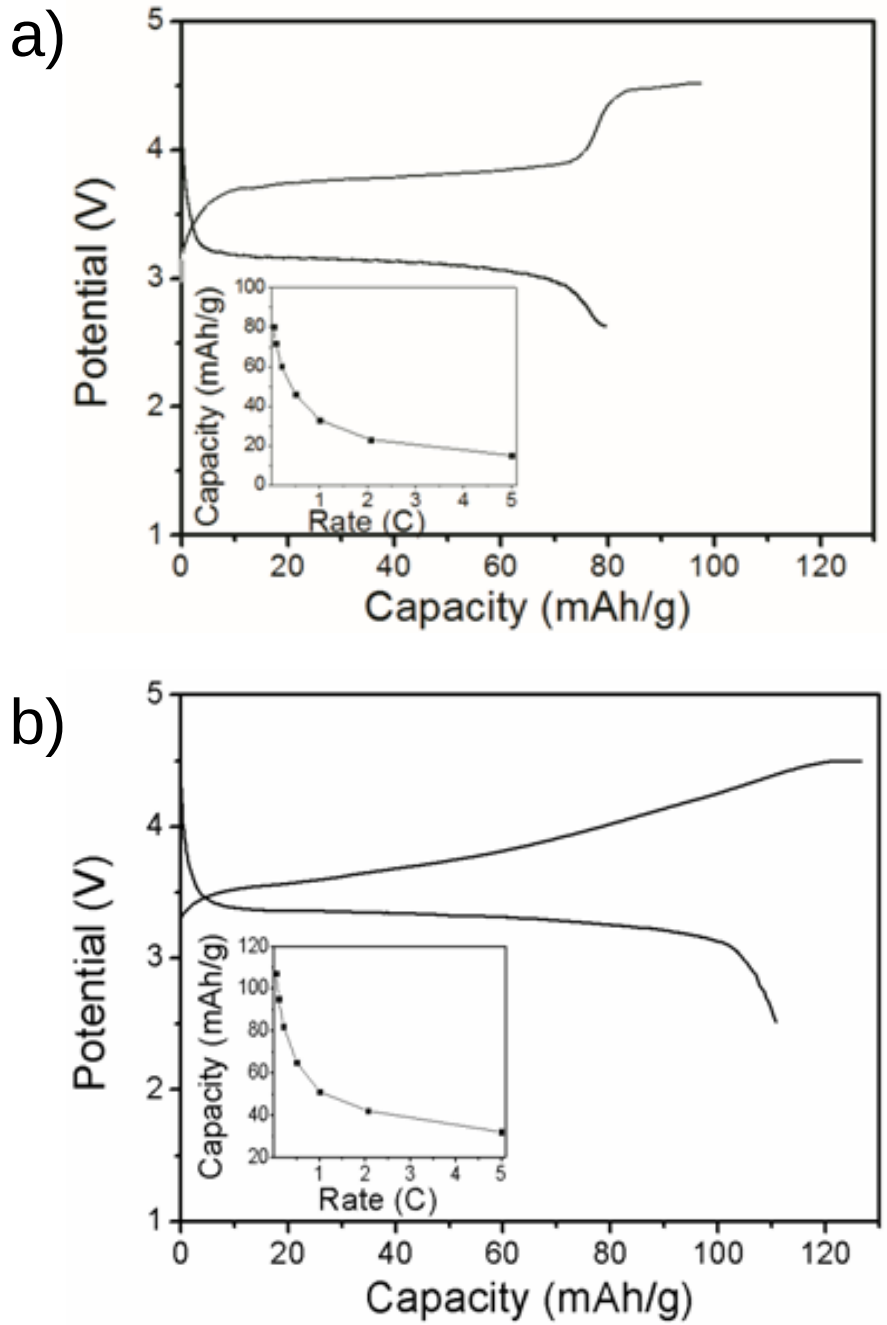

Figure 4.5. Cycling performances of the cells made with (a) sample 1 and (b) sample 2 as the cathodes.

CHAPTER 5

SYNTHESIS AND CHARACTERIZATION OF GARNET-TYPE SOLID-STATE ELECTROLYTE

5.1 Abstract

High quality garnet-type $Li_7La_3Zr_2O_{12}$ solid electrolyte was synthesized using a solution-based technique. The electrolyte pellets were sintered at 900 ^oC, resulting in tetragonal phase, which then transformed to cubic phase after annealing at 1230 ^oC. The ionic conductivity of both phases was studied and revealed to be $3.67x10^{-7}$ S/cm and 1.67×10^{-4} S/cm, respectively. A proto-type cell comprised of $Li_7La_3Zr_2O_{12}$ electrolyte, $LiCoO_2$ cathode and lithium metal anode was assembled. The cell made with the cubic phase electrolyte exhibited superior performance than the one made with the tetragonal phase electrolyte. The former cell possessed a very promising gravimetric discharge capacity of 3.4 mAh/g, which is the highest value obtained among similar setups.

Jiajia Tan and Ashutosh Tiwari, Synthesis of cubic phase $Li_7La_3Zr_2O_{12}$ electrolyte for solid-state lithium-ion batteries, Electrochem. Solid-State Lett., 15 (3) A37-A39 (2012) Reproduced by permission of ECS - The Electrochemical Society; new materials have been added.

5.2 Introduction

Lithium-ion batteries have attracted tremendous attention over the last several decades. Presently, attempts are being made to use these batteries to power vehicles to avoid CO_2 and other pollutants emitted by conventional gasoline driven vehicles. These new applications require lithium-ion batteries to possess high safety, large energy density, long life time and tolerance to high temperatures. The present liquid electrolyte-based lithium-ion batteries cannot satisfy these requirements because they use organic liquid electrolytes which are flammable and volatile, and tend to leak and decompose at high temperatures [1-4]. Therefore, recent research has been focused on solid-state electrolytes which are expected to be electrochemically stable and can also meet other requirements [5].

A newly developed inorganic solid-state electrolyte material, $Li_7La_3Zr_2O_{12}$ (LLZO) has created much enthusiasm in this field due to its high ionic conductivity, good compatibility with lithium metal and stability in air [6-10]. LLZO is a garnet-type material that has two stable phases: the tetragonal phase and the cubic phase. Although the tetragonal phase can be obtained at lower synthesis temperatures than the cubic phase, the latter has a bulk conductivity of $\sim 10^{-3}$ S/cm, compared to $\sim 10^{-6}$ S/cm for the former [11, 12]. Moreover, the cubic phase LLZO is very stable in air while the tetragonal phase suffers from a phase transition occurring at around 100 – 150 °C in air [13].

In most of the earlier reports, LLZO was prepared by conventional solid-state processes which involve multiple grinding and high-temperature sintering [11]. Li is a very volatile element, hence, high temperature sintering for long durations can result in significant nonstoichiometry in the material. In order to get stoichiometric materials it is

essential to develop a low temperature method which involves no or fewer high temperature steps. In this regard some efforts were made by Kokal et al. who used a sol-gel method to synthesize LLZO [14]. Though they could prepare LLZO by this method, the material was predominantly in tetragonal phase and exhibited a very low ionic conductivity of 3.12×10^{-7} S/cm.

In this work, we are reporting on a solution based process to synthesize high-quality cubic phase LLZO possessing very high ionic conductivity. Detailed characterization and fabrication of a proto-type all-solid-state battery using LLZO electrolyte are also being reported.

5.3 Experimental Procedure

The experimental procedures for synthesizing LLZO are illustrated in Figure 5.1. Firstly, high purity powders of Li_2CO_3, La_2O_3 and $ZrO(NO_3)_2\cdot6H_2O$ procured from AlfaAesar were used as the starting materials. These materials were dissolved in diluted nitric acid and mixed together to form a transparent solution. A ratio of Li: La: Zr in the solution was maintained as 7.7: 3: 2. The excess 10% of Li was used to compensate for the loss of lithium during the sintering steps involved in the later stages of processing. Citric acid was added to the above solution to act as a chelating agent. The pH value of the mixture was adjusted to around 2 which ensured that all the constituents remained dissolved in the solution. The resulting solution was refluxed for 1 hour and then evaporated and dried to get white powder. The powder was heated at 800 ^{o}C for 10 hours in flowing air. In the next step, the powder was ground and pressed into several pellets under a pressure of 3500 psi. Calcination of these pellets was performed in air at different

temperatures over the range of 900 ^{o}C to 1230 ^{o}C for 8 hours. The ramp rate for heating and cooling was maintained at 1 °C/min.

Structural characterization of the synthesized material was performed using the X-ray diffraction (XRD) technique with CuK_{α} radiation (λ = 1.54 Å). Morphology of the pellets was examined by scanning electron microscope (SEM) and their elemental composition was determined by energy-dispersive X-ray spectroscopy (EDS). The ionic conductivity of the sintered pellet (2.1 mm thick) was determined by the electrochemical impedance spectroscopy (IES) function of the Gamry 600 electrochemical analyzer. For this, gold electrodes were deposited on both sides of the pellet using a DC-sputtering system. The frequency range of the impedance spectroscopy was between 1MHz and 10Hz. A proto-type Li/LLZO/$LiCoO_2$ cell was prepared by simple tape-casting of $LiCoO_2$ powders on the surface of the LLZO pellet. For this, polyvinylidene fluoride (PVDF) was dissolved into n-methylpyrrolidone (NMP) solvent, forming a viscous slurry; then $LiCoO_2$ powders were mixed into the slurry to attain a weight ratio of 85: 15 for $LiCoO_2$: PVDF. The obtained mixture was pasted onto one surface of the pellet evenly and then covered by a piece of aluminum foil to act as the current collector. Mass loading of $LiCoO_2$ per unit area was 6 mg/cm^2. The pellet with the $LiCoO_2$ coating was dried at 100 °C for 1 hour and then a prototype battery was assembled in an argon environment using lithium metal foil as the anode. The assembled cell was heated at 90 °C for 1 hour to enhance the contact between the lithium foil and the electrolyte.

5.4 Results and Discussion

Figure 5.2 shows the XRD patterns of the samples sintered at 900 °C and 1230 °C. As can be seen, the sample sintered at 900 °C is tetragonal, showing characteristic double

peaks. The crystals belong to $I4_1/acd$ space group, and the lattice constants were calculated to be a = 13.149 Å, and b = 12.698 Å (a = 13.134 Å, b = 12.663 Å) [15]. The pellet sintered at 1230 °C possessed cubic crystals, in the space group of Ia-3d. Using the Rietveld refinement, the lattice constant was found to be a = 12.8974 Å (similar to a = 12.9682 Å in the literature [10]). Here, it is important to note that though the final sintering temperature required for getting the desired cubic phase in our method is almost the same as required in solid-state methods, our method avoids repetitive heating and grinding steps and hence, the total sintering time is much less than that needed in solid-state methods.

Figure 5.3 (a) shows the SEM image of the LLZO material synthesized at 900 °C for 8 hours. As you can see, the grains size is less than 5 μm and the connections between grains are quite poor. Figure 5.3b shows the SEM image of the pellet sintered at 1230 ^{o}C. The grains are larger with an average size of 10 micron. Moreover, the grains contacted one another via grain boundaries, forming a continuous conduction path for lithium ions. Figure 5.4 (a) and (b) show the SEM images of the cross-section and the polished surface of the LLZO pellet sintered at 1230 ^{o}C. Though there were some holes, the pellet was quite solid, having a density of 7.53 g/cm^3.

EDS measurement was conducted on the LLZO sample sintered at 1230 ^{o}C. The counts for oxygen, lanthanum and zirconium were found close to the stoichiometric atomic ratio. The elemental mapping for O, La and Zr is presented in Figure 5.4. These images clearly show that the three elements are distributed evenly throughout the surface, indicating the absence of phase separation or nonstoichimetric area. The EDS results for the elemental ratios of lanthanum, zirconium and oxygen for both the bulk and surface of

the sintered pellet are shown in Table 5.1. Though the lithium element cannot be directly detected by EDS technique, the atomic ratios of oxygen: lanthanum: zirconium were quite similar on the surface as well as in the bulk of the pellet and were close to the values expected in stoichiometric material.

As suggested by very broad XRD peaks, the as-prepared sol-gel powders (before calcination) were nano-sized, possessing very high surface to volume ratio. Direct heating of those powders to 1230 °C could have resulted in severe lithium evaporation. So to avoid the above problem, we performed sintering in two steps. In the first step, the sol-gel prepared powders were calcined at 800 ^{o}C for 10 hours. This resulted in grain-growth and hence, a reduction in the over-all surface to volume ratio. In the second step, compressed powders were calcined at 1230 ^{o}C for 8 hours. Because of the reduced surface to volume ratio of the powders and the short calcination time, the problem of lithium evaporation was eliminated as confirmed by the EDS results shown in Table 5.1.

Figure 5.6 displays the room temperature Nyquist plots of the complex impedance for the tetragonal and cubic phase LLZO pellets, which were covered by ion-blocking Au electrodes. The curves could be regarded to consist of a compressed semicircle and a tail. The compressed semicircle at high frequencies could originate from the total electrical resistance through the bulk and grain boundaries. The tail at the low frequency range represents capacitive behavior between the ionic blocking gold electrodes, indicating the ionic nature of the LLZO pellet. The impedance data were fitted to an equivalent circuit model of $(R_{tol}//Q_{tol})Q_{el}$(solid line), where R_{tot} is the total resistance, Q is the constant phase element [14]. From the fitting results, the room temperature ionic conductivity was found to be $3.67x10^{-7}$ S/cm for the tetragonal phase LLZO, while the obtained value for

cubic phase LLZO was 1.67×10^{-4} S/cm, almost 3 orders of magnitude higher than the former.

In order to make an estimate of the activation energy, temperature dependent measurement of total ionic conductivity was performed over the range of room temperature to 100 °C (Figure 5.7). The ionic conductivities were found to fit well in the Arrhenius equation:

$$\sigma = (A/T)\exp(-E_a/(kT)) \quad (5.1)$$

where σ is the electrical conductivity, A is a constant, T is the absolute temperature, E_a is the activation energy and k is the Boltzmann's constant. Activation energy was calculated to be 0.61 eV and 0.36 eV for tetragonal and cubic LLZO, respectively.

In order to investigate the electrochemical performances of the cubic LLZO as an electrolyte in lithium-ion batteries, a prototype Li/LLZO/$LiCoO_2$ cell was fabricated using cubic phase LLZO. Room temperature EIS of the as-assembled cell is shown in Figure 5.8. The diagram shows a big semicircle in medium frequency range, which is not seen in the impedance plot of the Au/LLZO/Au cell. Therefore, it would originate from the Li+ transport across the interface between the electrolyte and electrode. By fitting the data to a model of $(R_{el}Q_{el})(R_{ct}Q_{ct})(R_{sf}Q_{sf})W$ (solid line), the interfacial resistance was estimated to be 23 kΩ. The large interfacial resistance is likely due to poor interfacial contact between the solid electrolyte and the cathode, resulting in impediment in lithium transport across the interface. Vapor based deposition techniques can be used to improve the solid-solid interfacial contact.

Figure 5.9 shows the first charge/discharge cycle at 2 $\mu A/cm^2$ for the Li/LLZO/$LiCoO_2$ cell recorded at room temperature. The cell was rechargeable with a gravimetric discharge capacity of 3.4 mAh/g, which is 2.5 % of the theoretical capacity of $LiCoO_2$ (136.7mAh/g). The above experimentally achieved discharge capacity is the highest among similar setups using tape-casted $LiCoO_2$ powders as the cathode. However, it is still much less than the desired capacity needed for practical applications. The capacity can be further increased by: (i) reducing the interfacial resistance and (ii) densifying and reducing the thickness of the electrolyte layer. Just a note, the cell using tetragonal LLZO as the electrolyte exhibited very little discharge capability, less than 1 mAh/g, and thus was not shown here.

5.5 Summary

We have successfully synthesized the LLZO solid electrolyte through a solution-based technique. The room temperature ionic conductivity of the tetragonal and cubic phase LLZO pellets was found to be $3.67x10^{-7}$ S/cm and 1.67×10^{-4} S/cm, respectively. Formation of the high-purity, stoichiometric, cubic phase $Li_7La_3Zr_2O_{12}$ by a fast solution based process is very important for realizing all-solid-state batteries. A discharge capacity of 2.5 % of the theoretically attainable value has been achieved in a prototype battery formed using cubic $Li_7La_3Zr_2O_{12}$ as the electrolyte, $LiCoO_2$ as the cathode and a lithium foil as the anode. Therefore, the cubic phase LLZ O is a very promising solid electrolyte for achieving safe and high power LIBs.

5.6 References

1. J. Trevey, J. S. Jang, Y. S. Jung, C.R. Stoldt and S. H. Lee, *Electrochem. Commun.,* **11**, 1830 (2009).

2. A. Hayashi, S. Hama, F. Mizuno, K. Tadanaga, T. Minami and M. Tatsumisago, *Solid State Ionics,* **175**, 683 (2004).

3. J. E. Trevey, Y. S. Jung and S. H. Lee, *Electrochem. Acta*, **56**, 4243 (2011).

4. A. Sakuda, H. Kitaura, A. Hayashi, K. Tadanaga and M. Tatsumisago, *J. Electrochem. Soc.*, **156**, A27 (2009).

5. J. W. Fergus, *J. Power Sources*, **195**, 4554 (2010).

6. S. Kumazaki, Y. Iriyama, K. H. Kim, R. Murugan, K. Tanabe, K. Yamamoto, T. Hirayama and Z. Ogumi, *Electrochem. Commun.,* **13**, 509 (2011).

7. K. H. Kim, Y. Iriyama, K. Yamamoto, S. Kumazaki, T. Asaka, K. Tanabe, C. A. J. Fisher, T. Hirayama, R. Murugan and Z. Ogumi, *J. Power Sources*, **196**, 764 (2011).

8. J. Awaka, A. Takashima, K. Kataoka, N. Kijima, Y. Idemoto and J. Akimoto, *Chem. Lett.,* **40**, 60 (2011).

9. J. Awaka, A. Takashima, H. Hayakawa, N. Kijima, Y. Idemoto and J. Akimoto, *Key Eng. Mat.,* **485**, 99 (2011).

10. A. Kuhn, S. Narayanan, L. Spencer, G. Goward, V. Thangadurai and M. Wilkening, *Phys. Rev. B*, **83**, 094302 (2011).

11. R. Murugan, V. Thangadurai and W. Weppner, *Angew. Chem. Int. Ed.*, **46**, 7778 (2007).

12. J. Awaka, N. Kijima, H. Hayakawa and J. Akimoto, *J. Solid State Chem.*, **182**, 2046 (2009).

13. C. A. Geiger, E. Alekseev, B. Lazic, M. Fisch, T. Armbruster, R. Langner, M. Fechtelkord, N. Kim, T. Pettke and W. Weppner, *Inorg. Chem.,* **50**, 1089 (2011).

14. I. Kokal, M. Somer, P.H.L. Notten and H. T. Hintzen, *Solid State Ionics*, **185**, 42 (2011).

15. M. Kotobuki, H. Munakata, K. Kanamura, Y. Sato and T. Yoshida, *J. Electrochem. Soc.,* **157**, A1076 (2010).

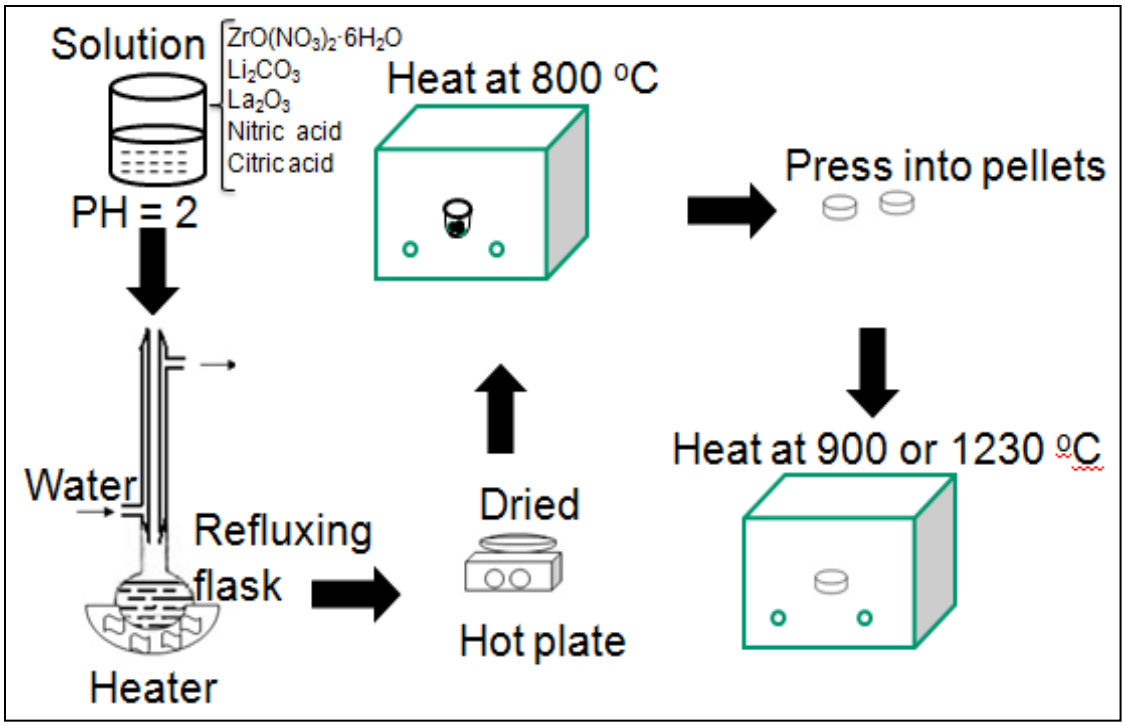

Figure 5.1. The schematic drawing of the experimental procedures.

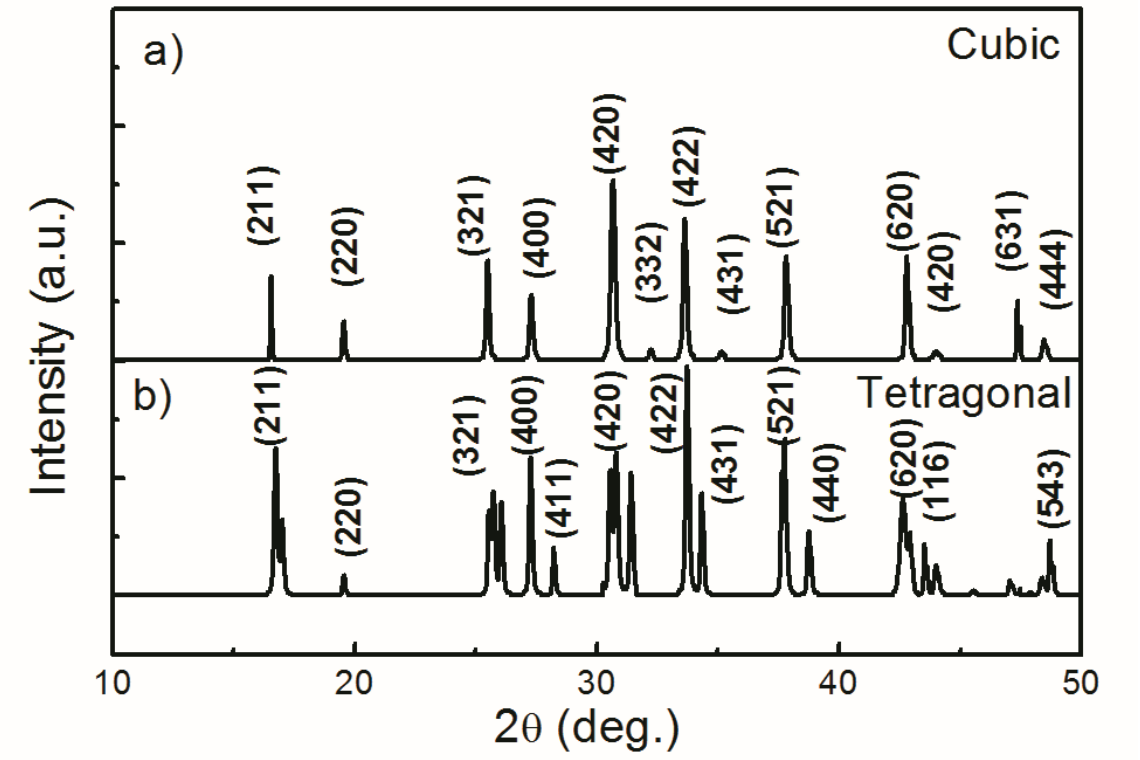

Figure 5.2. XRD patterns of the LLZO pellets sintered at (a) 1230 ^{o}C and (b) 900 ^{o}C.

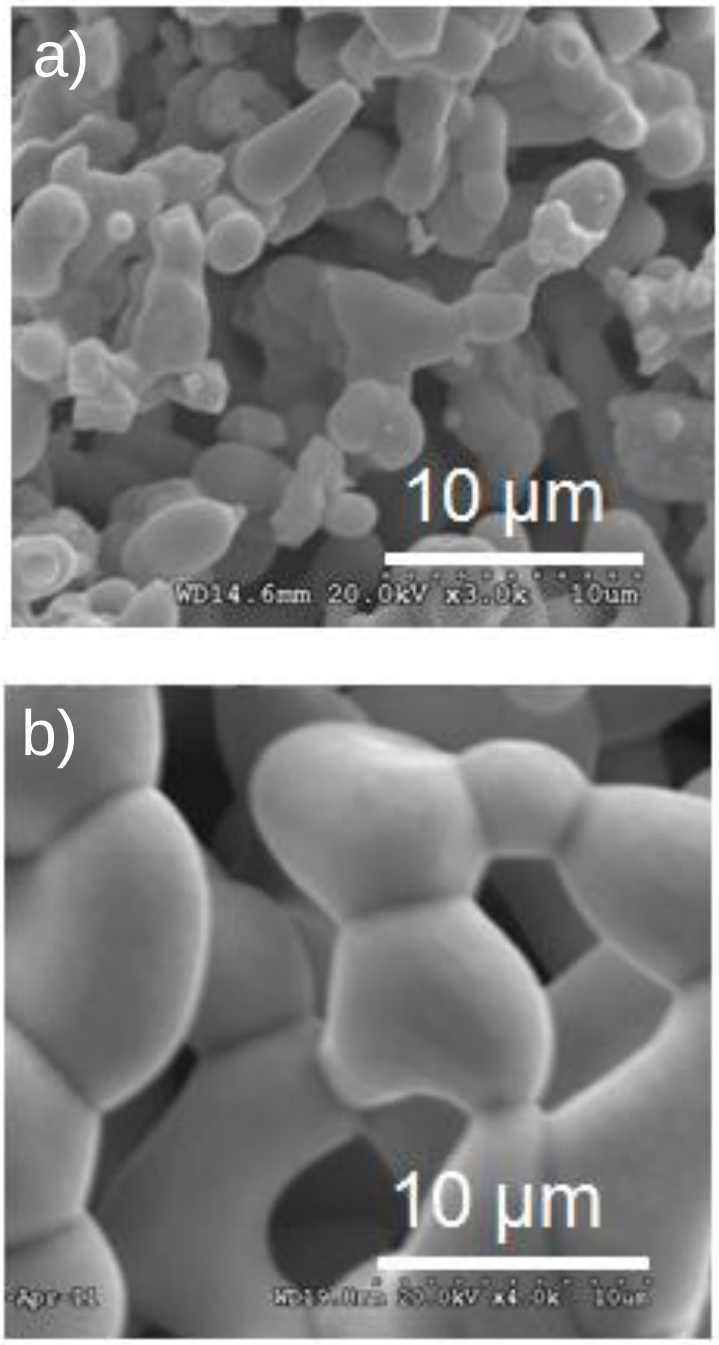

Figure 5.3. SEM images of the LLZO pellets sintered at (a) 900 ^{o}C and (b) 1230 ^{o}C.

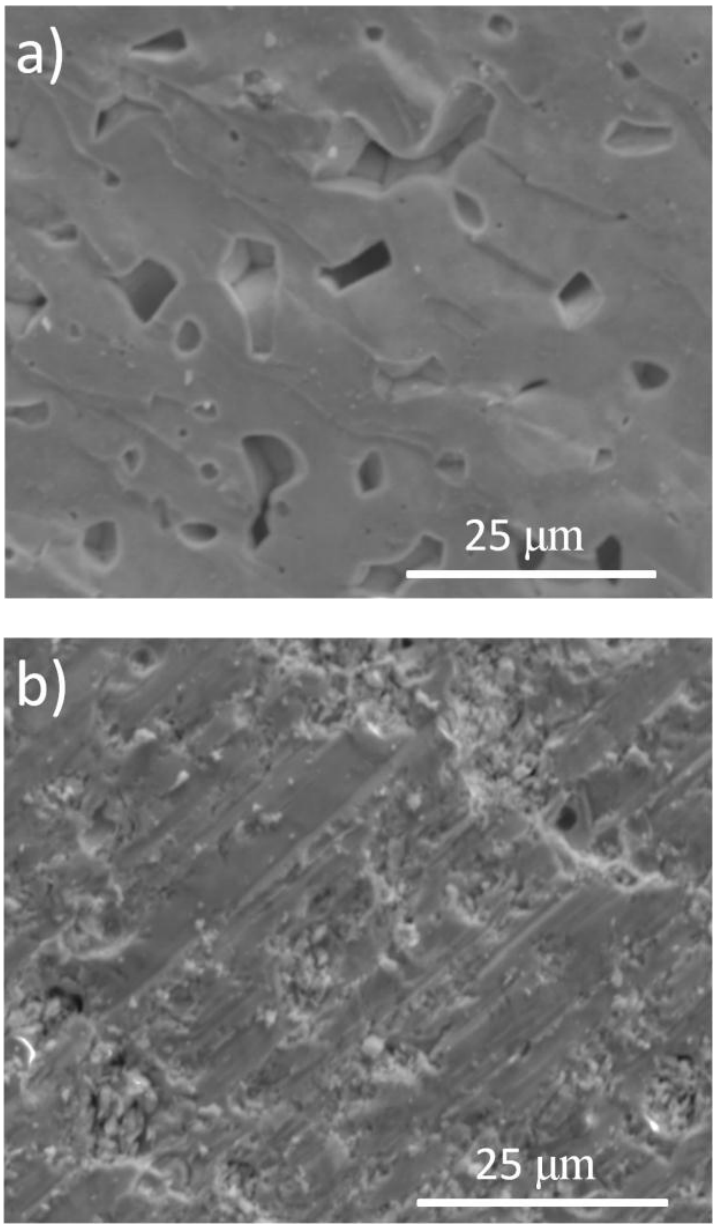

Figure 5.4. SEM images of: (a) cross-section and (b) surface of the LLZO pellet sintered at 1230 ^{o}C.

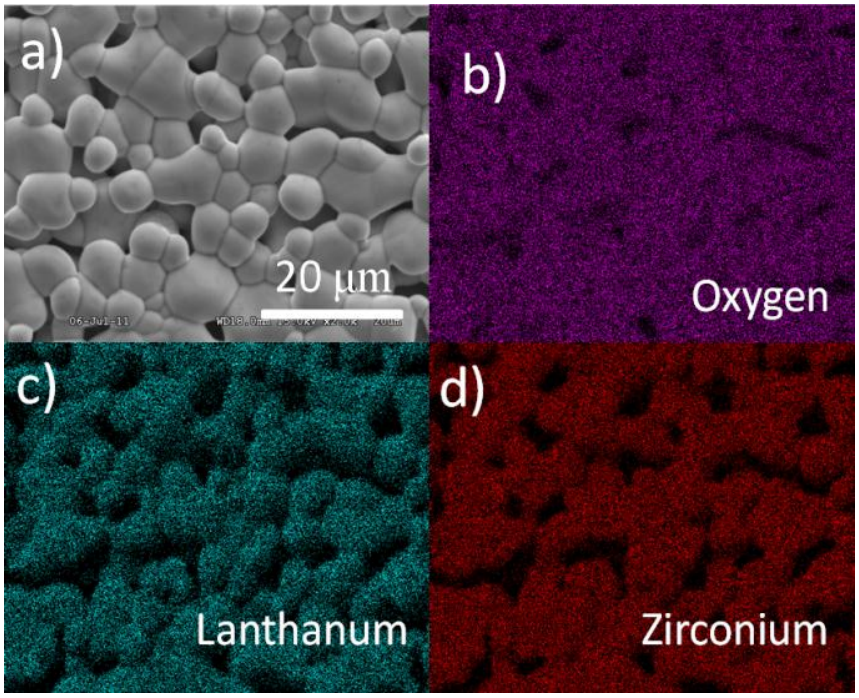

Figure 5.5. Elemental mapping of oxygen, lanthanum and zirconium on LLZO pellet sintered at 1230 ^{o}C.

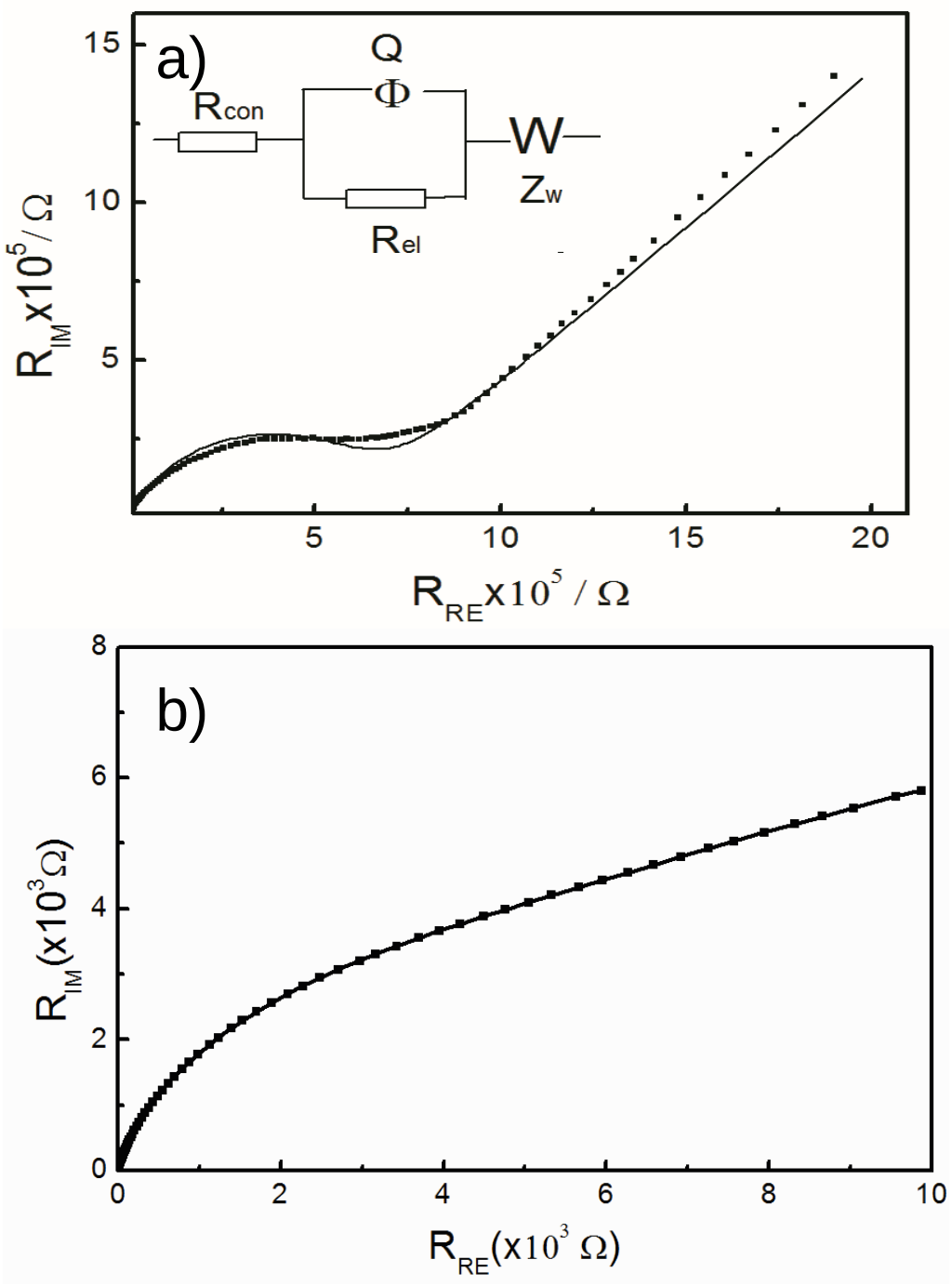

Figure 5.6. Nyquist impedance plots of the LLZO pellets sintered at (a) 900 ^{o}C and (b) 1230 ^{o}C.

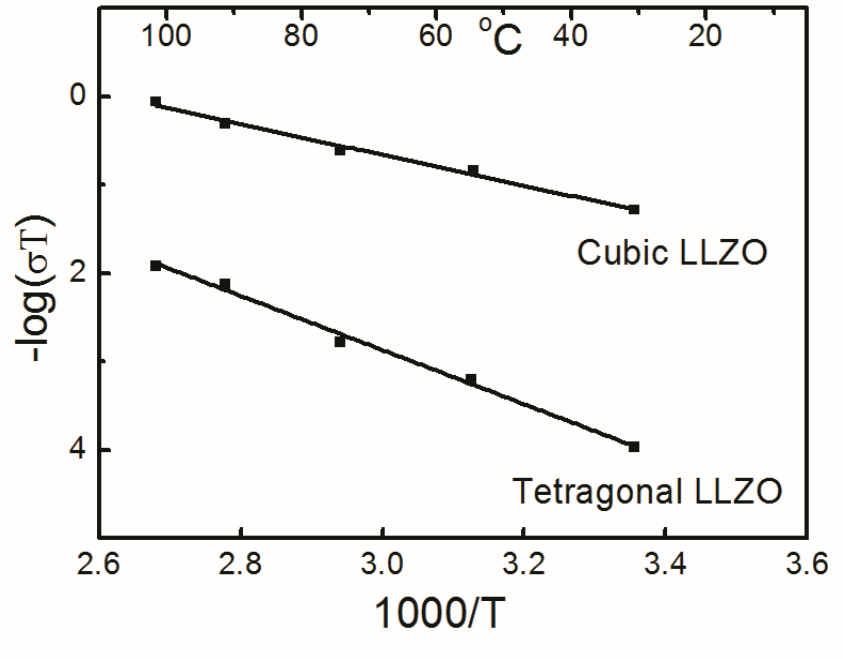

Figure 5.7. Arrhenius plot of the electrical properties for LLZO pellets.

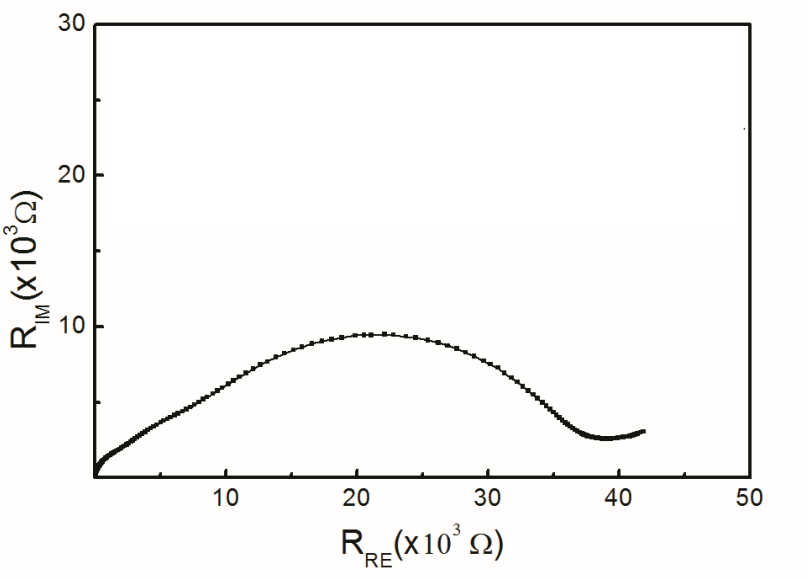

Figure 5.8. EIS spectrum of the Li/LLZO/$LiCoO_2$ prototype battery.

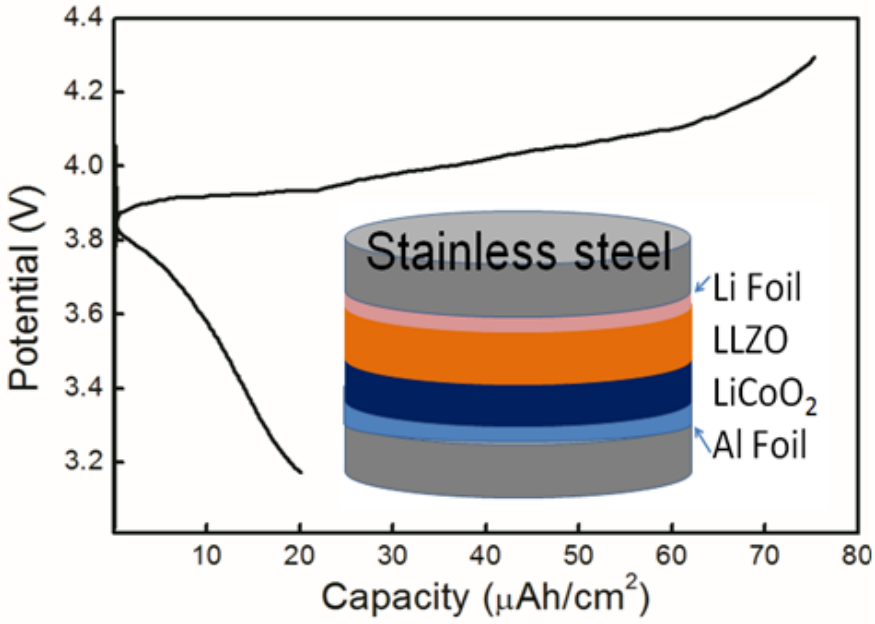

Figure 5.9. The first charge/discharge curves and schematic drawing of the Li/LLZO/$LiCoO_2$ battery.

Table 5.1: Elemental ratios for the surface and the bulk of the sintered pellet.

	Surface			Bulk		
	O	La	Zr	O	La	Zr
Atomic %	67.72 %	19.38 %	12.90 %	69.96 %	17.91 %	12.13 %
Integration Error	1.01	0.99	1.03	0.85	1.36	1.33
Peak/Background	35.79	9.23	9.13	64.93	8.91	7.75

CHAPTER 6

FABRICATION AND CHARACTERIZATION OF $Li_7La_3Zr_2O_{12}$ THIN-FILM ELECTROLYTE

6.1 Abstract

Thin films of $Li_7La_3Zr_2O_{12}$ were deposited at room temperature using a pulsed-laser-deposition process. Detailed structural, compositional, optical, and electrochemical characterizations of the films were performed. The films deposited at room temperature had amorphous structure, and exhibited a lithium-ion conductivity of 3.35×10^{-7} S/cm. The effects of annealing on the properties of the films were investigated. Films annealed at 1000 ℃ were found to have cubic crystals; but, the lithium-ion conductivity of the thermal-annealed films was inferior. However, laser annealing on the films was found to enhance the ionic conductivity to 7.36×10^{-7} S/cm. Moreover, the as-deposited thin films were found to be electrochemically stable against lithium metal.

6.2 Introduction

The last few decades have seen a drastic miniaturization of electronic devices following the famous Moore's law predicted by Gordan Moore in 1971. These developments in the electronic industry have resulted in ultra-low-weight electronic

---

Jiajia Tan and Ashutoshi Tiwari, Fabrication and characterization of $Li_7La_3Zr_2O_{12}$ thin films for lithium ion battery. Reproduced by permission of ECS - The Electrochemical Society; some images and grammar have been changed.

devices such as palm-top computers, smart phones, tablet PCs, etc. Batteries constitute one of the most important and essential components of these devices. At present, lithium-ion batteries are considered the most suitable candidate for use in portable electronic devices. However, these batteries are available only in bulk form and comprise a significant percentage of the overall weight of the device. As the miniaturization of electronic devices continues, we need more advanced batteries which are light weight, safe, and environment friendly. One possible solution is the development of thin-film batteries (TFBs) which can be integrated onto the microprocessor chips themselves. A major hurdle in achieving thin-film-lithium-ion batteries is the fact that the present lithium-ion battery technology utilizes liquid electrolytes. Liquid electrolytes cannot be used for making thin-film batteries. For these applications, we would require solid-state (SS) electrolytes. Moreover, to be able to integrate TFBs with microprocessor chips we will have to develop ways of growing electrolyte films at low temperatures.

As far as the research in SS electrolytes is concerned, many different kinds of inorganic electrolytes have been analyzed to date. These include Lisicon-type electrolytes, [1, 2] garnet-type Li ion conductors, [3, 4] perovskite-type lithium lanthanum tantantes, [5, 6] and sulfide glasses/ceramics [7, 8]. Among all of them, garnet type $Li_7La_3Zr_2O_{12}$ (LLZO), synthesized lately by Weppner's group [9] has been reported to possess very high ionic conductivity (10^{-6} S/cm for tetragonal phase and 10^{-3} S/cm for cubic phase). What's more, LLZO is chemically stable with a potential window wider than 0 - 7 V, is environment friendly, and is relatively inexpensive [9-12]. Since this garnet-type LLZO has shown nice performance as a solid electrolyte in the bulk form, it is expected to show satisfying properties as a thin-film electrolyte. To the best of our knowledge, the LLZO

electrolyte has only been synthesized as a bulk phase, with no research having been reported on LLZO thin films.

Given that LLZO is a complex oxide material, the preservation of stoichiometry from the target to the film would be very hard by conventional evaporation techniques. Therefore, a pulsed laser deposition system was employed. Utilizing highly energetic laser pulses, the target surface absorbs over 1 GW/cm^2 power density and as a result all the elements are ablated at the same rate despite their usually different partial pressures in the vapor phase; thus, the stoichiometry of the deposited film is more likely to be maintained. Considering that thin-film batteries are fabricated at low temperatures, we explored the pulsed laser deposition of LLZO films at room temperature. The as-deposited films were annealed ex-situ to achieve better crystallinity. The structural features, optical properties and electrical behavior of the as-deposited and postannealed films were characterized and illustrated.

6.3 Experimental Procedure

A high purity LLZO target was synthesized by a solution-based technique. Stoichiometric amounts of Li_2CO_3, La_2O_3 and $ZrO(NO_3)_2 \cdot 6H_2O$ powders were dissolved in nitric acid and mixed with the chelating agent (citric acid). The solution was refluxed for 1 hour and concentrated to gel before drying into powders. The obtained powders were heated in air at 800 °C for 10 hours, and were finally sintered at 1230 ^oC for 8 hours [13]. In order to compensate the lithium loss during laser deposition, a Li_2O target was prepared by sintering high purity Li_2O powders at 750 °C for 8 hours in flowing oxygen. A pulsed laser deposition (PLD) system using KrF excimer laser (248 nm wavelength and 25 ns pulse width) was employed. Both the LLZO target and the Li_2O target were

introduced into the PLD chamber. For every 100 shots of laser from LLZO target, 10 shots from Li_2O were added, resulting in a total of 7,700 shots. The laser pulse frequency was set to 10 Hz and the energy fluence was kept at $3J/cm^2$. The target was ablated by the laser with an incident angle of 45 °; the generated bright plume deposited material on an axis normal to the substrates which were 4.5 cm away from the target. The oxygen pressure in the chamber was varied from 10^{-3} mbar to 0.8 mbar, with 0.4 mbar found to be the most suitable value for achieving films of good stoichiometry. The films were postannealed at different temperatures up to 1000 °C for 30 minutes at a ramp rate of 5 °C/min.

Single crystalline $SrTiO_3$ (STO) in the <100> orientation was used as one of the substrates in our experiment; it has a cubic structure similar to that of LLZO. The crystal structure and surface morphology of the films deposited on STO were characterized by X-ray diffraction (XRD) using CuKα radiation (λ = 1.54 Å) and scanning electron microscopy (SEM), respectively. The measurement of electrical properties was conducted from room temperature to 60 ^oC using the electrochemical impedance spectroscopy (EIS) function of a Gamry 600. For this, Pt was deposited on the surface of STO and Au was coated on top of the LLZO film, forming an Au/LLZO/Pt cell which was heated at 80 °C for 1 hour to ensure good electrical contact. The structure of the cell is illustrated in Figure 6.1. The electrochemical stability of the thin films was investigated by cyclic voltammetry (CV) function of Gamry 600 on Li/LLZO/Pt/STO cells from -0.5 V to 5 V at a scanning rate of 10 mV/s. Also, Sapphire <0001> was used as a substrate; the reason for using sapphire is mentioned in the discussion section. The chemical composition of the films deposited on sapphire <0001> was analyzed by energy

dispersive X-ray spectroscopy (EDS). The optical properties of the films were tested by UV-VIS spectrometer, in the wavelength range of 190 nm to 1100 nm.

6.4 Results and Discussion

Figure 6.2 shows the XRD patterns of the as-deposited and annealed films that were grown on STO <100> substrates. As can be seen, the as-deposited films were amorphous, showing no diffraction peak beside the ones for substrate. After annealing at 800 °C for 30 minutes, two broad peaks appeared around the 2θ values of 27.75^{o} and 34.12^{o}. Upon further annealing at 1000 ^{o}C for 30 minutes, these peaks became sharper and several more peaks appeared. We found that these peaks correspond to the crystal orientations of cubic phase LLZO; the peaks were labeled according to the JCPDS card (Reference code: 00-045-0109). Here it is important to note that in the bulk LLZO system, the (420) peak is of the maximum intensity (100%) while the (400) peak is only about 55%. However, in our films the strongest peak was (400), while (420) peak was only 15% better as seen in Figure 6.2b. This indicates that our films may be slightly textured, having a preferred orientation in the <100> direction. The fact that just the annealing of the as-deposited films resulted in crystalline LLZO films indicates that the as-deposited films were amorphous LLZO.

The SEM images of the as-deposited and annealed thin films on STO substrates are shown in Figure 6.3. The surface of the film deposited at room temperature (Figure 6.3a) was quite smooth with scattered dots which can be reduced by elongating the target-to-substrate distance. The surface of the film became less continuous after sintering at 1000 °C (Figure 6.3b), due to different thermal expansion coefficients between the film

and the substrate. The thickness of the as-deposited film was revealed to be around 1 μm as seen from the cross-sectional image (Figure 6.3c).

In order to verify the chemical composition of the film, we conducted EDS measurements on the LLZO films grown on sapphire. The reason to choose sapphire as the substrate instead of STO is that the unique set of peaks for zirconium are overlapping with those of strontium in their EDS spectra. Figure 6.4 shows the EDS result for the cross-section of the as-deposited film. It was found that the counts for lanthanum and zirconium were close to the stoichiometric atomic ratio. The inset figure shows the counts of zirconium along the cross-section of the sample, from which we could confirm that the film thickness (marked by the gray bar) was around 1 μm.

The measurement of optical transmission properties can help us understand more about our films. The obtained optical transmission spectra of the as-deposited and annealed films are shown in Figure 6.5a. As you can see, the overall transmittance decreases for the annealed films in comparison to the as-deposited ones. This reduction is possibly due to the grain growth and defect formation in the films, also evidenced by the films shifting from transparent to opaque after annealing. It is shown that the transmission edge of the films shift to longer wavelengths after annealing, indicating a reduction of the optical band gap E_g. E_g can be directly found out by fitting the absorption data with the following equation:

$$\alpha = A(h\nu - E_g)^n / h\nu \quad (1)$$

where α is the absorption coefficient, A is a constant, and n = ½ for direct band gap and 2 for indirect band gap materials [14]. The values of band gaps calculated by fitting the

above equation are shown in Figure 6.5b. The linear behavior of the curve when n = ½ reveals the direct band-gap nature of the thin films. E_g is the intercept value when extrapolating the linear portion to the energy axis. The optical band gap of the as-deposited LLZO thin film was found to be 5.13 eV, which decreased to 3.64 eV after annealing at 1000 ^oC. This is the first ever report of the optical bandgap of LLZO.

Electrical properties of the LLZO thin films were investigated for their potential application as solid-state electrolyte in lithium-ion batteries. For this, an Au/LLZO/Pt/STO cell was fabricated as described in the experimental section. Figure 6.6 shows the Nyquist impedance plots of the as-deposited films, in the frequency range of 1 MHz to 100 Hz. The curve could be regarded to consist of a semicircle in the high frequency range and a tail in the low frequency range. The impedance data can be fitted by an equivalent circuit model drawn in the same figure, where R_{con} is the contact resistance, R_{el} is the electrolyte resistance, Q is the constant phase element, and Z_w is the Warburg impedance. By fitting the equivalent circuit model to the data (black curve) with experimentally determined geometric parameters, we obtained an ionic conductivity value of 3.35 x 10^{-7} S/cm for the as-deposited stoichiometric films. This value is better than the total ionic conductivity of the tetragonal LLZO bulk samples [15]. The activation energy of the films was estimated to be 0.36 eV. The benefit of using a Li_2O target in addition to the LLZO target during deposition was confirmed by depositing other thin films just from a single LLZO target. The electrical properties of these films are shown as red dots and solid lines in Figure. 6.6. As can be seen, by removing the Li_2O target, the as-deposited film possesses a lower ionic conductivity of 7.19×10^{-8} S/cm, which may be caused by lithium loss during deposition.

The influence of annealing on the ionic conductivity of the films was also studied, and the results are shown in Figure 6.7. After annealing the films at 800 °C for 30 minutes, the ionic conductivity of the sample decreased to 1.78×10^{-7} S/cm, almost half that of the as-deposited films. This is possibly due to the increased hardness for ionic transport through the films that were full of defects and cracks formed during crystallization. Therefore, high temperature annealing is not favorable for increasing ionic conduction. Upon further annealing of films at 1000 ^{o}C, the platinum contact became oxidized and the cell showed a capacitor like behavior.

In order to enhance the ionic conductivity of the thin films, they were annealed by pulses of a highly energetic laser. Using lasers, the film will crystallize very fast and possibly crack free, since thermal expansion is a relatively slow process. The ionic conductivity of the annealed films was measured and shown in Figure 6.8. As can be seen, the semicircle of the spectroscopy for the laser-annealed film is much smaller than the as-deposited one. Further calculation showed that the ionic conductivity increased to 7.36×10^{-7} S/cm using laser pulses of 1 J/cm^2 energy density. The increase of ionic conductivity may result from the crystallization of LLZO in cubic phase. However, the conductivity value was much less than that of the bulk-phase LLZO, mostly due to the small size of the grains (the inset figure) and the limited thickness of the crystallized layer on the top of the film. For simplicity and clarity, the values of ionic conductivity and activation energy for those films were summarized in Table 6.1.

The electrochemical stability of these two kinds of films (supplemented and not supplemented by lithium) was tested in Li/LLZO/Pt/STO cells by attaching a piece of lithium on top of the films. The cyclic voltammegrams of the Li/LLZO/Pt/STO cells are

shown in Figure 6.9. The film deposited from the LLZO target is lithium ion conductive with a small cathodic peak around 1 V. However, it is not quite stable at higher bias versus Li/Li^+, as shown from the increasing anodic current at high voltages. This phenomenon might be ascribed to lithium deficiency in the electrolyte thin film. Then we tested the other cell using the film deposited from the LLZO+Li_2O targets. However, when we tested the cell that used the LLZO film supplemented with lithium during deposition, the film was found to be much more stable at higher voltages. Therefore, the addition of lithium during deposition does indeed increase the electrochemical stability of the LLZO thin films. Thus, the amorphous LLZO film prepared by pulsed laser deposition is a promising solid electrolyte for thin-film lithium-ion batteries.

6.5 Summary

We have successfully fabricated LLZO thin films through pulsed laser deposition at room temperature. The as-deposited films were amorphous and then crystallized by annealing. With the increase of annealing temperature, the optical band gap red-shifted from the original value of 5.13 eV down to 3.64 eV. The as-deposited films exhibited a good ionic conductivity of 3.35×10^{-7} S/cm at room temperature with an activation energy of 0.36 eV. Laser-annealing was found to increase the ionic conductivity of the film to the value of 7.36×10^{-7} S/cm. Moreover, the electrochemical stability of the films against lithium metal was found to be quite satisfying. In all, the LLZO thin films, are a very promising solid-state electrolyte for realizing next generation TFBs.

6.6 References

1. H. Chen, H. Tao, X. Zhao and Q. Wu, *J. Non-Cryst. Solids*, **357**, 3267 (2011).

2. J. K. Feng, L. Lu and M. O. Lai, *J. J. Alloys Compd.*, **501**, 255 (2010).

3. J. E. Trevey, Y. S. Jung and S. H. Lee, *Electrochimi. Acta*, **56**, 4243 (2011).

4. A. Sakuda and A. Hayashi, *J. Am. Ceram. Soc.*, **93**, 765 (2010).

5. W. R. Brant, S. Schmid, Q. Gu, R. L. Withers, J. Hester and M. Avdeev, *J. Solid State Chem.*, **183**, 1998 (2010).

6. A. Mei, X. L. Wang, J. L. Lan, Y. C. Feng, H. X. Geng, Y. H. Lin and C. W. Nan, *Electrochimi. Acta*, **55**, 2958 (2010).

7. V. Thangadurai and W. Weppner, *J. Solid State Chem.*, **179**, 974 (2006).

8. V. Thangadurai and W. Weppner, *Adv. Funct. Mater.*, **15**, 107 (2005).

9. R. Murugan, V. Thangadurai and W. Weppner, *Angew. Chem. Int. Ed.*, **46**, 7778 (2007).

10. I. Kokal, M. Somer, P. H. L. Notten and H. T. Hintzen, *Solid State Ionics*, **185**, 42 (2011).

11. M. Kotobuki, H. Munakata, K. Kanamura, Y. Sato and T. Yoshida, *J. Electrochem. Soc.*, **157**, A1076 (2010).

12. J. Tan and A. Tiwari, *Electrochem. Solid-State Lett.*, **15**, A37 (2012).

13. H. Buschmann, S. Berendts, B. Mogwitz and J. Janek, *J. Power Sources*, **206**, 236 (2012).

14. R. Murugan, S. Ramakumar and N. Janani, *Electrochim. Commun.*, **13**, 1373 (2011).

15. H. Buschmann, J. Dolle, S. Berendts, A. Kuhn, P. Bottke, M. Wilkening, P. Heitjans, A. Senyshyn, H. Ehrenberg, A. Lotnyk, V. Duppel, L. Kienle and J. Janek, *Phys. Chem. Chem. Phys.*, **13**, 19378 (2011).

16. F. I. Ezema and R. U. Osuji, *Chalcogenide Lett.*, **13**, 1373 (2011).

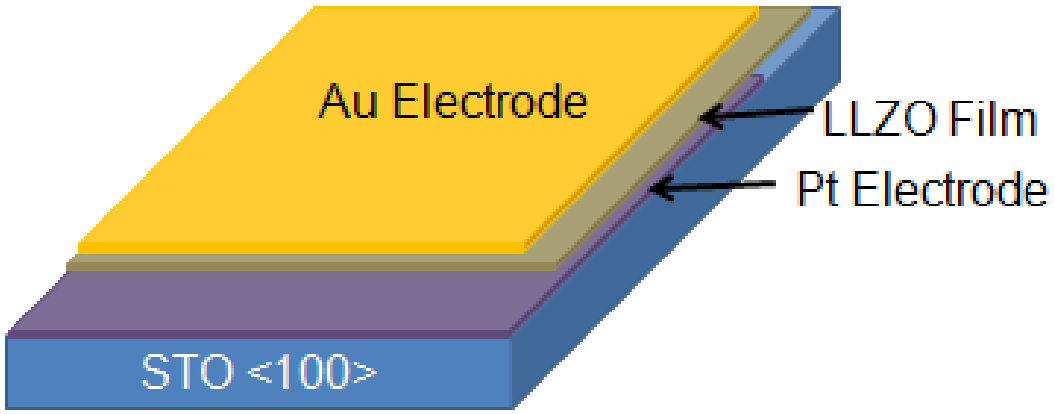

Figure 6.1. Schematic drawing of the Au/LLZO/Pt cell deposited on STO substrate.

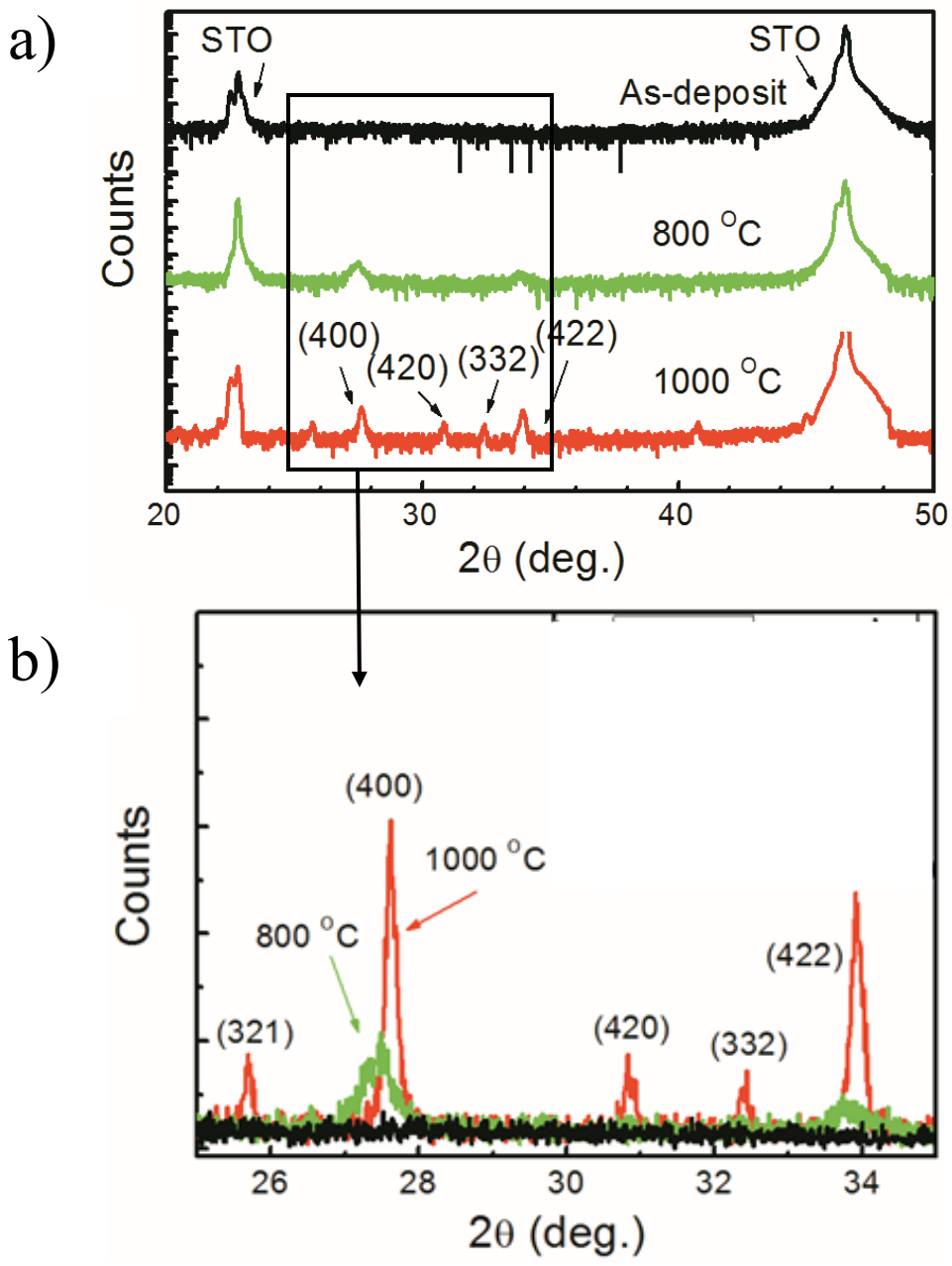

Figure 6.2. XRD patterns of the as-deposited and annealed films; (b) is the magnification of the box in (a).

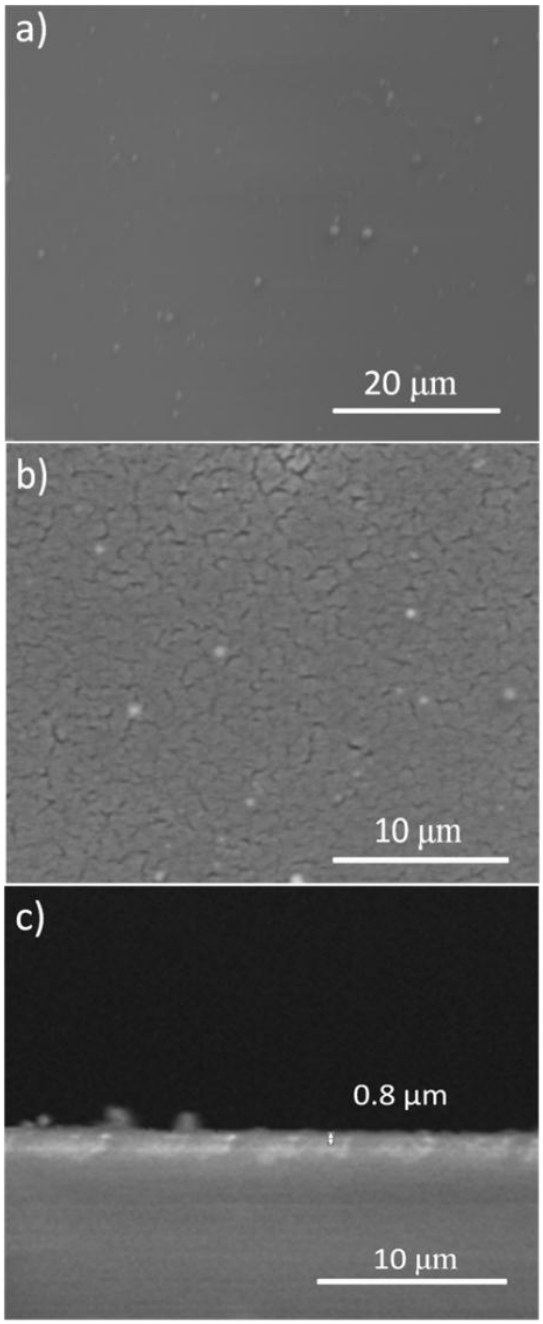

Figure 6.3. SEM images taken on the (a, b) surface and (c) cross section of the films.

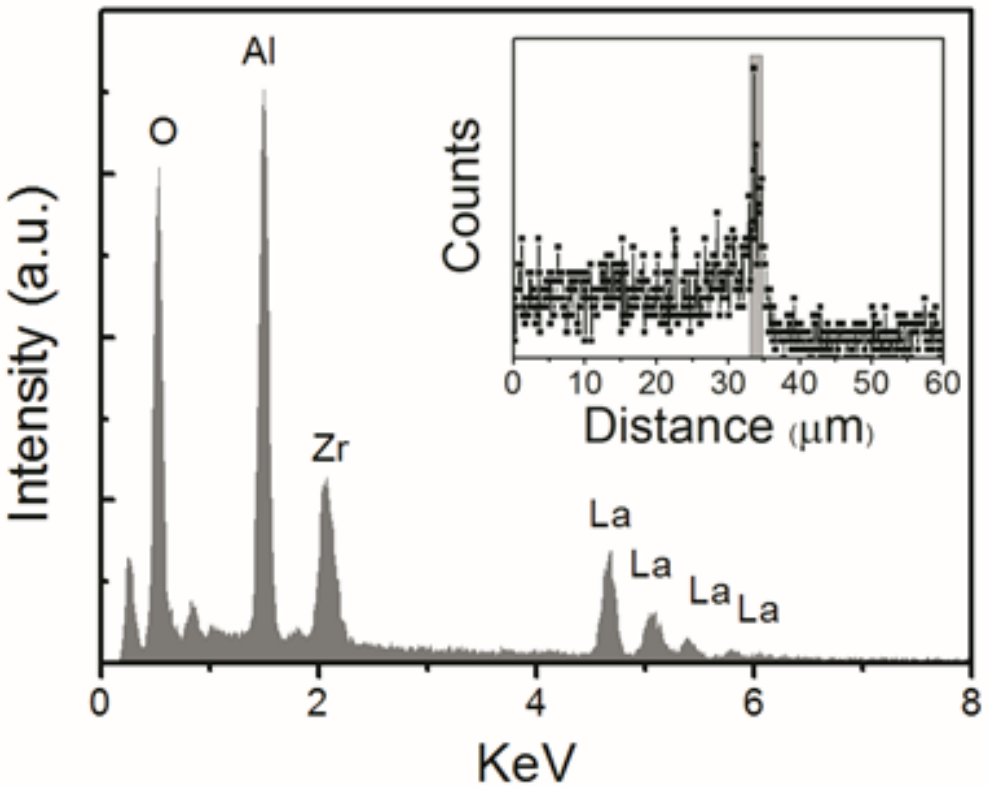

Figure 6.4. EDS spectrum of the LLZO films deposited on sapphire.

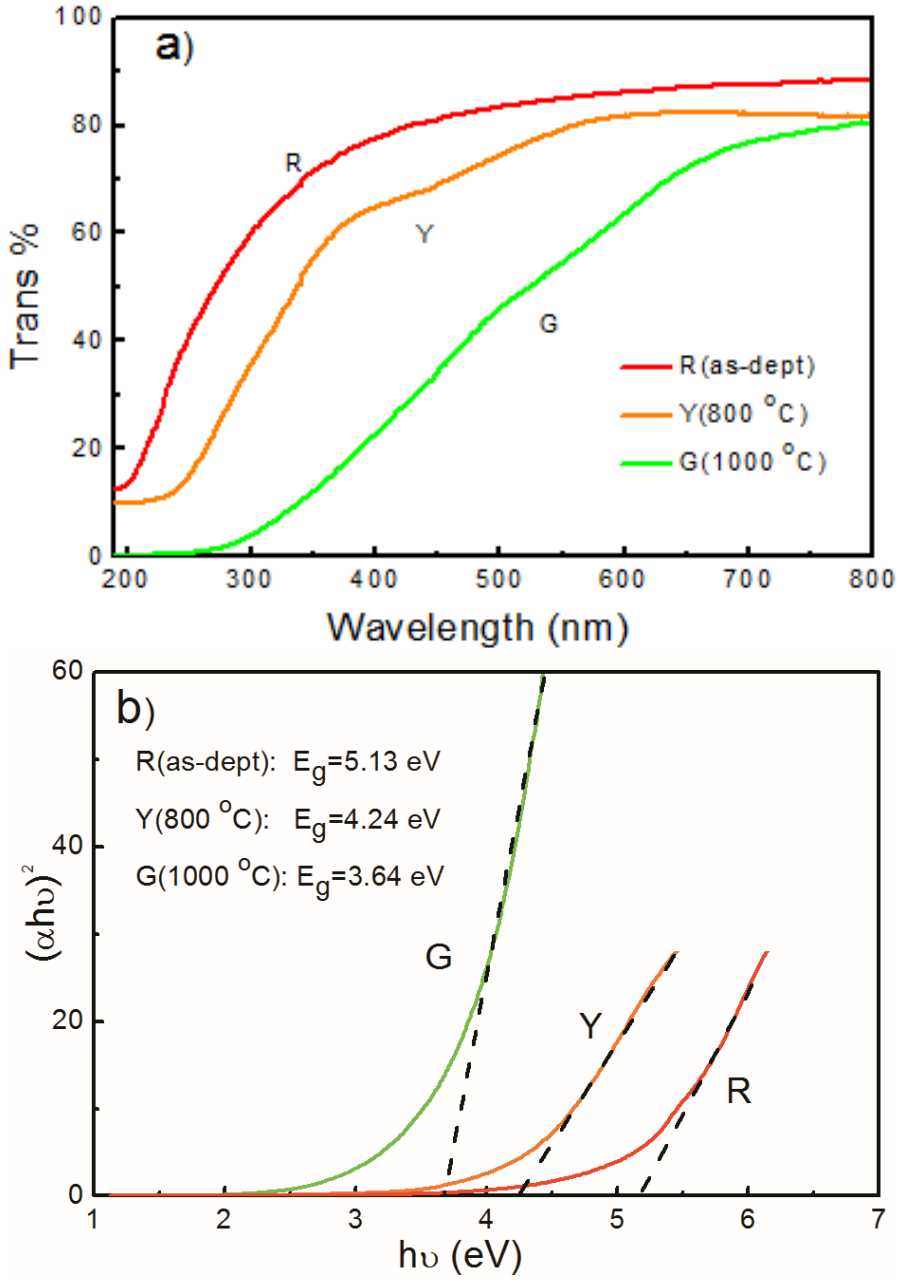

Figure 6.5. (a) Transmittance as a function of wavelength; (b) Plots of $(\alpha h\upsilon)^2$ as a function of photon energy ($h\upsilon$) for LLZO thin films.

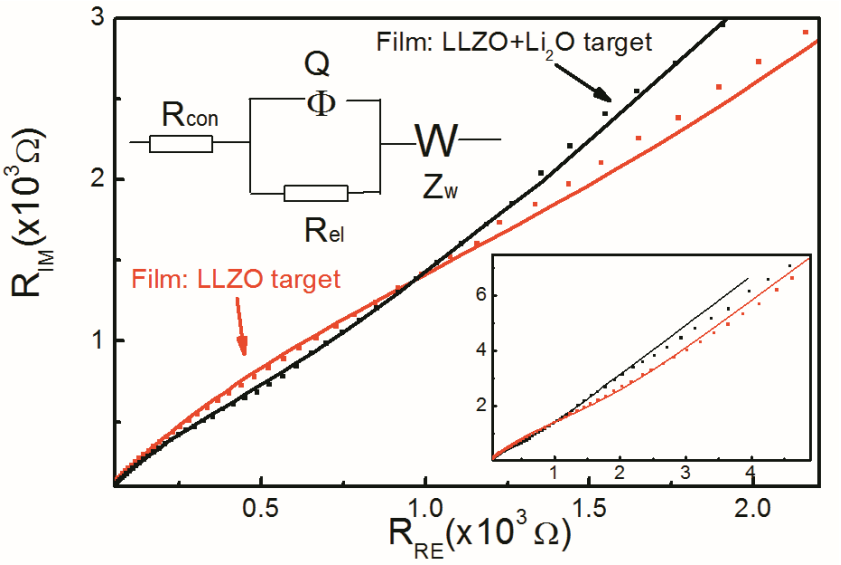

Figure 6.6 Nyquist impedance plots for LLZO films deposited from LLZO+Li_2O dual targets and LLZO target, the left inset is the equivalent circuit and the right inset is the zoom out plots.

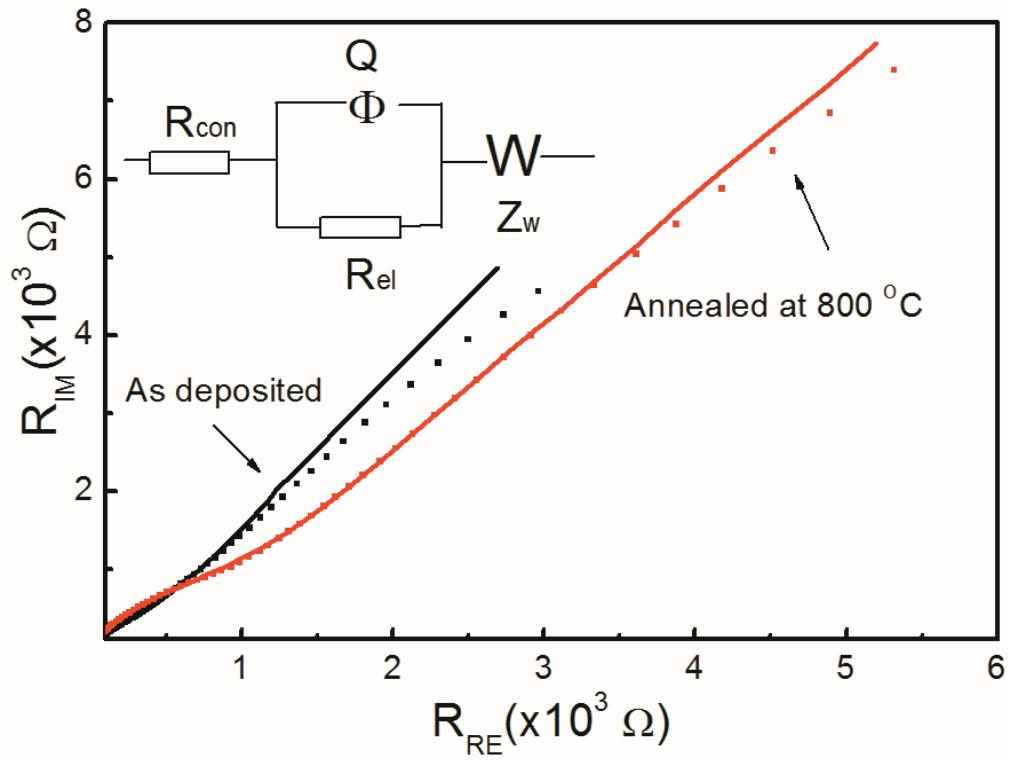

Figure 6.7. Nyquist impedance plots for the as-deposited and thermal annealed LLZO films, inset is the equivalent circuit.

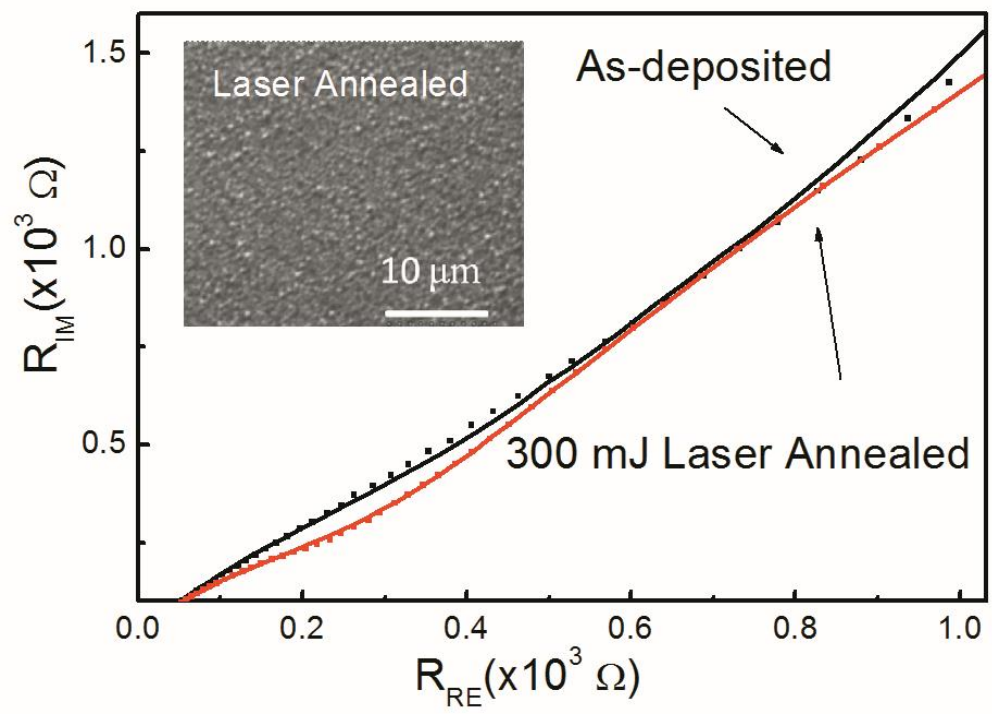

Figure 6.8. Nyquist impedance plots for as-deposited and laser-annealed LLZO films, inset is the surface SEM of the laser annealed films.

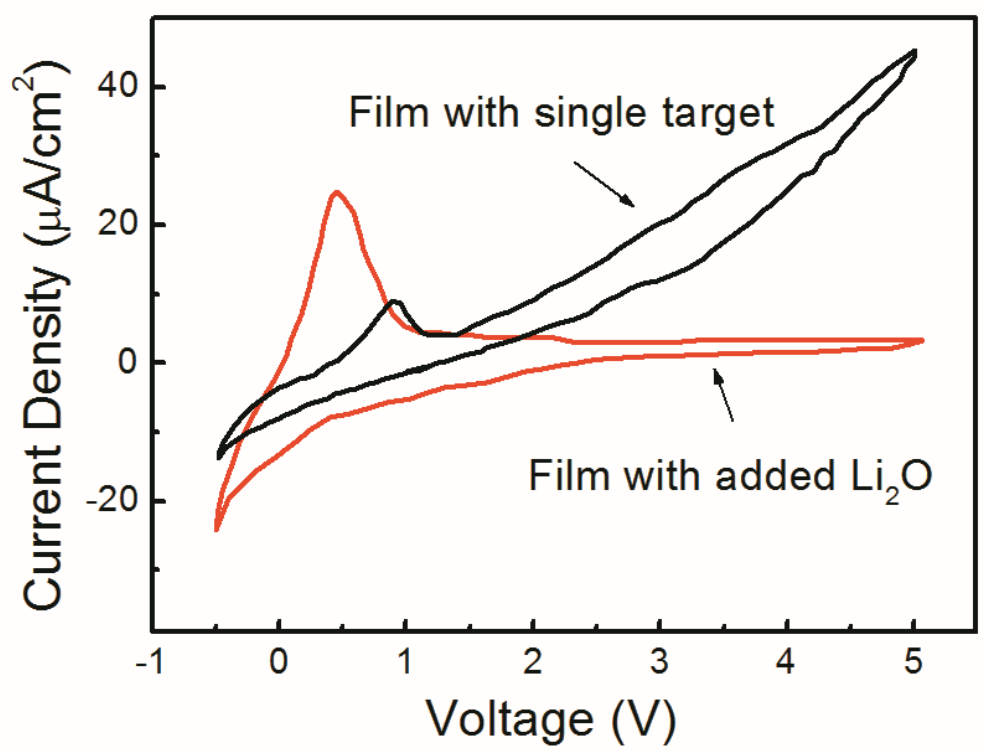

Figure 6.9. Cyclic voltammogram of the Li/LLZO/Pt cell made of the stoichiometric and lithium deficient films.

Table 6.1. Electrical properties of the as-deposited film, thermal and laser annealed films and lithium deficient film.

Target	Anneal (°C)	R (Ω)	σ (S/cm)	Activation Energy (eV)
LLZO+Li_2O	As-deposited	0.3×10^3	3.35×10^{-7}	0.36
LLZO+Li_2O	800	0.67×10^3	1.78×10^{-7}	0.41
LLZO+Li_2O	Laser	0.14×10^3	7.36×10^{-7}	0.32
LLZO	As-deposited	1.4×10^3	7.19×10^{-8}	0.45

CHAPTER 7

CONCLUDING REMARKS

High potential, high capacity polyanionic compounds ($LiFePO_4$ and $Li_2FeP_2O_7$) were evaluated for use as cathodes in lithium-ion batteries. $Li_7La_3Zr_2O_{12}$ was studied as a solid-state electrolyte of bulk form for use in lithium-ion batteries. $Li_7La_3Zr_2O_{12}$ thin films were fabricated and studied as electrolytes for thin-film batteries. According to the results and observations obtained in these studies, important conclusions are summarized in the following paragraphs.

7.1 Polyanionic Cathodes

Low-cost, solution based techniques have been used to successfully synthesize high purity polyanionic compounds. The synthesis conditions have been optimized for achieving high performance composite cathodes in two aspects. Firstly, the type and amount of chelating agent were varied. It was found that a chelating agent with medium carbon chain length (citric acid) peformed better than that with long backbone chains (PVA). This indicated that a medium carbon chains results in homogeneous carbon distribution, therefore, leading to better performance. It was also found that the carbon/lithium ratio in the starting solution would influence the grain size and the

homogeneity of composites. For example, the optimum ratio for $LiFePO_4$/C composite was between 4/2 and 6/2; while the ratio of 9/2 was found to be better than 6/2 in the case of $Li_2FeP_2O_7$/C composite. Secondly, the temperature and time at which the samples were sintered were found to affect the phase and purity of the sample. $LiFePO_4$/C powders heated at 650 ^oC for 12 h gave the best performance and $Li_2FeP_2O_7$/C powders heated at 550 °C for 24 h possessed pure monoclinic phase. The samples were made into cathodes and tested in two-electrode cells. $LiFePO_4$/C powders were found to show a specific capacity of 148 mAh/g, while $Li_2FeP_2O_7$/C showed 108 mAh/g for one lithium removal. The cyclic voltammetry showed that the second lithium of $Li_2FeP_2O_7$ was active and possible to be removed; therefore, higher capacity is attainable once coupled with the electrolyte of a high stable voltage.

7.2 Garnet-type Solid-State Electrolytes

Garnet structured $Li_7La_3Zr_2O_{12}$ have been successfully synthesized by a cheap, fast solution-based technique for application as solid-state electrolyte in lithium-ion batteries. Two phases were formed by sintering the powders yielded from solution at different temperatures. A tetragonal phase was obtained by sintering at 900 ^oC, the room temperature ionic conductivity was found to be $3.67x10^{-7}$ S/cm. However, a cubic phase was obtained by sintering at 1230 ^oC, showing a room temperature ionic conductivity of 1.67×10^{-4} S/cm. This phase change was found to be related to the alumina crucible, which was used to contain the powders when sintered at high temperatures. The incorporation of Al_2O_3 stabilized the cubic phase from transforming to tetragonal phase when cooling down to room temperature by impeding lithium ordering. Both of the phases were assembled into Li/LLZO/$LiCoO_2$ cells. Since the cubic phase LLZO showed

better ionic conductivity, Li/LLZO/$LiCoO_2$ showed higher specific capacity of 3.4 mAh/g, almost 2.5% of the theoretical capacity of $LiCoO_2$. Therefore, the cubic phase LLZO is a very promising solid electrolyte for achieving safe and high performance LIBs. However, the specific capacity is still quite low in comparison with that of lithium-ion cells using liquid electrolyte, due to large interfacial resistance between solids.

For achieving better performance, LLZO thin films were fabricated through pulsed laser deposition at room temperature. The as-deposited films were amorphous, which were then crystallized by annealing. With the increase of annealing temperature, the optical band gap red-shifted due to the grain boundary formation between crystals. The ionic conductivity of the as-deposited films was 3.5×10^{-7} S/cm at room temperature, which decreased because of the crack formation in the films after sintering at high temperatures. In order to reduce the crack formation caused by the different thermal expansion coefficient between films and substrate, a fast annealing process was employed. Laser-annealing was found to increase the ionic conductivity to 7.36×10^{-7} S/cm. Moreover, the films were found to be quite electrochemically stable in contact against lithium metal. Therefore, the LLZO thin films are a potential solid-state electrolyte for next generation TFBs.

7.3 Suggestions for Future Work

The following points are recommended as the possible extension of the above work.

1. Further work on modification of $LiFePO_4$/C needs to be focused on the type of carbon materials. Graphene is the best candidate due to its high electrical

conductivity, continuous conduction path and large surface area, compared to other carbon forms of nanoparticle or nanotubes.

2. The second lithium of $Li_2FeP_2O_7$/C composites can be further removed by using high voltage anodes, e.g., $Li_4Ti_5O_{12}$. The appearance of a small cathodic peak at 4.5 V needs to be explained by further study of its crystal structure by e.g., in situ XRD.
3. Al substitution at the lithium sites was found to increase the stability and ionic conductivity of the cubic phase LLZO. Samples with varying degrees of Al substitution need to be further studied. In addition, substitution of lithium by boron and gallium are worthy investigation, since they are at the same group of Al in the periodic table.
4. A complete thin-film battery using thin film LLZO as the solid electrolyte should be synthesized by thermal evaporation or sputtering techniques. Since pulsed laser deposition technique is of high energy, the growth of a second film on a medium-densified film may cause a problem of penetration. Further research to avoid this problem can be of great interest.